7. SITE 1226[1]

Shipboard Scientific Party[2]

BACKGROUND AND OBJECTIVES

Site 1226 was selected as a drilling target because its microbial activity was expected to be intermediate between that in ocean-margin settings and that in the lowest-activity open-ocean environments.

The principal objectives at this site were

1. To test by comparison with other sites drilled during this expedition whether microbial communities and activities are different in this deeply buried environment than in open-ocean sediments with less organic matter and shallower burial;
2. To document the conditions under which methanogenesis occurs in sulfate-rich open-ocean sediments; and
3. To test how basement hydrologic flow affects microbial communities, microbial activities, and microbial effects on environmental properties in the sediments that overlie the basement.

Site 1226 (3297 m water depth) is located in the eastern equatorial Pacific, 300 km south of the Galapagos Islands, near the present-day boundary between the South Equatorial Current and the Peru Current. Near the sea surface in this region, the advection of water from the Peru Current results in relatively high nutrient levels and biological productivity (Chavez and Barber, 1987). According to its calculated backtrack path, this site has drifted eastward but has remained near its present latitude for most of its history (Pisias et al., 1995; Farrell et al., 1995). Sediment thickness at Site 1226 is 420 m. The oldest sediments immediately overlie basaltic basement and have a biostratigraphic age of 16.5 Ma (Shipboard Scientific Party, 1992a). As described in **"Principal Results,"** p. 2, in the "Site 1225" chapter, geochemical studies of Deep Sea Drilling Project (DSDP) and Ocean Drilling Program (ODP) sites throughout this

---

[1]Examples of how to reference the whole or part of this volume.
[2]Shipboard Scientific Party addresses.

region have shown that seawater flows through the underlying basaltic basement (Baker et al., 1991).

The lithology, sediment age, and many geochemical and geophysical characteristics of the target site were well characterized by earlier studies of Site 846. The gross lithologic and physical properties of the carbonate and siliceous oozes and chalk at Site 846 are characteristic of sediments throughout the region (Shipboard Scientific Party, 1992a; Pisias, Mayer, Janecek, Palmer-Julson, and van Andel, 1995). Leg 138 studies showed that the region has undergone large variations in sediment accumulation over the course of its history. Accumulation of calcium carbonate and opal was unusually low at Site 846 during the Miocene "carbonate crash" of 11–7.5 Ma and was unusually high during the widespread Indo-Pacific "biogenic bloom" that occurred from ~7 to 4.5 Ma (Farrell et al., 1995). The organic carbon accumulation rate is presently high and appears to have gradually increased throughout the Pleistocene (Shipboard Scientific Party, 1992a; Emeis et al., 1995).

Leg 138 shipboard chemical studies of Site 846 show that concentrations of several dissolved chemical species (methane, ammonium, strontium, silica, and alkalinity) peak part way down the sediment column. In contrast, dissolved sulfate, lithium, and calcium exhibit maximum values near the sediment/water interface and the basement/sediment interface (Shipboard Scientific Party, 1992a).

As at Sites 851 and 1225, these patterns of sedimentary interstitial water concentration are inferred to result from modest levels of biological activity throughout the sediment column, coupled with diffusive exchange with the overlying ocean and with seawater flowing through the underlying basaltic basement. The sediments of Site 846 have a higher organic carbon content than the sediments of Sites 851 and 1225. Organic carbon content at Site 846 ranges from 0.2% to 1.0% and is highest in the Pleistocene and upper Pliocene deposits. Accordingly, Site 846 exhibits steeper gradients than Sites 851 and 1225 in interstitial water chemical species that respond to prokaryotic mineralization processes, such as sulfate, ammonium, and methane. The distinctly higher concentration of methane at Site 846 than at Site 851 is particularly intriguing because methanogenesis is generally understood to be suppressed by sulfate-reducing bacteria and methane may be oxidized in the presence of sulfate.

The subsurface distribution of key electron donors (hydrogen, acetate, and formate) and of electron acceptors with higher standard free-energy yields (oxygen, nitrate, manganese oxide, and iron oxides) was not determined for Site 846.

PRINCIPAL RESULTS

Site 1226 provides an excellent series of samples from the sediment/water interface down to basement, including good cores from the contact zone between sediment and basalt. The geochemical gradients that span the 420-m-thick sediment column are bounded at the sediment/seawater interface and the sediment/basement interface by comparable but opposite reduction-oxidation (redox) zonations. Sulfate reduction appears to be the predominant electron-accepting pathway at this site. A broad maximum of dissolved inorganic carbon (DIC) and ammonium in the interstitial water demonstrates the mineralization of organic material throughout the sediment column at several-fold higher rates than at Site 1225. Concentrations drop steeply to near-seawater values at the

sediment/water interface and less steeply toward seawater values at the contact with basement. Water flow through the basement thus provides an effective sink for sedimentary metabolic DIC.

As at Site 1225, the overall chemical zonations are consistent with thermodynamic control of electron acceptor use by subsurface prokaryotes. The data show that water flow through the underlying basaltic basement introduces electron acceptors with high free-energy yields to sediment hundreds of meters below the seafloor. Relative to Site 1225, however, these zonations are more compressed because of higher rates of prokaryotic activities. Oxygen was not detected at any sediment depth within the column at Site 1226, and any oxic surface layer of sediment must thus have been closer to the ocean interface than the depth of our first dissolved oxygen measurement in Hole 1226B, in Section 201-1226B-1H-1, 10 cm. Nitrate, however, was detected in core sections nearest to the sediment/water and sediment/basement interfaces. As at Site 1225, nitrate diffuses upward into the overlying sediment from water flowing through the basement. However, at Site 1226 the diffusing nitrate barely penetrates into the sediment column before being reduced.

As the next electron acceptor in the classical redox sequence, the interstitial water distribution of manganese shows a more complex pattern. Dissolved manganese peaks just at the sediment/water interface and again 9 m below, followed by a steep drop to a zone of near-zero concentration between 100 and 250 meters below seafloor (mbsf). Yet another distinct peak in manganese is present at 300 mbsf. At the bottom of the sediment column, manganese peaks again between 400 mbsf and the sediment/basement interface. The near-basement peak and the 300-mbsf peak together define a broad 160-m interval of unusually high dissolved manganese concentrations.

Comparison with the Leg 138 *Initial Reports* data indicates that the most deeply buried interval of high dissolved manganese is composed of hydrothermally influenced sediments immediately above the basement. The 300-mbsf peak is present in sediments that were deposited at low rates during the Miocene "carbonate crash." In contrast, the sediments that define the overlying interval of near-zero dissolved manganese concentrations were deposited at high rates during the 7- to 4.5-Ma "biogenic bloom" that occurred throughout much of the world ocean (Farrell et al., 1995). These results suggest that the availability of electron-accepting pathways to current subseafloor activity directly depends on broad-scale patterns of past oceanographic change. More detailed interpretation of these multiple zones of apparent manganese reduction and oxidation must await further solid-phase and interstitial water chemical analyses.

The zone of dissolved sulfide extends from just 5 m below the sediment/water interface to a depth of 280 mbsf, and the broad peak reaches 0.7 mM at ~100 mbsf. Throughout this sulfidic sediment column, iron is <10 μM but displays narrow peaks of ~40 μM just above and below the sulfide zone. This pattern reflects both the low equilibrium concentration of ferrous iron in sulfidic interstitial water and the presence of reducible iron near the sediment surface and in the deep sediment column, including a third iron peak at 380 mbsf. The interstitial water data identify a sink for both sulfide and manganese within an interface at 250–280 mbsf, where manganese may precipitate with sulfide.

Methane exhibits a broad peak at 100–250 mbsf with concentrations of 2–3 μM. Although this is still a trace level of biogenic methane, it is

more than tenfold higher than that at Site 1225. Sulfate is present at >68% of seawater concentration throughout the sediment column and indicates active sulfate reduction over the entire methane peak. The co-existence of methane and sulfate at these levels demonstrates the ability of methanogens to maintain an active metabolism in a high-sulfate environment where competition for energy substrates must be strong and where the methanogens may be limited to noncompetitive substrates (Oremland and Polcin, 1982; Oremland et al., 1982). The results also show that sulfate-reducing bacteria in this environment are apparently unable to exploit methane beyond the existing low concentrations.

Acetate and formate concentrations are low in the upper 0–100 m of sediment (<0.5 μM). At greater depths, their concentrations increase to 1–3 μM. This shift in concentrations appears to result from regulation mechanisms that are not yet understood for any sedimentary environment. The volatile fatty acids (VFAs), acetate and formate, are known to be important substrates for most anaerobic respiring bacteria and for methanogens (Winfrey and Ward, 1983; Wellsbury and Parkes, 1995). The interstitial water concentrations of these intermediate fermentation products are regulated by a balance between production and consumption. Concentrations of both acetate and formate are usually found to be relatively higher in organic-rich marine sediments, where they appear to be a function of the rate of fatty acid production and of the energy-yielding metabolism of the consumers. For example, sulfate reducers are able to outcompete methanogens in their efficiency of substrate uptake and thereby drive acetate and formate concentrations to lower levels. However, control of VFA concentrations by such competition is difficult to reconcile with their increased concentrations in the deeply buried Site 1226 sediments that exhibit high dissolved manganese and iron concentrations.

Hydrogen was very low in incubated sediment samples from Site 1226, ranging from 0.1 to 0.8 nM. This is below the equilibrium concentration of a few nanomolar measured in the sulfate reduction zone of more active nearshore sediments (Hoehler et al., 1998) and is even below the concentrations measured at Site 1225, where prokaryotic activity is significantly lower than at Site 1226. According to theoretical calculations of the minimum energy yield required for prokaryotic respiration (Thauer et al., 1977; Schink, 1997) and also according to hydrogen data from a range of sedimentary environments, equilibrium concentration of hydrogen is maintained at the lowest limit that provides the lowest required energy yield of the hydrogen-metabolizing prokaryotes (Hoehler et al., 2001). Based on the dissolved sulfate, manganese, and iron data, sulfate reduction is the predominant respiration process throughout most of the sediment, with the other electron acceptors gaining relative significance near the top and bottom of the sediment column. However, the Site 1226 hydrogen incubation concentrations are lower than those in surface sediments, where sulfate reduction is the predominant process. This finding suggests that either the Site 1226 sulfate-reducing communities derive the canonical minimum energy yield at lower hydrogen concentrations than surface sulfate-reducing communities or they utilize hydrogen at energy yields below the previously accepted theoretical limit.

Experiments on samples from selected sediment depths were conducted on the major microbial processes, including methanogenesis, acetogenesis, sulfate reduction, hydrogen oxidation, and prokaryotic growth. Although most of these data will be available only postcruise,

initial results show a time constant of hydrogen turnover on the order of a few days. Other substrates for microbial activities will have much longer turnover of months to years, and only the postcruise radiotracer results will demonstrate these rates. Total prokaryotic cell counts show 10^6–10^7 cells in the upper 100 m of the sediment column. This is an order of magnitude higher than at Site 1225, in accordance with the higher availability of organic material at Site 1226. Below 100 mbsf, the cell concentrations are rather similar at the two sites. A broad spectrum of prokaryotic most probable number (MPN) counts and enrichments was initiated at this site, ranging from heterotrophs to autotrophs and from psychrophiles to thermophiles. Samples were also taken for cultivation from pieces of basaltic rock recovered at the bottom of Hole 1226B. Because of the slow growth rate of the indigenous microorganisms, successful counts and cultures are expected to require many months to years for growth and development.

Contamination tests are very important for all the microbiological work and were conducted continuously throughout drilling by injecting perfluorocarbon tracer (PFT) into the drilling water. In all cores that were used for microbiological experiments, counts, or isolations, a contamination test was also conducted with prokaryote-sized fluorescent microbeads released within the core catcher upon impact with the sediment (five tests at Site 1226). The detection limit of the PFT method is 0.02 µL drilling fluid (seawater)/g sediment. The results show low to nondetectable contamination in most advanced hydraulic piston corer (APC) cores (<0.1 µL drilling fluid/g sediment) but significant potential contamination in extended core barrel (XCB) cores where the sediment was also visibly disturbed. Subsampling of XCB cores was done here with a reduced sampling program from intact biscuits of sediment. Slurry samples used for an extensive program of microbiology and process studies all (apart from one) have nondetectable contamination when using the PFT method and nondetectable or extremely low contamination using the bead method.

Eight Adara tool deployments and four deployments of the Davis-Villinger Temperature Probe (DVTP) define a sediment/water interface temperature of 1.7°C and an estimated sediment/basement interface temperature of 24.4°C. An accurate linear temperature gradient of 54°C/km was determined through the 420-m-thick deposit. As the sediment depth increases, temperatures thus shift from the psychrophilic microorganism range to the mesophilic range. Deployment of the corresponding pressure tool (Davis-Villinger Temperature-Pressure Probe [DVTP-P]) showed ambient hydrostatic pressure.

As at Site 1225, most cores from the first deep hole (Hole 1226B) were logged on the catwalk with an infrared (IR) camera for postcruise analysis of the IR logging utility. In order to continue building a temperature database suitable for assessing the microbiological effectiveness of catwalk core handling strategies and for determining microbial cultivation strategies, the IR camera was also used to immediately log temperature gradients across cut section ends.

OPERATIONS

Transit to Site 1226

Our transit from Site 1225 to Site 1226 was by way of Puerto Isidro Ayora, Santa Cruz Island, in the Galapagos archipelago, Ecuador. We

laid over at anchorage for 4.5 hr to clear customs as an ODP employee disembarked for compassionate leave. The 1258-nmi transit from Site 1225 to the Galapagos required 117 hr at an average speed of 10.8 kt. We made the 155-nmi transit from the Galapagos to Site 1226 in 13 hr at an average speed of 11.9 kt, arriving on the Global Positioning System coordinates of previously occupied Site 846 at 1100 hr on 19 February. A summary of Site 1226 coring operations is listed in Table **T1.**

Hole 1226A

The positioning beacon for Site 1226 was deployed at 1203 hr on 19 February. A pipe trip positioned the bit at 3308 meters below rig floor (mbrf), and a bottom-water temperature was recorded with the Adara APC temperature tool. Core 1H returned full and did not establish a mudline depth, so Hole 1226A was abandoned.

Hole 1226B

After raising the bit to 3303 mbsf, Core 1H recovered 4.4 m of sediment, establishing the mudline at 3308.1 meters below rig floor. Continuous APC coring from Core 1H through 29H (0.0–271.9 mbsf) returned 105% recovery. Slow drill over after Core 29H prompted us to change to XCB coring, which continued through Core 41X (271.9–378.0 mbsf) (average recovery = 91%). Core 42P, cut with the pressure coring sampler (PCS) (378.0–380.0 mbsf) recovered a full 1-m core as well as ~40 cm in the barrel beneath the pressure chamber. XCB coring continued with Cores 43X through 47X (380.0–421.4 mbsf) (recovery = 74%). Hole 1226B was terminated after coring ~1.5 m into basement.

In addition to the mudline temperature recording before Core 2H, downhole operations in Hole 1226B included Adara tool measurements on Cores 5H, 7H, 10H, 13H, 16H, and 21H (42.4, 61.4, 89.9, 118.4, 146.9, and 194.4 mbsf, respectively). The APC-Methane (APC-M) tool was run continuously on Cores 5H through 29H (32.9–271.9 mbsf) but stopped recording data after Core 10H. No reason for this interruption in recording could be determined. The Tensor APC orientation tool was used continuously on Cores 3H through 29H. The DVTP was deployed at 262.4, 310.0, and 358.4 mbsf, and the DVTP-P was deployed at 241.9 mbsf. A single logging run with the triple combination (triple combo) tool string was completed in Hole 1226B by 1100 hr on 23 February. PFT was pumped continually for microbiological contamination testing. Fluorescent microspheres were also deployed on Cores 2H, 5H, 12H, 22H, 34X, 40X, 43X, 46X, and 47X. Operations in Hole 1226B were terminated at 1045 hr on 23 February.

Hole 1226C

Hole 1226 was a mudline core dedicated to physical properties sampling. Core 1H (0.0–7.9 mbsf; recovery = 100%) was spudded 20 m north of Hole 1226B, and after recovery the hole was abandoned.

Hole 1226D

After another offset of 20 m north, Core 1H (0.0–7.6 mbsf; recovery = 100%) was intended to initiate a second attempt at deep penetration, but upon recovery we discovered that the upper 3 m of the core was surrounded by water in the core liner and the core appeared to be either

slightly under gauge or at least soupy. As an intact mudline core was re-
quired for dense interstitial water and microbiological sampling, we
deemed this core inappropriate and abandoned Hole 1226D. Fluores-
cent microspheres and continuous PFT were used on Core 1H.

Hole 1226E

In planning this expedition, we recognized that time on site would
be a critical parameter if we were to complete all our scientific objec-
tives. Our operations plan included the option of spot coring intervals
of interest in order to conserve valuable operations time. For Hole
1226E, we determined that intervals of particular interest were the up-
per 100 m of the section, the top of the interval where XCB coring re-
turned poor material for interstitial water and microbiological sampling
(250–320 mbsf), and the lower 40 m of the section (380–420 mbsf).
Continuous APC coring from 0.0 to 112.1 mbsf (Cores 1H through
12H) returned an average of 105% recovery.

The interval between 114 and 250 mbsf was then drilled without cor-
ing. Continuous APC coring from 250 to 326 mbsf required drilling
over the bit but returned superb intact cores. The interval between 326
and 378 mbsf was also drilled without coring. At 378 mbsf, the PCS was
run at the same depth as deployed in Hole 1226B to test a different bit
configuration (polycrystalline diamond [PDC] vs. carbide). A nearly full
core barrel was recovered (Core 21P), but a piece of chert was jammed
in the throat of the tool, preventing recovery under pressure. Four XCB
cores (Cores 22X through 25X) (380.0–418.4 mbsf; recovery = 76%)
ended operations in this hole.

In order to evaluate the downhole temperature gradient, additional
Adara temperature measurements were performed at 45.6, 74.1, and
112.1 mbsf in Hole 1226E. To complete the temperature profile in this
hole, the DVTP was deployed at 307 and 400 mbsf and an in situ pres-
sure measurement was attempted with the DVTP-P at 326 mbsf. PFT
was pumped continually for microbiological contamination testing,
and fluorescent microspheres were deployed on Cores 1H, 15H, and
16H as part of our contamination testing protocol. The APC-M tool was
deployed on Cores 5H through 12H. Operations at Site 1226 concluded
when the bit passed through the rig floor at 1615 hr on 25 February,
and we began our transit to Site 1227.

LITHOSTRATIGRAPHY

The sedimentary sequence at Site 1226 consists of alternating inter-
vals of nannofossil and diatom ooze, with varying numbers of radiolar-
ians and foraminifers. Accessory minerals such as plagioclase and pyrite
are present in minor amounts throughout the cored interval. Two
lithostratigraphic units were established at Site 1226 (Fig. F1). Unit I is
characterized by decimeter- to meter-scale variations in biogenic silica
and carbonate, whereas Unit II is dominated by red, green, and brown
metalliferous sediments directly overlying the oceanic basement. Only
Hole 1226B was used for lithostratigraphic purposes, as it was the only
hole at Site 1226 that was continuously cored from the sediment sur-
face to the oceanic basement. As Site 846, which had previously been
drilled during Leg 138, is located in close proximity (within 100 m) of
Site 1226, the age framework presented in this chapter follows the chro-

F1. Lithostratigraphic summary,
p. 40.
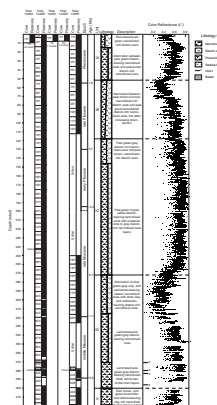
nostratigraphy of Site 846 (Shipboard Scientific Party, 1992) revised according to the timescale of Berggren et al. (1995a, 1995b).

The lithostratigraphic description of the sequence is based on visual observation of sediment color and sedimentary structures, smear slide analysis, and color reflectance. X-ray diffraction (XRD) analyses and laboratory measurements of magnetic susceptibility, density, and water content (see "Physical Properties," p. 26) were also used to detect lithologic changes.

Description of Lithostratigraphic Units

Unit I

Interval: 201-1226B-1H-1 through 45X-2
Depth: 0–400.2 mbsf
Age: Pleistocene to early Miocene

Unit I contains alternating intervals of diatom-bearing to diatom-rich nannofossil ooze and nannofossil-rich diatom ooze with varying amounts radiolarians, foraminifers, and siliciclastic components. In the deeper part of Unit I below ~370 mbsf, the sediments become progressively consolidated and were classified as chalk or diatomite, depending on their mineralogical composition. The sediments of this unit range in age from Pleistocene to early Miocene (Shipboard Scientific Party, 1992). We divided Unit I into four subunits (IA–ID). Subunit IA consists of Pleistocene pale gray to green nannofossil-rich diatom ooze in the upper part and alternating intervals of diatom-bearing and diatom-rich nannofossil ooze in the lower part of the subunit. The mostly late Pliocene age sediments of Subunit IB are dominated by alternating meter-scale intervals of dark olive-green diatom ooze and pale green diatom-rich nannofossil ooze. Pale greenish gray nannofossil ooze and pale brown to pale olive diatom-rich nannofossil ooze of late Pliocene to late Miocene age are the dominant lithologies of Subunit IC. Subunit ID is characterized by alternating intervals of olive green–gray clay- and radiolarian-bearing nannofossil diatom ooze and white clay- and radiolarian-bearing diatom-rich nannofossil ooze of early to late Miocene age. Incipient lithification in the lower part of this subunit transforms the sediments into diatomite and chalk. The presence of dolomite, porcelanite, and chert provides further evidence for the diagenetic sequence in the carbonate- and silica-rich sediments of Site 1226.

Subunit IA

Interval: 201-1226B-1H-1 through 6H-CC
Depth: 0–51.9 mbsf

The uppermost part of Subunit IA (Core 201-1226B-1H through Section 3H-1; 0–15.4 mbsf) consists of intensively bioturbated pale gray to green nannofossil-rich diatom ooze. Trace fossils (mostly *Zoophycos, Skolithos,* and *Planolites*) as well as open burrows are common (Fig. F2A). The mineralogic assemblage is dominated by varying amounts of biogenic opal-A (siliceous microfossils, mostly diatoms) and calcite (nannofossils and foraminifers) (see "Mineralogy," p. 11).

Below 15.4 mbsf, the subunit is dominated by alternating intervals of light gray diatom-bearing nannofossil ooze and darker pale green diatom-rich nannofossil ooze. The foraminifer content increases with depth, and a faint gray banding, crosscut by burrows with purple reac-

F2. Site 1226 features, p. 41.
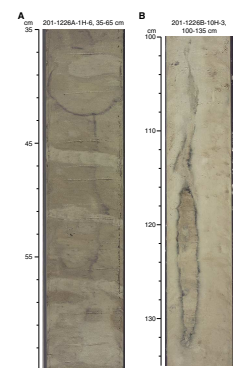
tion halos, is common. Trace amounts of pyrite were also found (see "Mineralogy," p. 11). Color reflectance values are generally high but variable, ranging from ~40% to 65% in the visible bands.

Subunit IB

Interval: 201-1226B-7H-1 through 13H-CC
Depth: 51.9–118.4 mbsf

Subunit IB is dominated by alternating meter-scale intervals of dark olive-green diatom ooze and pale green diatom-rich nannofossil ooze. The top of the subunit is marked by a sharp color change from light green to dark olive green, which reflects an overall increase of the diatom component. This increase of biogenic silica (opal-A) in the sediment is also confirmed by XRD analyses (see "Mineralogy," p. 11). Color reflectance data show a clear negative excursion toward lower values (35%–45%) caused by the generally lower reflectivity of diatom-rich sediments at Site 1226 (see "Color Reflectance Spectrophotometry," p. 11). Color reflectivity returns to higher and more variable values in the lower part of the subunit.

Mottling and bioturbation as well as pale purple alteration halos around burrows dominate the lighter-colored diatom-bearing nannofossil ooze intervals. Some of the trace fossils were recognized as burrows of *Zoophycos* type. The relative thicknesses of the alternating darker diatom ooze and lighter nannofossil ooze intervals are variable, with the pale brown diatom ooze layers becoming thicker toward the center of the subunit. Minor amounts (<5%) of radiolarians and foraminifers were observed in Cores 201-1226B-12H and 13H, as well as a dark spot containing both pyrite and plagioclase (XRD Sample 201-1226B-12H-7, 53–54 cm) (see "Mineralogy," p. 11).

As already noted by the Leg 138 Shipboard Scientific Party, at Site 846 the color banding that characterizes the subunit is arranged in cycles ranging from 1 to 10 m in thickness. Based on an average sedimentation rate of ~40 m/m.y. (Shipboard Scientific Party, 1992), the duration of these cycles would range between ~25 and ~250 k.y. and may result from Milankovitch-type orbital forcing of the sedimentary regime during deposition of Subunit 1B.

Subunit IC

Interval: 201-1226B-14H-1 through 29H-CC
Depth: 118.4–271.9 mbsf

Within the upper 28 m of Subunit IC (Cores 201-1226B-14H through 17H; 118.4–146.9 mbsf), pale greenish gray nannofossil ooze and pale brown to pale olive diatom-rich nannofossil ooze are the dominating lithologies. Mottling and bioturbation range from moderate to intense and are typically associated with pale purple alteration rims. Pale purple and gray banding is either dominant (e.g., Core 201-1226B-15H) or faint and overprinted by bioturbation (e.g., Core 201-1226B-16H). This banding disappears in darker greenish zones, where diatoms are more abundant.

In the lower 125 m (Cores 201-1226B-18H through 29H; 146.9–271.9 mbsf), the subunit is characterized by pale green to pale yellow nannofossil ooze with scattered olive to gray diatom-rich nannofossil ooze layers showing high opal-A content (e.g., XRD Sample 201-1226B-29H-6, 104–105 cm). Intense to moderate bioturbation and burrows with pale purple, green, and gray reaction halos are common. Bioturbated

intervals are often characterized by a mottled texture and sometimes by very long (up to 90 cm) subvertical burrows, probably of *Skolithos* type (e.g., Core 201-1226B-24H). Pale purple to white horizontal alteration bands are scattered throughout the lower part of Subunit IC and are usually either weakly developed or partially obliterated by bioturbation. Scattered millimeter-sized pyrite nodules were also observed and identified in XRD spectra (Sample 201-1226B-29H-7, 56–57 cm).

Subunit ID

Interval: 201-1226B-30X-1 through 45X-2
Depth: 271.9–400.2 mbsf

The main lithology in the uppermost part of Subunit ID (Cores 201-1226B-30X through 34X; 271.9–314.7 mbsf) is characterized by alternating intervals of olive green–gray clay- and radiolarian-bearing nannofossil diatom ooze (of mixed opal-A and calcite composition) and white clay- and radiolarian-bearing diatom-rich nannofossil ooze. Low color reflectance values are common (Fig. F1) because of a marked increase of the diatom component. Yellow clasts of dolomite (Fig. F2D) and dark specks of pyrite, one of which contained trace amounts of barite (Sample 201-1226B-30X-7, 36–38 cm), were also observed.

In the central part of Subunit ID (Cores 201-1226B-34X through 40X; 314.7–371.1 mbsf), the main lithology consists of pale greenish gray and yellow diatom-bearing nannofossil ooze. Variable amounts of clay, plagioclase, and volcanic glass are also present. The sediments are finely laminated and slightly to moderately bioturbated.

The lowest part of Subunit ID (Cores 201-1226B-41X through 45X; 371.1–400.2 mbsf), is marked by a few brown brittle quartz layers (Sample 201-1226B-41X-1, 2–3 cm) (Figs. F2C, F3D) that are present between 371 and 398 mbsf and correlate with those found at Site 846 between 372 and 398 mbsf (Shipboard Scientific Party, 1992). About 10 m deeper in the section, green porcelanite composed of opal-CT was found (Sample 201-1226B-44X-CC, 9–10 cm). The lowest part of Subunit ID also coincides with the first appearance of semilithified sediments of both siliceous (diatomite) and calcareous composition (chalk).

Unit II

Interval: 201-1226B-45X-3 through 47X
Depth: 400.2–421.4 mbsf
Age: early Miocene

Unit II consists of pale green (upper part) and light reddish brown to brown and green (lower part) foraminifer- and diatom-bearing clay-rich nannofossil chalk that directly overlies the oceanic basement (Fig. F2E). Black spots and layers are common. The transition between the green upper part and the brown lower part is present at ~405 mbsf (Sections 201-1226B-46X-4 and 201-1226E-24X-4). The reddish color is caused by the presence of hematite (Sample 201-1226B-47X-2, 53–54 cm) (Fig. F3F), whereas the black color represents either chert or manganese oxide minerals. Bioturbation is generally moderate. In Sections 201-1226B-46X-4 and 201-1226E-24X-4, a green band is present within the light reddish brown sediments at a depth of ~413 mbsf. The top of the band is truncated by a sharp contact, and the layer above is a ~5-cm-thick graded bed that contains reworked sediments from below the contact (Fig. F2D, F2E). Near the basalt/sediment interface, a few normal graded

F3. Examples of XRD analyses, p. 45.
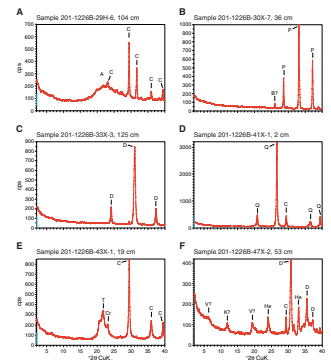
beds as well as reversed graded beds were observed. These beds are a few centimeters thick and are composed of angular to subangular granule-, sand-, and silt-sized clasts. The larger clasts in these beds are either fragments of black chert or dolomite, whereas silt is mostly volcanic ash. Below 420.6 mbsf, 80 cm of feldspar-rich basaltic breccia was recovered (Fig. F2G).

Color Reflectance Spectrophotometry

Spectrophotometric analyses of Hole 1126B samples provided a detailed and mostly continuous record of color variations in the sediments of Site 1226. Color reflectance data greatly improved lithostratigraphic reconnaissance and allowed correlations and comparisons between lithologic changes and variations in other parameters of the sediment, such as magnetic susceptibility, physical properties, and gamma radiation.

In particular, variations in lightness (L*) match both primary and secondary lithostratigraphic divisions, as shown in Figure F1. Lightness is usually proportional to the relative amount of nannoplankton ooze (usually pale green) and is inversely proportional to the amount of diatom ooze (usually pale brown/olive to brown/olive).

Three negative excursions can be recognized in the lightness curve of Figure F1. The first two excursions correspond to stratigraphic intervals dominated by diatom oozes. The third low-reflectivity interval is present below 400 mbsf in a nannofossil ooze interval that is partially red, brown, and black because of the concentration of hematite and possibly magnetite in the sediment (see "Unit II," p. 10, in "Description of Lithostratigraphic Units" and "Mineralogy," p. 11).

The two low-reflectivity intervals located between ~50 and 70 mbsf and between ~270 and 320 mbsf can be also correlated with variations in other parameters of the sedimentary record. For instance, they both match the two main peaks of total organic carbon reported for Site 846 (Shipboard Scientific Party, 1992). Also, lightness variations match well the variations in some of the physical properties of the sediment column (see "Physical Properties," p. 26); they are proportional to variations in density and inversely proportional to variations of porosity and water content. Therefore, darker diatom ooze layers at Site 1226 are generally more porous and less dense than the light-colored nannofossil ooze sediments. It is also worth noting that the first negative excursion of the L* curve (located between ~50 and 70 mbsf) matches the only main positive peak of the natural gamma radiation curve (see "Physical Properties," p. 26).

Mineralogy

XRD was performed on 25 samples from Hole 1226B and 11 samples from Hole 1226E. Overall, the two main sediment components detected are calcite and opal-A (Fig. F3A). Their relative proportion reflects the abundance of nannofossils and diatoms, the two main biogenic components of the sediment. Biogenic opal-A silica is particularly abundant in Subunit IB, at the bottom of Subunit IC, and at the top of Subunit ID.

Pyrite was detected in most of the sediments of Subunits IA, IB, and IC. However, the highest concentrations of pyrite were found on top of Subunit ID (Samples 201-1226B-30X-7, 36–37 cm, and 31X-5, 120–121 cm), together with trace amounts of barite (Sample 201-1226B-30X-7,

36–37 cm) (Fig. F3B). Dolomite was detected as yellow nodules in Subunit ID (Samples 201-1226B-33X-3, 125–126 cm, and 36X-1, 105–106 cm) (Fig. F3C).

Both opal-CT and quartz, two diagenetic products of biogenic opal-A, were found in the lowermost part of Hole 1226B. Quartz composes the brittle brown chert layers that are present in the lowermost part of Subunit ID and Unit II below 371 mbsf (Samples 201-1226B-41X-1, 2–3 cm; 44X-CC, 9–10 cm; and 47X-1, 7–8 cm) (Fig. F3D). Opal-CT was found in green porcelanite layers at a depth of ~380 mbsf (Sample 201-1226B-43X-1, 19–20 cm) (Fig. F3E), below the depth of the first occurrence of chert layers (Fig. F1). The presence of opal-CT below chert indicates anomalous conditions during silica diagenesis at Site 1226. The mineralogic assemblage of an orange-red sample collected from the lowermost part of Unit II (Sample 201-1226B-47X-2, 53–54 cm) (Fig. F3F) includes hematite, clay minerals (illite/smectite), and dolomite.

Thin Section

Light gray basalt was recovered from the core catcher of Core 201-1226B-47X. A small rounded fragment was archived, and a thin section (see "Site 1226 Thin Sections") and bulk geochemical analysis was acquired immediately postcruise. In thin section, the sample has abundant fresh plumose to sheaf quench-textured plagioclase. The ratio of quench-textured plagioclase to altered groundmass glass varies from plagioclase much more abundant than groundmass to the opposite across the 2 cm of the section, indicating the sample was taken from near the margin of a flow. Calcite is the most common alteration phase, filling vesicles and fractures with less abundant smectite. The major element oxide bulk chemistry of this sample (Table T2) is average East Pacific Rise (EPR) mid-ocean-ridge basalt (MORB) and is virtually identical to the composition reported for Sample 138-846B-45X from the basement sampled at this location during Leg 138. Trace element abundances are also consistent with normal EPR MORB compositions.

Summary

At Site 1226, a nearly complete Pleistocene to early Miocene section of alternating intervals of nannofossil-rich diatom ooze and diatom-rich nannofossil ooze with varying amounts of foraminifers and radiolarians was recovered. The thickness of the sedimentary section at this site is ~420 m. This depth also marks the contact between the sediments and the oceanic basement.

The main sedimentological characteristic of the sediments is variation in abundance of biogenic carbonate (mostly nannofossils) and silica (mostly diatoms) at a scale of decimeters to several meters. Leg 138 studies inferred that this variation might be the result of Milankovitch-type orbital forcing during deposition of the sediments at Site 1226 (Shipboard Scientific Party, 1992). Two sedimentary units were distinguished. Unit I is characterized by alternating intervals of diatom-bearing to diatom-rich nannofossil ooze and nannofossil-rich diatom ooze with varying amounts of radiolarians, foraminifers, and siliciclastic components. In the deeper part of Unit I, the sediments become progressively consolidated and were classified as chalk and diatomite. Within Unit I, four subunits were distinguished (Subunits IA–ID). Boundaries between these subunits coincide with major breaks in color reflectance and changes in most physical properties of the sediments

(see "Physical Properties," p. 26). The presence of dolomite, porcelan-
ite, and chert layers below 300 mbsf documents the onset of both car-
bonate and silica diagenesis. The presence of porcelanite below the
depth of the first occurrence of chert layers indicates a somewhat
anomalous diagenetic sequence for biogenic silica at Site 1226.

Unit II consists of ~20 m of light reddish brown and green metallifer-
ous nannofossil chalk, which directly overlies the oceanic basement.
Manganese- and iron-rich minerals, volcanic glass, and reworked hori-
zons are present above plagioclase-rich basaltic basement.

BIOGEOCHEMISTRY

The interstitial water (IW) program at Site 1226 was designed to
clearly define biogeochemical zones and to allow for modeling of bio-
geochemical reaction rates and associated chemical fluxes. Like Site
1225, this site is characterized by active fluid flow in the underlying
basement (Baker et al., 1991). The sampling strategy was similar to that
applied at Site 1225, with the main difference being a higher sampling
frequency of two samples per core carried through the first deep hole,
Hole 1226B (total of 87 samples). After initial analyses of these samples,
an additional 41 samples were collected from Hole 1226E to target spe-
cific depth intervals where interstitial water profiles displayed signifi-
cant chemical variation—samples from the upper 25 mbsf (16 samples
from 252.85 to 323.85 mbsf and 9 samples from 382.80 to 418 mbsf)
(Table T3). In addition to routinely employed chemical analyses, we ac-
quired IW concentration data for hydrogen, acetate, formate, nitrate,
dissolved oxygen, DIC, high-resolution manganese and iron, and meth-
ane at trace levels.

As at Site 1225, microbially mediated reactions and chemical ex-
change across the sediment/seawater and sediment/basement interfaces
drive most of the variations in interstitial water chemistry. As a result,
distinct biogeochemical zones are present downhole at these sites. Pro-
files of dissolved species at Site 1226 are consistent with somewhat
greater microbial activity compared to Site 1225.

Interstitial Water

Alkalinity and DIC have similar downhole profiles. Alkalinity in-
creases from ~2.8 mM near the sediment/water interface to a high of
~6.9 mM at 59 mbsf (Fig. F4A). The values then decrease gradually to
~6.5 mM at 192 mbsf and more rapidly to ~2.0 mM at the bottom of
Hole 1226B. The range in alkalinity at this site is ~5 mM. DIC increases
from 2.8 mM near the sediment/water interface to a broad maximum of
~7.0 mM between 83 and 188 mbsf (Fig. F4B). DIC concentrations then
decrease to ~2.0 mM at the bottom of Hole 1226B. The range in DIC
concentrations is also ~5 mM. Both alkalinity and DIC have their great-
est variability between adjacent samples in the deepest 100 m of the
sediment column. The onset of this variability coincides with signifi-
cant changes in lithology and physical properties associated with the
transition to lithostratigraphic Subunit 1D (see "Lithostratigraphy,"
p. 7, and "Physical Properties," p. 26). The alkalinity profile at Site
1226 is similar to the profile previously obtained at Site 846 (Shipboard
Scientific Party, 1992). DIC measurements were not made at Site 846.
The ~5-mM increases in alkalinity and DIC concentrations at Site 1226
are greater than the increases in these parameters at Site 1225 (see Fig.

T3. Dissolved species, p. 84.

F4. Dissolved species in interstitial
waters, p. 46.
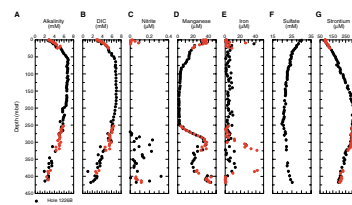
F4). This strongly suggests that rates of respiration at Site 1226 are higher than those at Site 1225.

Dissolved oxygen was not detected with the microelectrode at sediment depths of 0.1 mbsf and below. Attempts to measure oxygen in highly consolidated sediments immediately above basement failed.

Interstitial water nitrate concentrations were determined in the upper and lower sections of Holes 1226B and 1226E for comparison with Site 1225. Based on preliminary results, the pronounced zones of high nitrate at the top and bottom of the sediment column as observed at Site 1225 are not present at Site 1226. In the lowermost 16 m of Hole 1226E, nitrate concentrations reach only 3 µM, compared to 23 µM at Site 1225.

Nitrite formation is an intermediate step in nitrification, and interstitial water nitrite concentrations were analyzed for samples between 260 and 418 mbsf in Hole 1226B and between 0 and 11.95 mbsf and 401.90 and 418 mbsf in Hole 1226E and in the deepest 18 m of the site (Table T3; Fig. F4). In an attempt to detect active turnover of interstitial water nitrogen species, interstitial water nitrite concentrations were determined within 5 to 30 min after sampling. Nitrite concentrations range from 0.0 to 0.23 µM, with the highest values between 290 and 350 mbsf (Fig. F4). Nitrite concentrations roughly track nitrate concentrations in the lowermost ~20 m.

The high-resolution dissolved manganese profile (Fig. F4D) shows considerable structure, including features of potential significance to subsurface microbial activity. Unlike at Site 1225, manganese concentrations >30 µM are present just below the seafloor (0.1–0.2 mbsf). After a slight drop and a second peak at 1.8 mbsf, dissolved manganese declines to 5 µM at 80 mbsf. Concentrations drop less precipitously over the next 80 m to 2 µM. At 250 mbsf, dissolved manganese rapidly increases to form a peak, with values exceeding 36 µM at 303 mbsf (Sample 201-1226B-33X-2, 135–150 cm). Concentrations then decrease to a local minimum of 18 µM at 360 mbsf and increase to a high of 44 µM near the base of the hole.

The upper part of the dissolved manganese profile is somewhat similar to that at other open-ocean sites that underlie regions of primary productivity (Brady and Gieskes, 1976). The shallow concentration peak probably results from the dissolution of manganese oxide phases driven by microbial manganese reduction. The changes in gradients at 80 and 160 mbsf are likely caused by manganese precipitation. The deeper part of the profile probably necessitates a complex explanation because the dissolved manganese peaks likely signify reduction of solid manganese oxides—phases that would not accumulate in the presence of significant amounts of sedimentary organic carbon. Dissolved organic carbon may be diffusing downward and reacting with solid manganese phases at depth. This dissolved manganese profile at Site 1226 may represent a special case where an interval of low organic sedimentation (and presumably high burial rate of authigenic manganese oxides) was followed by an interval of relatively high primary productivity in surface waters (and presumably rapid accumulation of organic carbon).

Similar to Site 1225, dissolved iron concentrations at Site 1226 (Fig. F4E) show considerably more scatter between adjacent samples than do other analyzed species. Concentrations are not significantly different between true replicate samples, indicating that the scatter is not caused by poor analytical precision. At Site 1225, two explanations were offered for this variability: (1) oxidation of iron in some samples during

squeezing or water handling or (2) inclusion of solid iron in some samples. To address the first possibility, most interstitial water samples at Hole 1226B were squeezed through a three-way valve into a second glass syringe evacuated of air. In general, however, adjacent samples from Hole 1226B show more variation in iron concentration than samples processed by conventional means from Hole 1226E, possibly because of iron adsorption on glass. To address the second possibility, several samples were pushed through 0.45-µm (standard) and 0.10-µm filters. However, iron concentrations for all of these dual analyses lie within analytical precision (Table T4). If solid iron contributes to the variation in "dissolved iron," the corresponding particulates must be <0.10 µm in size. Other than the unresolved scatter, the iron profile is characterized by three short intervals of high concentrations. These peaks are centered at ~10, 315, and 385 mbsf. These peaks are present on the shoulders of peaks in dissolved manganese.

Dissolved sulfate concentrations decrease from near seawater concentrations at the sediment surface to 19.8 mM at 246.20 mbsf (Table T3; Fig. F4F). Below this depth, sulfate increases to 25.2 mM at 417.20 mbsf, just above the basaltic basement. The downhole profile generally exhibits lower sulfate values than that at Site 1225. Moderate sulfate reduction occurs throughout most of the sediment column at Site 1226.

The downhole profile of dissolved strontium is similar to that obtained for Site 846, although with much higher depth resolution. Concentrations are similar to that of seawater (86 µM) in the uppermost sample at 0.10 mbsf and then steadily rise to values >310 µM at 205 mbsf (Fig. F4G). Below 300 mbsf, concentrations sharply decrease to 190 µM above basement. The overall profile suggests an active zone of carbonate recrystallization in lithostratigraphic Subunit 1C (see "Description of Lithostratigraphic Units," p. 8, in "Lithostratigraphy"), with diffusive exchange with seawater at the top and with modified seawater at the bottom.

Dissolved lithium concentrations track those determined for Site 846, although there is an offset at low values that requires additional attention (Fig. F4H). Concentrations are similar to that of seawater (26 µM) in the uppermost sample at 0.37 mbsf and then steadily decrease to a low of 11 µM at 220 mbsf. With a slight concavity at ~300 mbsf, concentrations increase to ~23 µM above basement. Lithium is removed from interstitial water during carbonate recrystallization. As with strontium, the overall profile suggests an active zone of carbonate recrystallization in lithostratigraphic Subunit 1C.

Concentrations of dissolved barium are below the detection limit (0.1 µM) in all samples analyzed from Site 1226.

Concentrations of dissolved calcium, potassium, and magnesium were determined by inductively coupled plasma–atomic emission spectroscopy. Interstitial water samples were diluted at 50:1 with deionized water, and standard curves were constructed by diluting International Association for the Physical Sciences of the Ocean standard seawater aliquots with a range of deionized water volumes. Given current operating conditions for the instrument, the dilution is probably not ideal and this may have affected analytical precision, especially for magnesium and potassium.

The downhole profiles of dissolved calcium, potassium, and magnesium are similar to those obtained for Site 846, although with far greater vertical resolution. Concentrations of calcium are similar to that of seawater (10.8 mM) in the uppermost sample at 0.10 mbsf and then decrease to 7.5 mM at ~100 mbsf (Fig. F4I). Dissolved calcium steadily

T4. Iron concentrations, p. 87.

returns to 10.8 mM between 360 and 380 mbsf, an interval where silica concentrations drop precipitously and the sediment contains chert horizons. Calcium concentrations then rise steeply to 16 mM over the lowermost 40 m. Dissolved potassium generally decreases from 11.8 mM at the seafloor to 10.6 mM at 330 mbsf. Below this depth and after a possible offset to higher concentrations, potassium drops rapidly to 9 mM above basement. By contrast, dissolved Mg concentrations steadily decrease from 54 mM near the seafloor to 48 mM above basement.

Total dissolved sulfide ($\Sigma H_2S = H_2S + HS^-$) is present at detectable levels (>0.0002 mM) at depths greater than 0.59 mbsf (Fig. **F4J**). The concentrations of sulfide increase linearly with increasing depth to 0.43 mM at 21.45 mbsf. Below this depth, the concentrations of sulfide continue to increase with increasing depth, but the data show more scatter. The scatter in the sulfide data corresponds to the increase in scatter in the methane data at the same depths (Fig. **F4K**). Like methane, sulfide may have been lost from samples through degassing. In this case, the maximum values best approximate in situ concentrations. Sulfide concentrations continue to increase with increasing depth and form a broad maximum of 0.5–0.7 mM between 45 and 178 mbsf. Peak concentrations of sulfide reach 0.7 mM at 74 mbsf. Below 178 mbsf, the concentrations of sulfide decrease linearly with depth to 0.089 mM at 235 mbsf. Between 235 and 279 mbsf, sulfide concentrations vary between 0.09 and 0.19 mM before decreasing to values of <0.0001 mM at depths below 281 mbsf.

Collectively, the dissolved sulfide and sulfate profiles (Fig. **F4F**) suggest a broad zone centered between 25 and 150 mbsf where sulfate is reduced to sulfide. The presence of sulfide between 235 and 279 mbsf is consistent with the small inflection in the sulfate profile at 250 mbsf and further indicates a deeply buried zone of sulfate reduction. The broad maximum in sulfide corresponds to the maxima in the metabolic products DIC (Fig. **F4B**) and ammonium (Fig. **F4L**). In contrast to DIC and ammonium, the low solubility of metal sulfides results in the complete removal of sulfide at 281 mbsf. This depth approximately coincides with a transition toward higher dissolved iron concentrations downhole (Fig. **F4D**).

Ammonium concentrations rise from 22.4 µM at the top of the section to a maximum of 641 µM between 90 and 121.2 mbsf then decline more gradually downward, reaching 222 µM at 410 mbsf (Fig. **F4L**). The ammonium profile is similar to that obtained previously at Hole 846C (Shipboard Scientific Party, 1992). The shape of the ammonium profile is similar to the alkalinity and DIC profiles and mirrors the sulfate profile (Fig. **F4F**). Increased interstitial water ammonium, alkalinity, and DIC and decreased sulfate are consistent with the degradation of organic matter via bacterial sulfate reduction.

Concentrations of dissolved phosphate generally decrease from 8 to ~2 µM between 1.3 and 125 mbsf (Fig. **F4P**). Below 125 mbsf, phosphate declines smoothly, reaching a value of ~1 µM at 360 mbsf. Between 382.8 and 390.8 mbsf, phosphate concentrations are only ~0.3 µM.

Concentrations of acetate and formate were analyzed in 40 interstitial water samples from Hole 1226B (Table **T3;** Fig. **F4M, F4N**). Concentrations were generally higher than those at Site 1225 (see **"Biogeochemistry,"** p. 14, in the "Site 1225" chapter) and exceeded the detection limit in the majority of samples. Three distinct depth intervals can be distinguished: (1) concentrations of both compounds are below or around the detection limit between the sediment surface and

116.2 mbsf; (2) concentrations of both acetate and formate range between 0.4 and 1.2 µM between 116.2 and 274.7 mbsf; and (3) maximum concentrations of acetate and formate, from 1.1 to 4.3 µM and 0.7 to 2.2 µM, respectively, are present below 298.1 mbsf. The acetate profile has two distinct peaks at 336.50 and 409.6 mbsf, with values of 3.9 and 4.3 µM, respectively.

The stepwise increase in acetate and formate concentrations below 116.2 mbsf coincides with a sharp decline in total organic carbon (TOC) from ~0.5% to 0.1% (Shipboard Scientific Party, 1992) and the transition to lithostratigraphic Subunit 1B (see "Description of Lithostratigraphic Units," p. 8, in "Lithostratigraphy"). The depth interval from 116.2 to 274.7 mbsf also coincides with the plateau of maximum methane concentrations (Fig. F4K; see discussion below) and minimum sulfate concentrations. Presently, the significance of increasing acetate levels with increasing burial depth remains unclear. Wellsbury et al. (1997) showed that interstitial water acetate concentrations generally increase with temperature in sediments from the Blake Ridge. Temperature at the bottom of Site 1226 sediment reaches ~25°C (see "In Situ Temperature Measurements," p. 33, in "Downhole Tools").

Methane was detected in all samples from Hole 1226B (Table T5; Fig. F4K). No other hydrocarbons were detected. Maximum methane concentrations exceed 2 µM in the sediment horizon from ~80 to 300 mbsf. These concentrations are an order of magnitude higher than the maximum concentration found at Site 1225 in the same depth horizon. Notably and unlike at Site 1225, methane concentrations do not drop to zero above the sediment/basement interface.

Consistent with observations at Site 1225, the two procedures employed for extracting the dissolved methane led to different recoveries. On average, methane concentrations were slightly higher in samples that were extracted for 24 hr at room temperature than in samples extracted with the standard ODP technique used for safety purposes (Fig. F4K).

Incubations for hydrogen analysis were conducted on 13 samples from Hole 1226B and 4 samples from Hole 1226E (Table T6). The samples were incubated at temperatures close to the in situ sediment temperatures (4°, 13°, and 21°C) (see Table T6 for details). The temperatures were chosen based on the temperature profile modeled from the temperature tool data (see "Downhole Tools," p. 33).

Hydrogen concentrations in the incubations from Site 1226 are low (<1 nM) (Fig. F4O) compared to those at Site 1225 and measured by Hoehler et al. (1998) in shallow nearshore sediments. Concentrations ranged between 0.13 and 0.74 nM without any clear downhole trends. A more detailed consideration of the controls on hydrogen concentrations requires an analysis of free energies of the dissimilation reactions that involve hydrogen.

The dissolved interstitial silica profile at Site 1226 generally increases with depth over the upper 300 mbsf (Fig. F4Q), probably due to dissolution of amorphous biogenic silica (opal-A). The highest measured concentrations (1300–1400 µM) are present in lithostratigraphic Subunit IB between 275 and 315 mbsf. Overall, the downhole silica profile tracks variations in color reflectivity (see "Color Reflectance Spectrophotometry," p. 11, in "Lithostratigraphy"), with maxima corresponding to diatom-rich intervals. The pronounced decrease between 360 and 400 mbsf coincides with the presence of chert nodules and layers consisting of quartz (see "Mineralogy," p. 11, in "Lithostratigraphy"). Below this interval of low silica, concentrations sharply increase, although

T5. Methane in headspace, p. 88.

T6. Hydrogen concentrations, p. 89.

the onset of this rise cannot be resolved because of poor recovery. Toward basement, the concentrations drop as expected by the flow of silica-poor basement water.

Chloride concentrations increase from 553 mM near the sediment/water interface to 561 mM at a depth of 40.2 mbsf (Fig. F4R). This trend is most likely due to the diffusion of chloride from high-chlorinity glacial seawater out of the sediment column (e.g., McDuff, 1985). The values are relatively constant to a depth of 390.8 mbsf and then decrease to 552 mM at 413 mbsf. This near-basement decrease has at least two possible origins. Lower-chlorinity basement water is consistent with basement waters being derived from interglacial bottom waters. However, the diagenesis of chert in this part of the sediment column could also release water.

Sediments

Contents of TOC, calcium carbonate, total nitrogen, and total sulfur were not determined throughout most of the sediment column at Site 1226. However, they were determined on selected samples from representative intervals of Subunits IB (50–120 mbsf) and ID (260–310 mbsf) (Table T7). Samples were chosen to compare their chemical composition in relation to lithology, which alternates between nannofossil ooze and diatom ooze throughout Subunit IB and the upper part of Subunit ID (see "Unit I," p. 8, in "Description of Lithostratigraphic Units" in "Lithostratigraphy"). Total nitrogen and total sulfur concentrations are generally low or below detection limit. Notable differences in TOC content are present in adjacent layers of nannofossil ooze and diatom ooze, with the latter type commonly containing higher amounts of TOC and lower amounts of carbonate. Both the carbonate and TOC concentration data of Site 1226 are in agreement with data from respective intervals obtained at Site 846 (Shipboard Scientific Party, 1992) and provide a potential explanation for high-amplitude variation of TOC concentrations in the Site 846 data set. TOC and calcium contents throughout the sediment column were measured at Sites 851 and 846. In the upper 150 mbsf at Site 846, TOC typically exceeds 0.5%, with several values above 1% and a few approaching 2% (Shipboard Scientific Party, 1992). The average TOC contents of Site 846 are higher than those at Site 851. Maintenance of higher microbial activity by these higher TOC contents may account for alkalinity and DIC being higher at Sites 846 and 1226 than at Sites 851 and 1225.

MICROBIOLOGY

Microbiological samples were taken from every core of Hole 1226B at intervals of ~9.5 m for complete profiles of sulfate reduction rates, carbon, hydrogen, nitrogen, and sulfur (CHNS) geochemistry and deoxyribonucleic acid (DNA) analysis (Fig. F5). This basic sampling scheme was maintained throughout Hole 1226B. More extensive sampling focused on variable depth intervals in Hole 1226B throughout the sediment column but particularly emphasized the top and bottom layers of the sediment column, which are characterized by the steepest geochemical gradients (see Fig. F4). Between the sediment surface and Core 201-1226B-12H, the third section of every second core was sampled in an extensive manner. In the central portion of the sediment column (Cores 201-1226B-12H through 30X), the third section of every

T7. C, N, and S, p. 90.

F5. MBIO subsampling, Hole 1226B, p. 49.

third core was taken. Additionally, samples for fluorescence in situ hybridization (FISH), adenosine triphosphate (ATP), and lipid biomarker analysis were fixed or frozen, as appropriate, for selection and processing of the most promising and representative material on shore. Also, whole-round cores were subsampled into 5-cm³ syringes for subsequent measurement of methanogenesis, acetate turnover, and thymidine incorporation into DNA. Samples for acridine orange direct count (AODC) were fixed from the same intervals, and the cells were counted on the ship. Samples for anaerobic oxidation of methane, pyrolysis of organic material, and diffusion experiments were taken at several defined intervals (Fig. **F5**).

Based on our initial experience at Site 1225 (see **"Contamination Tests,"** p. 20, in "Microbiology" in the "Site 1225" chapter), modifications to minimize contamination and to increase handling efficiency were introduced at Site 1226. Details are given in **"Microbiology,"** p. 14, in the "Explanatory Notes" chapter. In contrast to Site 1225, interstitial water samples were always taken on the catwalk, either from intervals adjacent to the microbiology samples or from additional core sections.

Samples were taken for microbial enrichments and MPN quantifications with the aim of comparing distinct depths and chemical zones in the sediment column. Samples for slurry preparation and for cultivation of manganese reducers were taken from the surface or near-surface sediment (Cores 201-1226B-2H and 201-1226E-1H), from intermediate depths near 100, 200, 310, and 380 mbsf (Cores 201-1226B-12H, 22H, 34X, and 43X), and from the deepest core at 420 mbsf (Core 201-1226B-47X) (Fig. **F5**). An additional sample for manganese reducers and other cultivations was taken near 300 mbsf (Core 201-1226E-18H).

Starting from Core 201-1226B-30X (281.5 mbsf), where coring switched from APC to XCB, core quality deteriorated because of high levels of seawater infiltration, which gave the sediment a mushy consistency. Elevated levels of perfluorocarbon (PFC) contamination were found in the disturbed portions of XCB cores, for example in Cores 201-1226B-30X and 40X (Table **T8**). In such cases, the remaining portions of consolidated sediment ("biscuits") were collected for a reduced sampling program that was improvised under the circumstances (see **"Biscuit Sampling,"** p. 23). The full sampling program resumed for Cores 201-1226B-45X, 46X, and 47X at the bottom of Hole 1226B.

Microbiological sampling in Hole 1226E focused on several additional depths to complement the microbiological profiles obtained in Hole 1226B and to fill sampling gaps (Fig. **F6**). The mudline core of Hole 1226E was sampled at three depths (in Sections 201-1226E-1H-1, 1H-3, and 1H-5) to obtain finer resolution near the sediment surface, where the steepest biogeochemical gradients had been encountered during ODP Leg 138 and confirmed by interstitial water analyses from Hole 1226B (Fig. **F4**). An additional sample for cultivation of manganese-reducing bacteria in Hole 1226E at 300 mbsf was chosen according to the analyzed manganese profile of Hole 1226E, which showed a conspicuous manganese peak at that depth (Fig. **F4**).

In Hole 1226E, a continuous APC sample series focused on the layers below 260 mbsf that had been sampled by XCB coring in Hole 1226B. Starting with Core 201-1226E-16H, every second core was sampled according to the full program sampling scheme down to 326 mbsf (Fig. **F6**).

To explore the composition of microbial communities associated with oceanic crust and their contribution to basalt weathering, XCB

T8. Contamination based on PFT, p. 91.

F6. MBIO subsampling, Hole 1226E, p. 50.

drilling into basement rock was performed (Core 201-1226B-47X; 421.4 mbsf). The core catcher yielded fragments of basaltic rock that were sampled separately using a specially designed sample processing scheme (see "Rock Sampling and Distribution," p. 24).

Total Prokaryote Enumeration

Samples of 1-cm^3 plugs for prokaryote enumeration were taken on the catwalk from a total of 36 core sections at depths between 0.01 and 7.3 mbsf in Hole 1226E (4 samples) and between 8.85 and 420 mbsf in Hole 1226B (32 samples). Additionally, 2-mL samples or 25% slurry were taken from five slurries prepared in the laboratory (see "Total Prokaryotic Cell Counts," p. 25, in "Procedures and Protocols" in "Microbiology" in the "Explanatory Notes" chapter). Slurries were made from Cores 201-1226B-2H, 12H, 22H, 43X, and 47X and from Core 201-1226E-1H.

Prokaryotes were present in 24 samples from the near surface to 419.4 mbsf (Fig. F7). Prokaryotes were not detected in the lowest sample at 420 mbsf. The highest number of prokaryotic cells was found in the near-surface sample (201-1226E-1H-1, 0–1 cm), which contained 4.63×10^8 cells/cm^3. The overall depth profile of cell numbers per cubic centimeter follows a trend observed at other ODP sites (Parkes et al., 1994); however, cell numbers are substantially lower than the average previously observed trend in the upper few meters and remain lower than average to 40 mbsf (Fig. F8). The profile then conforms well from ~40 mbsf to near basement at 419.4 mbsf, except for an additional reduction in cell numbers between 90 and 170 mbsf. All data fit within 2 σ of the average previously observed trend over the depths between 8.9 mbsf (Sample 201-1226B-2H-3, 145–150 cm) and 419.4 mbsf (Sample 47X-2, 145–150 cm).

Numbers of dividing cells (suggested as an index of growth) are typically <10% of the total count. As expected, dividing cells as a percentage of the total count are high near the surface (Fig. F7) and decrease to a minimum at 113 mbsf (Sample 201-1226B-13H-3, 145–150 cm). The percentage of dividing cells then increases until 295.3 mbsf (Sample 201-1226B-32X-3, 145–150 cm), where 13.4% of the total was observed to be dividing. Below 320 mbsf, three of the five measurements did not detect any dividing cells. However, there are indications of a second peak in dividing cells between 368.4 and 381 mbsf (Samples 201-1226B-40X-1, 29–33 cm, and 43X-3, 145–150 cm).

Total counts were performed on five of the six slurry samples. The prokaryotic populations present in laboratory slurries were compared to those in adjacent plug samples taken for total counts using a two-way analysis of variance with interaction. There was no significant difference between the samples (F-value = 0.56; degrees of freedom = 1 and 14; interaction not significant).

Contamination Tests

While drilling cores for microbiology, the potential for contamination with bacteria from the surface is highly critical. Contamination tests were continuously conducted using solutes (PFT) or bacterial-sized particles (fluorescent microspheres) to check for the potential intrusion of drilling water from the periphery toward the center of cores and thus to confirm the suitability of the core material for microbiological research. We used the chemical and particle tracer techniques described

F7. Prokaryotic cells enumerated, p. 51.
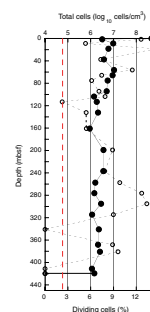
F8. Total prokaryotic profile, p. 52.
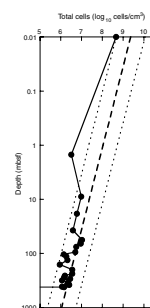
in ODP *Technical Note* 28 (Smith et al., 2000). Furthermore, the freshly collected cores were visually examined for possible cracks and other signs of disturbance by observation through the transparent core liner. Core sections observed to be disturbed before or after subsampling were not analyzed further. Such disturbance phenomena are critical to the integrity of the core material and therefore also to its usefulness for microbiological studies.

Perfluorocarbon Tracer

The PFC tracer (see "Perfluorocarbon Tracer Contamination Tests," p. 26, in "Procedures and Protocols" in "Microbiology" in the "Explanatory Notes" chapter) was injected continuously into the drilling fluid during drilling of Holes 1226B and 1226E. With a few exceptions, 5-cm³ subcores were taken from the bottom cut of each microbiology (MBIO) section or from the adjacent top of the immediately underlying section, as well as from 5-mL aliquots of each master slurry for contamination monitoring. In addition, samples from Section 201-1226B-47X-CC were collected to measure the concentration of PFT.

In all cases where PFT concentrations were below the detection limit, the delivery of PFT to the drill bit was positively confirmed by measuring the concentration of PFT in drilling fluid removed from the top of the core or by detection of PFT in sediment smeared along the edge of the core. At Site 1226, careful catwalk sampling and revised gas chromatography (GC) protocols (see "Microbiology," p. 14, in the "Explanatory Notes" chapter and House et al., this volume) resulted in lower detection limits (~0.02 µL seawater contamination/g sediment or ~0.025 µL seawater contamination/mL slurry) than those at Site 1225.

Given these detection limits, the results (Table T8) indicate very low levels of surface seawater contamination for APC subcores, with most having contamination levels of ~0.04 µL seawater drilling fluid/g sediment. Of the 21 APC cores sampled, only two had PFT concentrations indicating seawater contamination of >0.1 µL seawater/g sediment. XCB cores were generally more contaminated. PFT concentrations in subcores taken on the catwalk from XCB cores had as little as 0.03 µL seawater/g sediment (Section 201-1226B-43X-4) or as much as 4.08 µL seawater/g sediment (Section 201-1226B-30X-4), with one-half of the XCB catwalk subcores showing ≤0.29 µL seawater/g sediment. The mean level of seawater contamination observed for subsamples taken from within intact biscuits of sediment from an XCB core was 0.24 µL seawater/g sediment. This was also close to the level of seawater contamination observed in a subcore of a 4-cm biscuit removed from Core 201-1226B-43X, broken open, and carefully subsampled for PFT analysis (Fig. F9). Two samples taken from the core catcher of Core 201-1226B-47X were analyzed for PFT concentration. The first was a piece of breccia that showed a high degree of seawater contamination (~1.8 µL seawater/g sediment), and the second was the crushed internal part of a carefully washed and sterilized rock sample. In contrast to the piece of breccia, the internal part of the washed and sterilized sample showed low levels of PFT, representing ~0.05 µL seawater/g sediment. This finding demonstrates that careful subsampling of hard rock material from the core catcher can result in microbiologically clean samples. Of the five master slurry samples taken from Site 1226, only the slurry from Core 210-1226B-2H showed a moderate concentration of PFT (representing ~0.3 µL seawater/mL slurry), whereas PFT concentration was below the detection limit in the others (Table T9). Finally, the PFT concen-

F9. "Biscuit," p. 53.

T9. Potential contamination of slurries based on PFT, p. 92.

trations in three samples of interstitial water taken from XCB cores were analyzed. These samples showed higher levels of PFT than microbiological samples from the same cores, with an average contamination of ~0.5 µL seawater/mL interstitial water. However, the increased level of PFT in these samples may be a result of handling of samples during interstitial water pressing rather than a result of contamination by drilling fluid.

Background levels of PFT in various laboratories showed between undetectable levels and up to 9×10^{-12} g/mL air. Because of the high variability, no adjustment was made for laboratory air PFT contamination for these interstitial water samples. However, very high air levels of PFT were found in samples taken from the cold room (1.8×10^{-10} g/mL air). To avoid background problems, fresh samples were either carried from the laboratories onto the catwalk and capped in the open air, which had repeatedly tested PFT negative, or they were corrected for background readings of laboratory air. All values in the Table T8 are corrected for background.

Assuming 5×10^8 prokaryotic cells/L surface seawater, each 0.1 µL of seawater contamination may represent as many as 50 contaminating cells, if the sediment is porous enough to allow cells to travel with the PFT. However, the only slurry with detectable amounts of PFT (prepared from Core 201-1226B-2H) did not contain beads, indicating that prokaryotic cell mimics were not entrained into the sediment samples. Beads appear in this case to be a more realistic tracer of prokaryotic cells (see below).

Particulate Tracer

Fluorescent beads (5×10^{11} beads/core) were deployed on all five cores from which slurries were subsequently made in the laboratory. Only on the last core run for slurries (Core 201-1226E-1H) did the bag with bead suspension fail to burst and beads were not deployed. For each slurry, three subsamples were processed: (1) a sample of the slurry, (2) a sample tenfold diluted in 2% formaldehyde (used also for direct cell counts), and (3) a scraping from the outer surface of the core (processed to confirm deployment of beads).

Beads were detected in three of the slurries (Table T10). However, in the first slurry (Section 201-1226E-1H-1) this was due to a procedural error during processing. Absence of beads was confirmed from the vial sample. For the other two positive slurry samples (Sections 201-1226B-22H-3 and 43X-2), only a single bead was detected and it is believed this was probably due to sample handling rather than contamination. The counting procedure was modified at this site by viewing the filter membrane under a 63× objective rather than a 100× objective. This had the effect of increasing coverage of the filter membrane from ~9,000 µm²/field of view to 22,800 µm²/field of view, so raising the sensitivity by a factor of 2.5. The eyepiece counting grid covers approximately one-third of a field of view. For both the samples above, only a single bead was found after thorough searching. In both cases, processing the vial sample indicated a negative result. This finding suggests that handling of the bead samples rather than contamination during coring was the problem. Handling protocols were further improved for subsequent sites.

Cultivations

Slurries for cultivation were usually prepared by subcoring with two 60-mL syringes from the center of two freshly broken surfaces (after precutting the core liner with the ODP cutter). This represented a change in method from Site 1225 (see "Cultivations," p. 21, in "Microbiology" in the "Site 1225" chapter and "Cultivation of Microorganisms," p. 28, in "Procedures and Protocols" in "Microbiology" in the "Explanatory Notes" chapter). From Sections 201-1226B-43X-3 and 47X-1, slurries were prepared by breaking cleaned biscuits (see "Biscuit Sampling" below) and removing material from the inner untouched surfaces with sterile scalpels.

All MPN dilutions and enrichments inoculated using samples from Site 1226 are listed in Table T11. A strong indication for manganese(IV) reduction was given by the dissolved manganese interstitial water profile, which showed pronounced peaks of dissolved manganese close to the sediment surface and at 300 mbsf (see Fig. F4). At 350 mbsf the dissolved manganese concentrations show a minimum and increase toward the bottom of the hole to concentrations that are even higher than at the surface of the sediment. Consequently, MPN enrichments of manganese(IV)-reducing prokaryotes focused on this interval.

After the first few days of incubation, there was growth of rod-shaped cells in one enrichment assay at 25°C (room temperature) on medium 201-3 (see Table T5, p. 85, in the "Explanatory Notes" chapter), designed for anaerobic heterotrophs with nitrate as the electron acceptor. The culture was inoculated with sediment from Section 201-1226B-34X-3. This first positive result needs to be confirmed by further subculturing and by verifying with molecular data. Furthermore, the potential for previous contamination of the samples used for enrichment must be considered (see "Contamination Tests," p. 20).

FISH-SIMS

[13]C substrate incubations were initiated for postcruise analysis by FISH-secondary ion mass spectrometry (SIMS) using material from Cores 201-1226B-2H and 12H. In this case, 10 mL of the master slurry was injected into each bottle. The ^{13}C substrates used were methane, acetate, or glucose. However, for Core 201-1226B-12H, the ^{13}C acetate bottle had nonlabeled methane in the headspace.

Biscuit Sampling

Sediment cores recovered by XCB commonly had a mushy consistency because of mechanical disturbance and infiltration of drilling fluid. Such cores contained relatively few undisturbed portions, referred to in ODP parlance as biscuits. A biscuit is a hard, round to ellipsoidal or subcylindrical clump of sediment (3–7 cm in diameter, occasionally as long as 15 cm in length) that fails to break with hand pressure between the fingers and thumb (Fig. F9). Biscuits that fractured along planes with hand pressure were discarded because wet spots were commonly present along the fracture surfaces and were shown by PFT analysis to be contaminated (see "Contamination Tests," p. 20). In Hole 1226B, Cores 201-1226B-30X and deeper were recovered as XCB cores. Mushy sediment consistency was noticed in cores and sections deeper than Section 201-1226B-32X-3. Less than 10% of the sediment volume was recovered as usable biscuits in Cores 201-1226B-33X through 35X.

T11. Media inoculated with material from Site 1226, p. 94.

From these and subsequent cores, biscuits were recovered, kept under nitrogen for 1–4 hr, and sampled according to the following scheme:

1. Section 201-1226B-33X-4: biscuits were sampled for DNA and solid-phase iron, manganese, and sulfur analyses and FISH. To increase the amount of material collected, these samples were mixed with biscuits from the next section (201-1226B-34X-3) and have to be regarded as mixed samples with contributions from both cores.
2. Samples from Sections 201-1226B-35X-3 and 35X-4: biscuits were collected for activity measurements (hydrogen turnover, sulfate reduction rates, etc.)
3. Section 201-1226B-43X-2: ~60 cm of a 150-cm core section was collected as mostly 6- to 10-cm-long biscuits. Three 10- to 15-cm-long biscuits were used for slurry preparation and cultivations. Thirteen smaller biscuits (6–10 cm long) were used for DNA samples. Material for activity measurements was set aside under nitrogen but was not used.

Cores 201-1226B-45X and 46X exhibited no mushiness and biscuit formation and were cut and subsampled as described in **"Core Handling and Sampling,"** p. 15, in "Introduction and Background" in "Microbiology" in the "Explanatory Notes" chapter and in Figure **F5.** With Core 201-1226B-47X, the biscuit sampling protocol was used for slurry preparation, whereas other samples were taken by the routine procedures.

Rock Sampling and Distribution

Several individual pieces of rock of various sizes as large as 4.5 cm (dark gray to black basalt) were obtained from the core catcher of the lowermost core (201-1226B-47X). Furthermore, a large round rock piece was obtained that initially appeared to be a solid core sample of ~8 cm in length but broke into two smaller pieces during cleaning and investigation. These pieces were grayish green and contained pieces of gray-black weathered basalt (up to ~3 cm in length). A few of these weathered basalt fragments contained small red inclusions (tentatively identified as hematite). The cracks in the basalt were filled with white crystalline material that was visible when examined with a dissecting microscope. The white material is assumed to include calcite, as some could be removed with 3-M HCl treatment. Further examination suggested that the large core piece contained coring debris around a natural conglomerate (breccia). With a sterile spatula, the two pieces were broken into successively smaller pieces to obtain fresh uncontaminated surfaces from which material (16.6 g) for inoculations was obtained with a sterile scalpel. Some of the softer black material could be shaved off with a scalpel. Material from the inside of a freshly broken surface (3 g) showed a high concentration of the PFT tracer, indicating seawater contamination (Table **T8**). However, the same material was found to be free of fluorescent beads. Softer, partly creamy material from the outer rim (after scratching off the outer 2 mm), was obtained as control material (drilling fluid–contaminated inocula). The following enrichment media (see Table **T5,** p. 85, in the "Explanatory Notes" chapter) were inoculated with ~1 g of the inner rock or, as a control, with the outer rim material: H_2/HCO_3^-, $H_2/HCO_3^-/Fe(III)$, and a mixture of FERM-gluc-8.0 and FERM-xyl-8.0. Except for the $H_2/HCO_3^-/Fe(III)$

media, one tube each was prepared for anaerobic or for aerobic (head-space of air:nitrogen = 1:3) incubations. One set was incubated at 60°C and the other set at room temperature (20°–26°C). Pieces broken off from inside of the rock and some shaved-off material were kept in sterile nitrogen-flushed glass vials at 4°C for postcruise molecular work and further enrichments.

One piece of basalt from Section 201-1226D-47X-CC (Fig. **F10**) was washed with sterile nitrogen-flushed marine salts solution, crushed in the sterile shipboard rock crusher (see **"Rock Sampling,"** p. 35, in "Procedures and Protocols" in "Microbiology" in the "Explanatory Notes" chapter), and used for inoculation of various culture media. The wash water from the sample had the consistency of a diluted sediment slurry (~250 mL with 5% sediment) and was used as inoculum for controls and for testing for the presence of contaminating surface microbes.

The following enrichments were initiated:

1. Anaerobic polymer degrader (Poly), aromatic compounds degrader (Aro), and heterotrophs (Sed) (see **"Methods for Enrichment and MPN,"** p. 28, in "Procedures and Protocols" in "Microbiology" in the "Explanatory Notes" chapter) incubated at room temperature;
2. Anaerobic chemolithoautotrophs using hydrogen as electron donor and iron(III) or manganese(IV) as electron acceptor (A-bas) (see **"Methods for Enrichment and MPN,"** p. 28, in "Procedures and Protocols" in "Microbiology" in the "Explanatory Notes" chapter), incubated at room temperature;
3. Anaerobic chemolithoautotrophs using hydrogen as electron donor and either iron(III) ion ($H_2/HCO_3^-/Fe[III]$, 7.8), manganese(IV) ($H_2/HCO_3^-/Mn[IV]$, 7.8), CO_2 (H_2/HCO_3^-, 7.8), or sulfate (SRB-8.0) (see **"Methods for Enrichment and MPN,"** p. 28, in "Procedures and Protocols" in "Microbiology" in the "Explanatory Notes" chapter) as electron acceptor at 60°C;
4. Anaerobic heterotrophs with the media FERM-gluc and FERM-xyl (see **"Methods for Enrichment and MPN,"** p. 28, in "Procedures and Protocols" in "Microbiology" in the "Explanatory Notes" chapter) at 60°C; and
5. Aerobic hydrogen-utilizing chemolithoautotrophs (H_2/HCO_3^-/50% air) (see **"Methods for Enrichment and MPN,"** p. 28, in "Procedures and Protocols" in "Microbiology" in the "Explanatory Notes" chapter) at room temperature.

In addition, 3.2 g of the HCl-washed and crushed material was stored at 4°C and will be used for postcruise analysis including scanning electron microscopy, electron probe microanalyzer, and XRD analyses.

One piece of basalt was only washed several times with sterile saline solution and then used directly for enrichment of anaerobic iron(III) and manganese(IV) reducers at room temperature. Several of the blackish rock pieces (either directly from the core catcher or from the crumbling piece of breccia) were kept for postcruise experiments. Two pieces (washed in ethanol:phosphate buffered saline [PBS] and stored at –20°C) will be analyzed by FISH-SIMS (see **"Sample Preparation for FISH-SIMS,"** p. 38, in "Molecular Analysis" in "Procedures and Protocols" in "Microbiology" in the "Explanatory Notes" chapter).

F10. Basalt from an XCB core catcher, p. 54.

PHYSICAL PROPERTIES

At Site 1226 we collected a full range of physical property data from the sediment/water interface to immediately above basalt basement. The data are described below and compared with those from Site 846. At Site 846, APC coring ended at Core 138-836B-22H (206.6 mbsf). In Hole 1226B, APC coring extended to a depth of 271.9 mbsf (Core 201-1226B-29H) and in Hole 1226E to a depth of 326.0 mbsf (Core 201-1226E-20H). This allowed us to extend the depth of reliable physical property data by ~120 m. In addition, we collected IR emission and electrical resistance data that were not collected at Site 846.

Whole-round cores were first scanned for IR emission on the catwalk prior to sectioning. Immediately after sectioning, exposed section ends adjacent to the interstitial water and microbiology sections were IR scanned for temperature determination. The cores were then equilibrated to the laboratory temperature, and each section was run on the multisensor track (MST). The measurements made on the MST were magnetic susceptibility (spacing = 5 cm, data acquisition scheme [DAQ] = 2×1 s), gamma ray attenuation (GRA) bulk density (spacing = 10 cm, count time = 5 s), P-wave velocity (spacing = 10 cm, DAQ = 10), and natural gamma radiation (NGR) (spacing = 30 cm, count time = 15 s). Thermal conductivity measurements were made on the third section of each whole-round core in Hole 1226B. MST data were collected on cores from Holes 1226A, 1226B, 1226C, 1226D, and 1226E. IR emission and thermal conductivity measurements were made only on Hole 1226B cores. Some sections were removed from the catwalk for microbiology and interstitial water sampling. Physical properties were measured on these sections only if intact parts remained following the sampling. The likelihood of this declined after we switched from APC to XCB coring.

After splitting we took discrete undisturbed samples from each core for measuring moisture and density (MAD) (dry volume and wet and dry mass). We also measured compressional wave velocities using the digital sonic velocimeter and resistance using a third-party device.

Our sampling strategy was designed to address specific leg and related research objectives while maintaining core flow through the laboratory. Hole 1226A was scanned on the MST but not sampled for moisture and density. A full suite of physical property measurements in whole- and split-core mode were conducted on Hole 1226B cores, which extended from the sediment/water interface to the basalt basement. Hole 1226C comprised a single mudline core that was run at higher resolution and precision on the MST but without discrete MAD and P-wave data. Holes 1226D and 1226E were logged at the same rates as 1226B (see above); Hole 1226D was a disrupted mudline core, and Hole 1226E focused on areas of interest identified from Hole 1226B data. Voids and cracking were logged for the MST where separation was visible, and data were not recorded over these intervals.

MAD data, P-wave measurements from the velocimeter, and resistance data were collected only from Hole 1226B because of the high degree of correlation between the Site 846 and Hole 1226B MST data. Two MAD samples were taken per section for the top 60 m (Sections 201-1226A-1H-1 through 6H-7) and, where possible, for the lowermost 90 m (Sections 36X-1 through 47X-2). In between, MAD properties were measured at one per section. In sections where methane samples were collected, the MAD samples were co-located with the methane samples.

Spot sampling of MAD was also carried out in Hole 1226E in order to confirm Hole 1226B measurements.

MAD measurements were uploaded to the ODP (Janus) database and used to calculate water content, bulk density, grain density, porosity, void ratio, and dry bulk density. PWS3 data were collected on all sections. Resistance measurements were used to compute formation factors for Hole 1226B and were compared with porosity data.

Instrumentation and measurement principles are discussed in "Physical Properties," p. 41, in the "Explanatory Notes" chapter.

Infrared Scanner

Each core from Hole 1226B was scanned from top to bottom on the catwalk with an IR camera, except where there were problems booting the camera and/or computer. As mentioned in "Infrared Scanner," p. 24, in "Physical Properties" in the "Site 1225" chapter, extensive postcruise processing is needed to create a downcore scale. Therefore, correlations with other physical properties are not possible at this preliminary stage. However, in order to gain a greater understanding of the factors involved with taking accurate temperature measurements on the cores, we examined temperature profiles generated along different longitudinal sections of core to determine if reflection significantly alters the surface temperature. We briefly examined the differences between IR scanning during the day and night and between APC and XCB cores. Emissivity of a representative sample of mud from this site was established in order to obtain accurate temperature measurements of the section ends when they are cut on the catwalk.

The well-focused IR scan of Core 201-1226B-13H was selected to generate multiple core liner temperature profiles. The profiles differ by location of the profile line on the core liner (Fig. F11). The temperature range covered by the profiles was 18.2° to 20.7°C. The variation between profile measurements was 0.63°C, on average, with a maximum variation of 1.4°C (Fig. F11B).

A preliminary comparison of night and day scans was done by visual interpretation of the core scans using the IR software. The only noticeable difference was in the visibility of the scale. It appears that at night it is more visible on the image than during the day.

The disturbance associated with XCB coring, as well as areas where there was poor contact between the sediment and the core liner, were not identifiable with the current infrared scanning configuration. However, a large void (~30 cm) at the bottom of Core 201-1226B-43X was identifiable in the core liner images by its higher temperature (Fig. F12).

Emissivity (*e*) was determined using a residue from Sample 201-1225C-30H-6, 74.5–76.5 cm. A piece of electrical tape with a known emissivity (*e* = 0.95) was placed on the surface of the sediment. The temperature at the outer surface of the tape read by the IR camera was 27.4°C, and a thermistor inserted in the sediment directly beneath the tape confirmed that 27.4°C was the temperature of the sediment. The surface temperature of exposed sediment (i.e., not covered with tape) immediately adjacent was measured by the camera as 26.4°C (Fig. F13A). The emissivity of the camera was then adjusted so that the exposed sediment gave a temperature reading of 27.4°C (Fig. F13B). This resulted in an empirical value for the sediment emissivity of 0.84. This emissivity was subsequently used to recalibrate the temperature measurements of the section ends measured on the catwalk.

F11. Lines and core liner temperature profiles, p. 55.
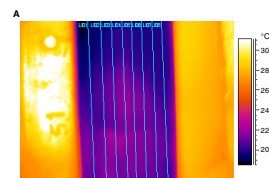
F12. IR scan of void at end of core, p. 57.
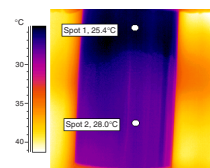
F13. Sediment emissivity using tape as control, p. 58.
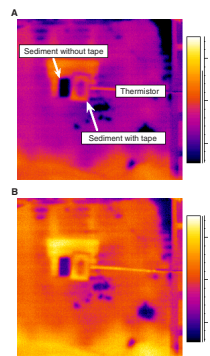
Magnetic Susceptibility

Low-field volume magnetic susceptibility was measured on the MST using the Bartington loop sensor as described in "Magnetic Susceptibility," p. 44, in "MST Measurements" in "Physical Properties" in the "Explanatory Notes" chapter. The data correlate well with the Site 846 data across the entire downhole profile (Fig. F14).

Average magnetic susceptibility is very low from 0 to 265 mbsf, varying between slightly negative and ~2 × 10^{-5} SI units, essentially indicating the absence of ferrimagnetic minerals. There is a very slight shift to more negative values at 52 mbsf, which correlates with the lithologic boundary between lithostratigraphic Subunits IA and IB. Between 50 and 120 mbsf, a meter-scale cyclicity in the magnetic susceptibility and reflectance data are inversely correlated (Fig. F15). Using an average sedimentation rate of 40 k.y./m (Site 846; Shipboard Scientific Party, 1992), preliminary spectral analysis suggests these are Milankovitch precessional cycles. The origin of the signal is intriguing because negative susceptibilities correlate with high values in the ratio of red-green to blue electromagnetic (EMR) spectral reflectivity, which is the opposite of the expected response. More commonly, a darker color, reflecting higher organic content, correlates with low or absent magnetite. We suspect the inverse correlation may be a function of the water content of the sediment, as water has a slightly negative magnetic susceptibility (–0.72 × 10^{-6} cgs units) (Carmichael, 1982, p. 270). Although the chromaticity value results from a more complex computation, it probably also reflects the wavelength-specific interaction of EMR and water.

Leg 138 scientists started XCB coring at 207 mbsf, whereas we extended APC coring to 326 mbsf. Between these depths, the two data sets remain very well correlated, including the slight increase at 264 mbsf. This suggests that the coring method does not adversely affect the susceptibility measurements at meter-scale resolution. Particularly, the peak of nearly 50 × 10^{-5} SI units centered on depth of 243.5 mbsf is real.

The average value of magnetic susceptibility steps up to ~3 × 10^{-5} SI units at ~264 mbsf, which is approximately coincident with the Subunit IC/ID lithostratigraphic boundary at 272 mbsf. This is coincident with a decrease in reflectance (see "Color Reflectance Spectrophotometry," p. 11, in "Lithostratigraphy"). Below 264 mbsf (the top of Subunit ID), magnetic susceptibility increases to a peak of ~10 × 10^{-5} SI units at a depth of 290 mbsf. It then declines to a low for Subunit ID at a depth of ~300 mbsf. Between 300 and 315 mbsf, it increases sharply to a peak of ~25 × 10^{-5} SI units and falls back to 6–8 × 10^{-5} SI units at ~325 mbsf. From this depth to the base of Unit I (400.12 mbsf) the susceptibility steadily increases to an average value of ~25 × 10^{-5} SI units.

Magnetic susceptibility continues to increase across Unit II to the base of the hole, where it reaches a downhole maximum of ~45 × 10^{-5} SI units.

Paleomagnetism

At Site 1226, we collected 29 discrete samples for paleomagnetic measurements from Hole 1226E, which was not continuously cored. The sampling frequency was one sample from each core for Cores 201-1226E-9H through 14H (70.9–269.0 mbsf) and two samples from each core below this interval to the bottom of the hole (Cores 201-1226E-15H through 25X; 269.0–418.4 mbsf). Alternating-field (AF) demagnetization of the natural remanent magnetization (NRM) was conducted up

F14. MST magnetic susceptibility, p. 59.
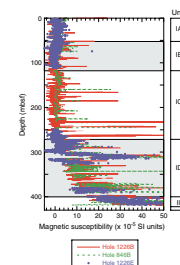
F15. Reflectance and magnetic susceptibility, p. 60.
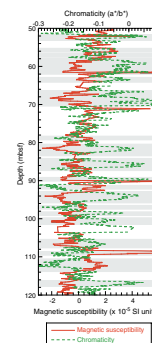
to 40 mT in 10- or 5-mT steps. Anhysteretic remanent magnetization (ARM) was measured to 40 mT in 10-mT steps with a 29-µT direct current–biasing field. AF demagnetization of the ARM was conducted to 40 mT in 10-mT steps on ~24 samples. Additional samples will be processed by stepwise thermal demagnetization on shore.

Magnetic intensity and susceptibility increase in lithostratigraphic Subunit ID below 300 mbsf (see "Subunit ID," p. 10, in "Unit I" in "Description of Lithostratigraphic Units" in "Lithostratigraphy") (Fig. F16). White clay- and radiolarian-bearing diatom-rich nannofossil ooze (Sample 201-1226E-18H-6, 55–57 cm) and pale yellow diatom-bearing nannofossil ooze (Sample 20H-5, 54.5–56.5 cm) in the upper and middle parts of lithostratigraphic Subunit ID show three magnetic components, including a downward drilling-induced overprint and two horizontal components (Fig. F17). In the lower part of lithostratigraphic Subunit ID, a pale yellowish white diatom-bearing nannofossil chalk with pale gray laminae (Sample 201-1226E-22X-5, 54.5–56.5 cm) has a stable downward inclination (Fig. F18).

Light reddish brown to brown foraminifer- and diatom-bearing clay-rich nannofossil chalk containing hematite in the lower part of lithostratigraphic Unit II directly overlies the oceanic basement. A dominant light brown layer (Sample 201-1226E-25X-3, 112–114 cm) and a dark brown layer (Sample 25X-CC, 13–15 cm) at the bottom of Hole 1226E show stable magnetic directions after removing the drilling overprint by 15-mT AF demagnetization (Figs. F19, F20).

Density and Porosity

Density data were measured on the MST by the GRA densitometer (spacing = 10 cm, count time = 5 s) and were calculated from the moisture and density data. Comparison of GRA data from Holes 1226B and 1226E relative to Hole 846B data reveals a consistent high-resolution density profile (Fig. F21). Figure F22 displays a 5-m moving average of the GRA density estimates from Holes 1226B and 846B, showing that the two surveys are statistically identical except between (1) ~210 and 270 mbsf, corresponding to the extended interval of advanced piston coring during Leg 201, and (2) ~375 and 410 mbsf, where the Hole 846B data erroneously predicted a density decrease in the increasingly consolidated sediments (see "Lithostratigraphy," p. 7).

GRA density increases from 1.20 to 1.52 g/cm³ from 0 to 15 mbsf and then declines back to a low of ~1.20 g/cm³ at 52 mbsf. Below 52 mbsf, GRA density first increases to ~1.52 g/cm³ at a depth ~120 mbsf and remains at 1.52 g/cm³ until ~250 mbsf. At 250 mbsf, it starts to decrease to a low of 1.22 g/cm³ at 300 mbsf. From 300 mbsf to the bottom of the hole, it increases to the downhole maximum of 1.74 g/cm³. This complex profile was interpreted to be controlled by sediment accumulation rate and mix of nannofossil-diatom components (Shipboard Scientific Party, 1992) (see "Lithostratigraphy," p. 7). Regular or cyclic downhole variability in GRA density data has a spatial frequency on a scale of ~10 m.

Moisture and density measurements for Hole 1226B (Fig. F23) compare favorably to both Leg 201 GRA-derived and Leg 138, Hole 846B GRA-derived values (Fig. F22). The bulk density and porosity profiles are clearly controlled by grain density fluctuation tied to the diatom/nannofossil ratio. Sharp grain density decreases at the tops of Subunits IB and ID are precise indicators of diatom enrichment and are accompa-

nied by sharp porosity increases resulting from the large open frustules. Subunit IC is composed of nannofossil ooze with grain densities generally between 2.58 and 2.68 g/cm³; porosity within this interval declines with depth consistent with one-dimensional consolidation models (Athy, 1930). Below the diatom-enriched interval at the top of Subunit ID (272–320 mbsf), increasing clay and siliciclastic content (see "Lithostratigraphy," p. 7) increase grain densities from ~2.62 to 2.82 g/cm³ at the top of Unit II (400 mbsf). The rapid porosity decrease from 320 mbsf to the top of Unit II probably reflects both a trend of increasing consolidation and clay infilling of the chalk pore structure.
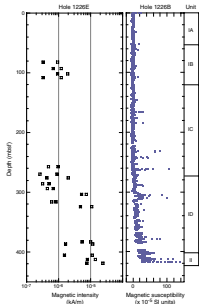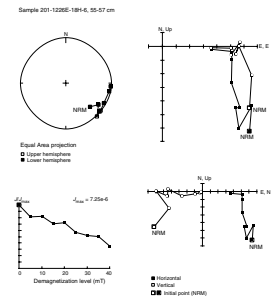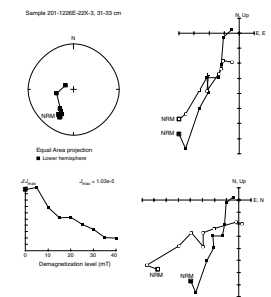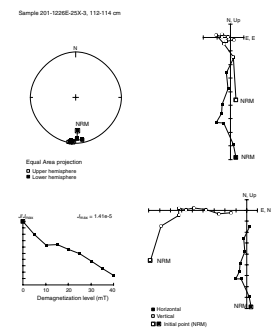
Compressional Wave Velocity

P-wave data from the MST *P*-wave logger (PWL) were recorded (spacing = 10 cm, DAQ = 10) for all APC cores from Holes 1226A through 1226E. The PWS3 velocimeter was used to measure *P*-wave velocities transverse to the core axis on all split cores from Hole 1226B, with measurements taken at two per section for Cores 201-1226B-1H through 6H, one per section for Cores 7H through 35X, and at least one per section for Cores 201-1226B-36X through 47X. Additional PWS3 measurements were made on split cores from Hole 1226E (Cores 201-1226E-18H through 20H and 22X and 25X), with sample cubes extracted from intact core sediments tested to provide information on drilling disturbance effects in XCB cores.

PWL measurements range from 1480 to 1520 m/s for both Holes 1226B and 1226E for the 0- to 272-mbsf interval (Subunits IA–IC), with depth-equivalent PWS measurements ~40 m/s faster (Fig. F24). PWS3 velocity fluctuations over 10–40 m show an inverse correlation with wet bulk density. PWS3 measurements on XCB split cores (272–418 mbsf) range from 1520 to 1740 m/s, with a mean gradient of ~1.3 m/s/m. Split-core *P*-wave velocity from 272 to 345 mbsf also appears to be controlled by wet bulk density in the sediment's unloaded shipboard state. Velocities of the increasingly consolidated ooze-chalk sediments from 345 to 408 mbsf increase rapidly from 1540 to 1660 m/s.

Comparison with Site 846 Wireline *P*-Wave Velocity Log

Large differences between wireline log velocities determined in the downhole environment and measurements made in the shipboard laboratory are evident below 120 mbsf (Fig. F24). The difference between the logging and PWS3 velocities from 120 to 255 mbsf reflects the effective stress sensitivity of the unconsolidated skeletal frame of the pelagic ooze sediments. In the interval between 255 and 345 mbsf, the PWS3 and wireline logging velocities are inversely related. PWS3 velocity variability can be explained by variation in the grain density component of bulk density where the sediments are not under consolidation stress. At their in situ consolidation state, sediment *P*-wave transmission velocities are controlled by their sensitivity to the porosity component of bulk density; shipboard and downhole porosity measurements both show a large porosity increase (70%–88%) from 255 to 305 mbsf, followed by a porosity decrease (88%–67%) from 305 to 345 mbsf (Fig. F23) (see "Downhole Measurements" in the "Site 846" chapter of the Leg 138 *Initial Reports* volume) (Shipboard Scientific Party, 1992). From 345 to 375 mbsf, the PWS3 and logging velocities follow an identical velocity gradient (3.33 m/s/m) and then fluctuate (±50 m/s) around a
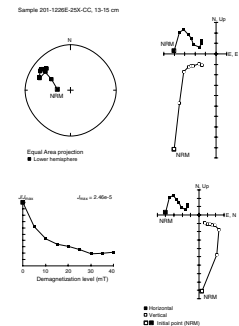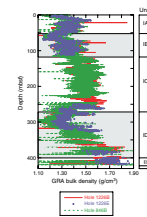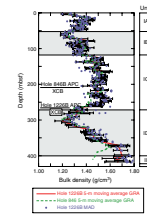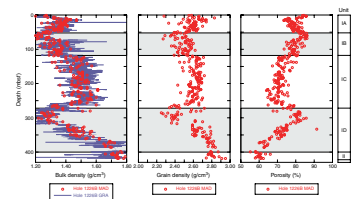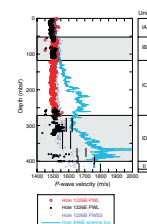
mean value of 1670 m/s for PWS3 data and 1820 m/s for the downhole logging results.

We attempted to determine drilling-related velocity artifacts associated with PWS3 measurements in XCB cores by measuring (1) intact core biscuits with minimal slurry rind at the core margin; (2) Hole 1226E piston cores over 271.9–326 mbsf, which was cored by XCB in Hole 1226B; and (3) plug samples from Hole 1226E split cores from which slurry rind was removed. We used simple ray traveltimes through a slurry rind-core biscuit model, assuming that the slurry rind has a velocity between 1500 and 1530 m/s and using the PWS3 velocities as composite measurements, to estimate the true core sediment velocity for various rind thicknesses. The results are shown as the velocity range between the solid lines for selected depth intervals in Figure F24. From this analysis, drilling disturbance appears to cause a 50- to 100-m/s decrease in recorded PWS3 velocities.

Natural Gamma Ray Emission

Natural gamma radiation was measured on the MST for Holes 1226B (spacing = 30 cm, count time = 15 s) and 1226E (spacing = 15 or 30 cm, count time = 15 s) and by wireline logs. Logging and MST NGR measurements exhibit a strong correlation from ~71 to 320 mbsf (Fig. F25A) (71 mbsf corresponds to the base of the drill pipe above which the logging NGR signal is attenuated). The MST peak at ~53 mbsf corresponds to the top of Subunit IB, which is composed of alternating layers of nannofossil-rich diatom ooze and diatom or nannofossil ooze. This interval has been previously shown to be exceptionally high in organic carbon (Shipboard Scientific Party, 1992) and enriched in uranium (Fig. F25B), reflecting highly reducing conditions at shallow burial depths. An anomalous drop in logging NGR measurements at ~318 mbsf, not reflected in the MST data or uranium concentrations, may be related to a sharp transition from indurated diatom ooze to nannofossil ooze.

Thermal Conductivity

Thermal conductivity measurements were made on Hole 1226B sediments at a rate of one per core (usually the third section, 75 cm, if this was available). Values range between 0.69 and 1.09 W/(m·K) (average = 0.85 W/[m·K]). Average normalized thermal conductivity and bulk density show a high correlation (Fig. F26), indicating that the thermal conductivity is a direct function of water content of the sediments (Bullard, 1963), consistent with Leg 138, Site 846 measurements. Thermal conductivity measurement quality was degraded between 280 and 320 mbsf and 365 and 380 mbsf, due to core disturbance and unfilled core liners.

Formation Factor

Formation factor was determined for Hole 1226B as described in "Formation Factor," p. 47, in "Physical Properties" in the "Explanatory Notes" chapter, with two measurements taken per section for Cores 201-1226B-1H through 6H, one per section for Cores 7H through 35X, and at least one per section for Cores 36X through 47X. Where possible, intact core biscuits were tested to minimize drilling disturbance effects in XCB cores (Cores 201-1226B-30X and below).

F25. NGR and radioactive element profiles, p. 70.
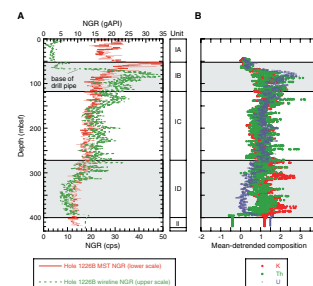
F26. Thermal conductivity measurements, p. 71.
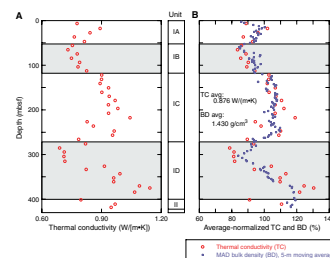
Lithostratigraphy and porosity are clearly reflected in the formation factor profile (Fig. F27). Down to ~270 mbsf (Subunits IA–IC), formation factors fluctuate between 1.8 and 3.0, with transitions at (1) ~50 mbsf (Subunit IA/IB boundary), coincident with a sharp porosity increase; (2) ~119 mbsf (Subunit IB/IC boundary), coincident with a steep porosity decrease; and (3) ~265 mbsf (Subunit IC/ID boundary), coincident with the initial increase in porosity associated with the porosity high between 275 and 320 mbsf. Data quality in the interval from 275 to 300 mbsf is mixed, as drilling-related artifacts bias the resistivity measurements downward. Outlined data points in Figure F27 were measured on core biscuits, with the electrodes inserted into drilled pilot holes for samples below 360 mbsf. The large change in formation factor (from 3 to 4.5) over the 300- to 375-mbsf interval is associated with both a large porosity decrease (from 87% to 55%) and increasing induration of the sediments (see "Lithostratigraphy," p. 7). Electrical conductivity anisotropy ranges from 2% to 14% (average = 7%) in Subunits IA–IC. Anisotropy associated with the highlighted measurements from 300 to 375 mbsf ranges from 4% to 10%.

Summary and Discussion

We can identify five physical property zones at Site 1226, only two of which correspond closely to lithostratigraphic subdivisions (Subunit IA and Unit II; see "Description of Lithostratigraphic Units," p. 8, in "Lithostratigraphy"). Lithostratigraphic Subunits IA, IB, and IC are characterized by an absence of ferrimagnetic minerals. Although the signal is very low in Subunit IB (50–120 mbsf), it seems to be cyclic and may represent a primary depositional record. There is a subtle decline in the magnetic signal at the top of lithostratigraphic Subunit IB, but the boundary is much more strongly recognized in the lower bulk density and higher porosity and NGR, which clearly define the diatom-dominated ooze between 50 and 70 mbsf.

A sharp increase in the density is present at ~120 mbsf, which corresponds to the boundary between lithostratigraphic Subunits IB and IC, but as Figure F22 indicates, this is probably just part of a general downhole increase. Magnetic susceptibility, *P*-wave velocity, and grain density show little variation across this lithostratigraphic boundary, and porosity continues to decline continuously from the top of Subunit IB to the base of Subunit IC. We therefore cannot confidently recognize the Subunit IB/IC boundary using the physical property data.

A number of significant changes in the downhole trends of all physical properties occur across the interval from 264 to 272 mbsf, at or near the base of Subunit IC. Magnetic susceptibility becomes measurably positive at ~264 mbsf and then steps up again at 272 mbsf. The most significant change in density, from ~1.45 to 1.32 g/cm³, takes place at 264 mbsf, coincident with a drop in grain density and *P*-wave velocity and an increase in porosity. Density increases again for a short interval at ~270 mbsf, and magnetic susceptibility increases appreciably at this level. Overall, this interval corresponds to the increase in linear sedimentation rate from ~15 m/m.y. below 264 mbsf to >30 m/m.y. above this level (see "Lithostratigraphy," p. 7).

Across the interval from 264 to 320 mbsf, all physical properties significantly deviate from general downhole consolidation trends and we recognize this as a distinct zone with respect to physical properties. It corresponds to an interval of mainly diatom ooze. Across this interval, bulk densities decline to an average of ~1.30 g/cm³ or less. Porosity and
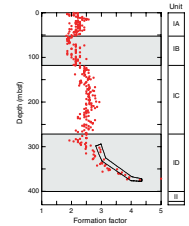
in situ *P*-wave velocity (the latter from Hole 846B; Shipboard Scientific Party, 1992) both reflect the increase in water content of these sediments, similar to the situation we described at Site 1225, Subunit IC (see "Summary and Discussion," p. 29, in "Physical Properties" in the "Site 1225" chapter). Between 300 and 320 mbsf, a subzone characterized by higher magnetic susceptibility is present near the base of the diatom-rich interval.

From ~300 mbsf, bulk density and *P*-wave velocity increase and porosity declines on a downhole consolidation trend to the base of the hole. Average grain density increases from 2.65 to 2.85 g/cm³ down to 400 mbsf and then increases to 2.95 g/cm³ in Unit II. The increase in average grain density over this interval is probably in part a result of an increase in iron-bearing minerals, indicated by the reddish color of Unit II and the increase in magnetic susceptibility from 320 mbsf to the base of the hole, but with a sharp increase at 400 mbsf coincident with the lithostratigraphic boundary.

DOWNHOLE TOOLS

At Site 1226, four different downhole tools were employed: the Adara temperature shoe, the DVTP, the PCS, and the DVTP-P. The results of these deployments are described in the three subsections below.

In Situ Temperature Measurements

Fourteen reliable determinations of downhole temperature were made at depths between 0 and 400 mbsf at Site 1226 using the Adara APC temperature tool and the DVTP. Table T12 summarizes the deployments. As described in "Downhole Tools," p. 49, in the "Explanatory Notes" chapter, in situ temperatures were estimated by extrapolation of the station data using thermal conductivities measured on adjacent cores to correct for the frictional heating on penetration. With the exception of the measurement from 310 mbsf, all of the temperature fits had 95% confidence intervals of <0.01°C.

The estimated in situ temperatures from both the Adara tool and the DVTP define a gradient of 0.0572°C/m in the upper 400 m of the sediment column (Fig. F28A). Extrapolating the temperatures using this temperature gradient yields a value of 25.9°C at the sediment/basement contact. Multiplying the gradient by an average thermal conductivity of 0.85 W/(m·K) (Fig. F26) yields a conductive heat flow estimate of 48.7 mW/m² at Site 1226. This value lies near the center of global heat flow database values for this area (Pollock et al., 1993). The temperature data from Site 1226 define a profile that is much more linear than the curved profile measured at Site 1225. There is a very slight curvature that can be explained by the decrease in thermal conductivity with depth. Figure F28B shows a theoretical steady-state conductive temperature profile calculated using a constant heat flow of 48 mW/m² and the measured thermal conductivities from the Hole 1226B cores. The consistency of the data with the calculated steady-state conductive profile indicates that basement temperatures are stable and advective heat transport by upward flow is negligible.
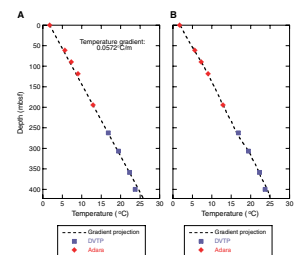
Davis-Villinger Temperature-Pressure Probe

The DVTP-P was deployed twice at Site 1226. During the first run in Hole 1226B, at 241.9 mbsf there was an initial pressure increase of 0.2 MPa during penetration followed by a drop of 12 MPa. Within 2 min pressures abruptly rose again to roughly hydrostatic levels. An average pressure signal equivalent to in situ hydrostatic pressure with ~0.1–0.2 MPa of noise was recorded during the remainder of the 30-min deployment. The abrupt drop in pressure was attributed to a leak near the probe tip. The results of the second deployment in Hole 1226E at 326 mbsf show that the pressure leak was successfully repaired (Fig. F29). The pressure record rose as expected on penetration and then dropped to hydrostatic over the next minute. The pressure then remained constant at hydrostatic level with 0.1- to 0.2-MPa noise for the remainder of the 20-min deployment interval. These data indicate that the seal of the formation around the probe tip was probably not very good and that the tool should be pushed a greater distance into the formation in the future.

Pressure Coring Sampler

Two trial runs of the PCS were made at Site 1226 with extended cutting shoes under rotary drilling. The primary difference between these runs and those at Site 1225 was that targeted intervals were significantly deeper and harder. Core 201-1226B-42P, collected using a Christensen auger with carbide cutters, reached the rig floor at 6208 psi, although the edges of the bit were broken off. After placing this core in an ice bath, the pressure decreased logarithmically to 4907 psi over 150 min (Fig. F30). Approximately 60 mL of gas was released upon opening the tool to atmospheric pressure. Pressure-volume-time relationships during cooling and opening are entirely consistent with the collection of a core with little to no gas (Dickens et al., 2000). Using a Rock Bit International auger with PDC cutters, Core 201-1226E-21P recovered a 1.00-m core but at atmospheric pressure. Examination of the tool revealed that a chert layer was present at the level of the ball valve, which prevented the tool from sealing at depth. There was no damage to the cutting shoe or tool.

APC-Methane Tool

The APC-M tool was deployed in Hole 1226B continuously from Cores 201-1226B-5H through 20H and in Hole 1226E continuously from Cores 201-1226E-5H through 12H. The data recovered from the APC-M tool will be analyzed postcruise.

DOWNHOLE LOGGING

Operations

One logging run was made at Site 1226 in Hole 1226B with the triple combo tool string (see "Downhole Logging," p. 53, in the "Explanatory Notes" chapter). After the last core was recovered at 1900 hr on 22 February, the hole was conditioned for logging. A wiper trip determined that there was no fill at the bottom of the hole. The hole was then displaced with 220 bbl of sepiolite, and the bottom of the drill string was
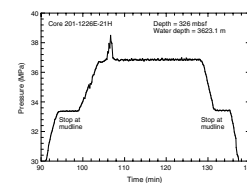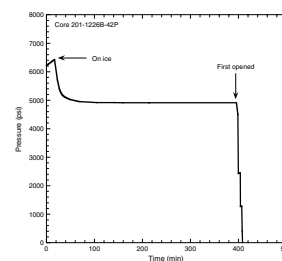
positioned at 80 mbsf. Logging rig-up started at 2300 hr on 22 February. The 35-m-long logging string started downhole 0130 hr on 23 February, and two passes were made without difficulty. Both passes reached the bottom of the hole at the wireline depth of 423 mbsf (3732 mbrf). Logging operations and rig-down were completed by 1030 hr on 23 February (see Table T13 for a complete summary of the operations).

Data Quality

The caliper log (Fig. F31A) shows that the borehole wall was generally smooth and that the caliper arm maintained good contact with the formation over most of the interval, a requirement for good quality data recording. Between 200 and 250 mbsf, the caliper appeared to reach its maximum extent, but the very good agreement between the density and porosity logs with core measurements (shaded circles in Fig. F31E, F31F) show that these measurements, which are the most sensitive to hole quality, were not affected. As at the previous site, the far porosity readings are generally lower than the near porosity because of their greater depth of investigation and they agree well with the MAD data. The excellent agreement between logs and the MAD properties extends to the entire interval logged and allows fine-scale core-log correlation of some distinctive features. A local density and resistivity minimum in the logs at 138.15 mbsf corresponds to a similar density low in Section 201-1226B-16H-1, from a sample that was taken at the bottom of a 30-cm-thick diatom-rich dark green band. Similarly, a density and resistivity peak at 262.64 mbsf can be associated with a density maximum measured at the top of Section 201-1226B-34X-2, underlying a dark green diatom- and nannofossil-bearing carbonate ooze layer. In such favorable hole conditions, similar core-log correlations can be extended further to correlate core description and downhole measurements.

Comparison with Hole 846B Logs

Figure F32 compares the logs from Hole 1226B (solid red lines) with the data recorded in Hole 846B during Leg 138 (dashed green line). The comparison between the two calipers in Figure F32A shows that Hole 846B was slightly narrower, but both holes are of comparable quality, which is confirmed by the excellent match between the two sets of logs. Both density and resistivity logs are almost identical, and the only differences are in the thorium and potassium yields (Fig. F32C, F32E). As at Site 1225, this difference is due to the low natural radioactivity of the nannofossil ooze that constitutes the bulk of the formation and the higher sensitivity of the gamma ray tool used during Leg 201 even though gamma readings were higher in Hole 1226B than Hole 1225A. However, a comparison of gamma ray measurements shows that yields are higher from Hole 1226B (average = >10 gAPI) than those recorded from Hole 1225A (average = <10 gAPI). The higher values measured in Hole 1226B are within the sensitivity range of the two generations of gamma ray sondes used (Hostile Environment Natural Gamma Ray Sonde and Natural Gamma Ray Tool) (see "Downhole Logging," p. 53, in the "Explanatory Notes" chapter), allowing a good match between the total counts of the logs. As in Hole 846B, the almost perfect parallelism between total gamma ray counts and the uranium content (Fig. F31B, F31C) shows that the local radioactivity is dominated by uranium and that uranium content increases steadily uphole. This obser-

vation, made during Leg 138, had suggested that this was the indication of high organic carbon in sufficiently reducing sediments, which would accumulate insoluble uranium(IV) from the seawater (Shipboard Scientific Party, 1992).
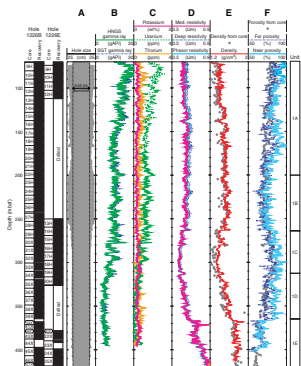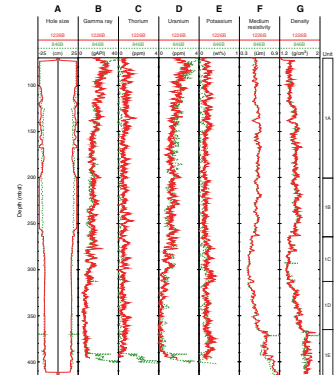
Logging Stratigraphy

As at Site 1225, the sediments at Site 1226 can be generally described by low natural radioactivity and physical attributes (density and resistivity) typical of high porosity. Both porosity logs and MAD measurements show that the porosity is consistently >60% (average = ~70%), explaining the generally low density and resistivity. The low NGR values are typical of the nannofossil-rich sediments dominant at Site 1226, and the main compositional change indicated by the logs is the general increase of uranium uphole. Our characterization of the formation from the logs is based on the physical measurements that show the clearest distinctions, specifically the resistivity and the density. Because of the limited variations in all data, we consider that the sediments penetrated by Hole 1226B correspond to only one logging unit. Subtle covariation differences allow definition of five subunits (Subunits 1A–1E) (see Fig. F31).

Logging Subunit1A (80–200 mbsf) is characterized by generally higher gamma radiation and uranium readings, decreasing steadily with depth. Resistivity and density both increase slightly downhole, and porosity decreases accordingly. The bottom of this subunit is marked by a sharp drop in gamma radiation and uranium, which is marked also in the density and resistivity logs.

Logging Subunit 1B (200–263 mbsf) displays almost uniform values for all logs, except for the decrease in gamma radiation and uranium that follows the general downward trend of the natural radioactivity in the entire hole. This subunit coincides with the only interval in the hole where the caliper indicates a consistently larger hole. Although this does not seem to have affected the data, which compare well with the core measurements and the data from Site 846, it indicates an interval with lower mechanical cohesion than the formations above and below.

In logging Subunit 1C (263–312 mbsf), gamma radiation counts, resistivity, and density decrease steadily with depth while porosity increases. This subunit corresponds to the upper part of lithostratigraphic Subunit ID, described as alternating clay- and radiolarian-bearing diatom nannofossil ooze with clay- and radiolarian-bearing diatom-rich nannofossil ooze, with a generally higher diatom-ooze proportion than the surrounding sediments (see "Description of Lithostratigraphic Units," p. 8, in "Lithostratigraphy"). The sequence of variously clay-bearing intervals is apparent in the generally larger variations in the NGR log. The higher porosity and lower density are typical of diatom-rich sediments.

Logging Subunit 1D (312–363 mbsf) is defined by a steady increase in resistivity and density with depth, whereas porosity decreases and gamma radiation counts are almost uniform. This subunit generally coincides with the middle part of lithostratigraphic Subunit ID, composed of diatom-bearing nannofossil chalk (see "Description of Lithostratigraphic Units," p. 8, in "Lithostratigraphy").

The top of logging Subunit 1E at 272 mbsf is marked by a sharp increase in density and resistivity and an opposite decrease in porosity. This logging subunit coincides with the deeper section of lithostrati-

graphic Subunit ID, described as diatom-bearing nannofossil chalk with chert layers (see **"Description of Lithostratigraphic Units,"** p. 8, in "Lithostratigraphy"). The spikes in the resistivity and density logs throughout this subunit could be associated with these layers.

Temperature Log

Temperatures were recorded with the Lamont-Doherty Earth Observatory Temperature/Acceleration/Pressure (TAP) memory tool attached at the bottom of the triple combo tool string. Because only a few hours had passed since the end of drilling operations and hole conditioning, the borehole temperature is not representative of the actual equilibrium temperature distribution of the formation. In the case of Hole 1226B, the drilling fluids circulating through the water column generated borehole fluid temperatures lower than the formation temperatures. Discrete measurements made with the DVTP-P indicate a maximum formation temperature of 23.7°C at 400 mbsf (see **"In Situ Temperature Measurements,"** p. 33, in "Downhole Tools"), whereas the maximum temperature recorded by the TAP tool is 14.0°C at 421 mbsf (see Fig. **F33**). The absence of significant anomalies in this profile not attributable to operations shows that any hydrologic activity is absent or of low intensity.

F33. Hole 1226B temperature log, p. 78.
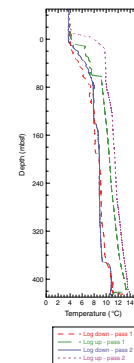
REFERENCES

Athy, L.F., 1930. Density, porosity, and compaction of sedimentary rocks. *AAPG Bull.,* 14:1–24.

Baker, P.A., Stout, P.M., Kastner, M., and Elderfield, H., 1991. Large-scale lateral advection of seawater through oceanic crust in the central equatorial Pacific. *Earth Planet. Sci. Lett.,* 105:522–533.

Berggren, W.A., Hilgen, F.J., Langereis, C.G., Kent, D.V., Obradovich, J.D., Raffi, I., Raymo, M.E., and Shackleton, N.J., 1995a. Late Neogene chronology: new perspectives in high-resolution stratigraphy. *Geol. Soc. Am. Bull.,* 107:1272–1287.

Berggren, W.A., Kent, D.V., Swisher, C.C., III, and Aubry, M.-P., 1995b. A revised Cenozoic geochronology and chronostratigraphy. *In* Berggren, W.A., Kent, D.V., Aubry, M.-P., and Hardenbol, J. (Eds.), *Geochronology, Time Scales and Global Stratigraphic Correlation.* Spec. Publ.—SEPM (Soc. Sediment. Geol.), 54:129–212.

Brady, S., and Gieskes, J.M., 1976. Interstitial water studies, Leg 34. *In* Yeats, R.S., Hart, S.R., et al., *Init. Repts., DSDP,* 34, Washington (U.S. Govt. Printing Office), 625–628.

Bullard, E.C., 1963. The flow of heat through the floor of the ocean. *In* Hill, M.N. (Ed.), *The Sea* (Vol. 3): New York (Wiley), 218–232.

Carmichael, R.S., 1982. *Handbook of Physical Properties of Rocks* (Vol. 2): Boca Raton, FL (CRC Press).

Chavez, F.P., and Barber, R.T., 1987. An estimate of new production in the equatorial Pacific. *Deep-Sea Res. Part A,* 34:1229–1243.

Dickens, G.R., Wallace, P.J., Paull, C.K., and Borowski, W.S., 2000. Detection of methane gas hydrate in the pressure core sampler (PCS): volume-pressure-time relations during controlled degassing experiments. *In* Paull, C.K., Matsumoto, R., Wallace, P.J., and Dillon, W.P. (Eds.), *Proc. ODP, Sci. Results,* 164: College Station, TX (Ocean Drilling Program), 113–126.

Emeis, K.-C., Doose, H., Mix, A., and Schulz-Bull, D., 1995. Alkenone sea-surface temperatures and carbon burial at Site 846 (eastern equatorial Pacific Ocean): the last 1.3 m.y. *In* Pisias, N.G., Mayer, L.A., Janecek, T.R., Palmer-Julson, A., and van Andel, T.H. (Eds.), *Proc. ODP, Sci. Results,* 138: College Station, TX (Ocean Drilling Program), 605–613.

Farrell, J.W., Raffi, I., Janecek, T.C., Murray, D.W., Levitan, M., Dadey, K.A., Emeis, K.-C., Lyle, M., Flores, J.-A., and Hovan, S., 1995. Late Neogene sedimentation patterns in the eastern equatorial Pacific. *In* Pisias, N.G., Mayer, L.A., Janecek, T.R., Palmer-Julson, A., and van Andel, T.H. (Eds.), *Proc. ODP, Sci. Results,* 138: College Station, TX (Ocean Drilling Program), 717–756.

Hoehler, T.M., Alperin, M.J., Albert, D.B., and Martens, C.S., 1998. Thermodynamic control on hydrogen concentrations in anoxic sediments. *Geochim. Cosmochim. Acta,* 62:1745–1756.

————, 2001. Apparent minimum free energy requirements for methanogenic Archaea and sulfate-reducing bacteria in an anoxic marine sediment. *FEMS Microbio. Ecol.,* 38:33–41.

Mayer, L., Pisias, N., Janecek, T., et al., 1992. *Proc. ODP, Init. Repts.,* 138 (Pt. 1): College Station, TX (Ocean Drilling Program).

McDuff, R.E., 1985. The chemistry of interstitial waters, Deep Sea Drilling Project Leg 86. *In* Heath, G.R., Burckle, L.H., et al., *Init. Repts. DSDP,* 86: Washington (U.S. Govt. Printing Office), 675–687.

Oremland, R.S., Marsh, L.M., and Polcin, S., 1982. Methane production and simultaneous sulfate reduction in anoxic salt marsh sediments. *Nature,* 296:143–145.

Oremland, R.S., and Polcin, S., 1982. Methanogenesis and sulfate reduction: competitive and noncompetitive substrates in estuarine sediments. *Appl. Environ. Microbiol.,* 44:1270–1276.

Parkes, R.J., Cragg, B.A., Bale, S.J., Getliff, J.M., Goodman, K., Rochelle, P.A., Fry, J.C., Weightman, A.J., and Harvey, S.M., 1994. A deep bacterial biosphere in Pacific Ocean sediments. *Nature,* 371:410–413.

Pisias, N.G., Mayer, L.A., Janecek, T.R., Palmer-Julson, A., and van Andel, T.H. (Eds.), 1995. *Proc. ODP, Sci Results,* 138: College Station, TX (Ocean Drilling Program).

Pisias, N.G., Mayer, L.A., and Mix, A.C., 1995. Paleoceanography of the eastern equatorial Pacific during the Neogene: synthesis of Leg 138 drilling results. *In* Pisias, N.G., Mayer, L.A., Janecek, T.R., Palmer-Julson, A., and van Andel, T.H. (Eds.), *Proc. ODP, Sci. Results,* 138: College Station, TX (Ocean Drilling Program), 5–21.

Pollack, H.N., Hurter, S.J., and Johnson, J.R., 1993. Heat flow from the Earth's interior: analysis of the global data set. *Rev. Geophys.,* 31:267–280.

Schink, B., 1997. Energetics of syntrophic cooperation in methanogenic degradation. *Microbiol. Mol. Biol. Rev.,* 61:262–280.

Shipboard Scientific Party, 1992. Site 846. *In* Mayer, L., Pisias, N., Janecek, T., et al., *Proc. ODP, Init. Repts.,* 138 (Pt. 1): College Station, TX (Ocean Drilling Program), 265–333.

Smith, D.C., Spivack, A.J., Fisk, M.R., Haveman, S.A., Staudigel, H., and ODP Leg 185 Shipboard Scientific Party, 2000. Methods for quantifying potential microbial contamination during deep ocean coring. *ODP Tech. Note,* 28 [Online]. Available from the World Wide Web: <http://www-odp.tamu.edu/publications/tnotes/tn28/INDEX.HTM>. [2002-03-30]

Thauer, R.K., Jungermann, K., and Decker, K., 1977. Energy conservation in chemotrophic anaerobic bacteria. *Bacteriol. Rev.,* 41:100–180.

Wellsbury, P., Goodman, K., Barth, T., Cragg, B.A., Barnes, S.P., and Parkes, R.J., 1997. Deep marine biosphere fueled by increasing organic matter availability during burial and heating. *Nature,* 388:573–576.

Wellsbury, P., and Parkes, R.J., 1995. Acetate bioavailability and turnover in an estuarine sediment. *FEMS Microbiol. Ecol.,* 17:85–94.

Winfrey, M.R., and Ward, D.M., 1983. Substrates for sulfate reduction and methane production in intertidal sediments. *Appl. Environ. Microbiol.,* 45:193–199.

Figure F1. Lithostratigraphic summary at Site 1226. The depth intervals where chert layers are present are indicated. TD = total depth.
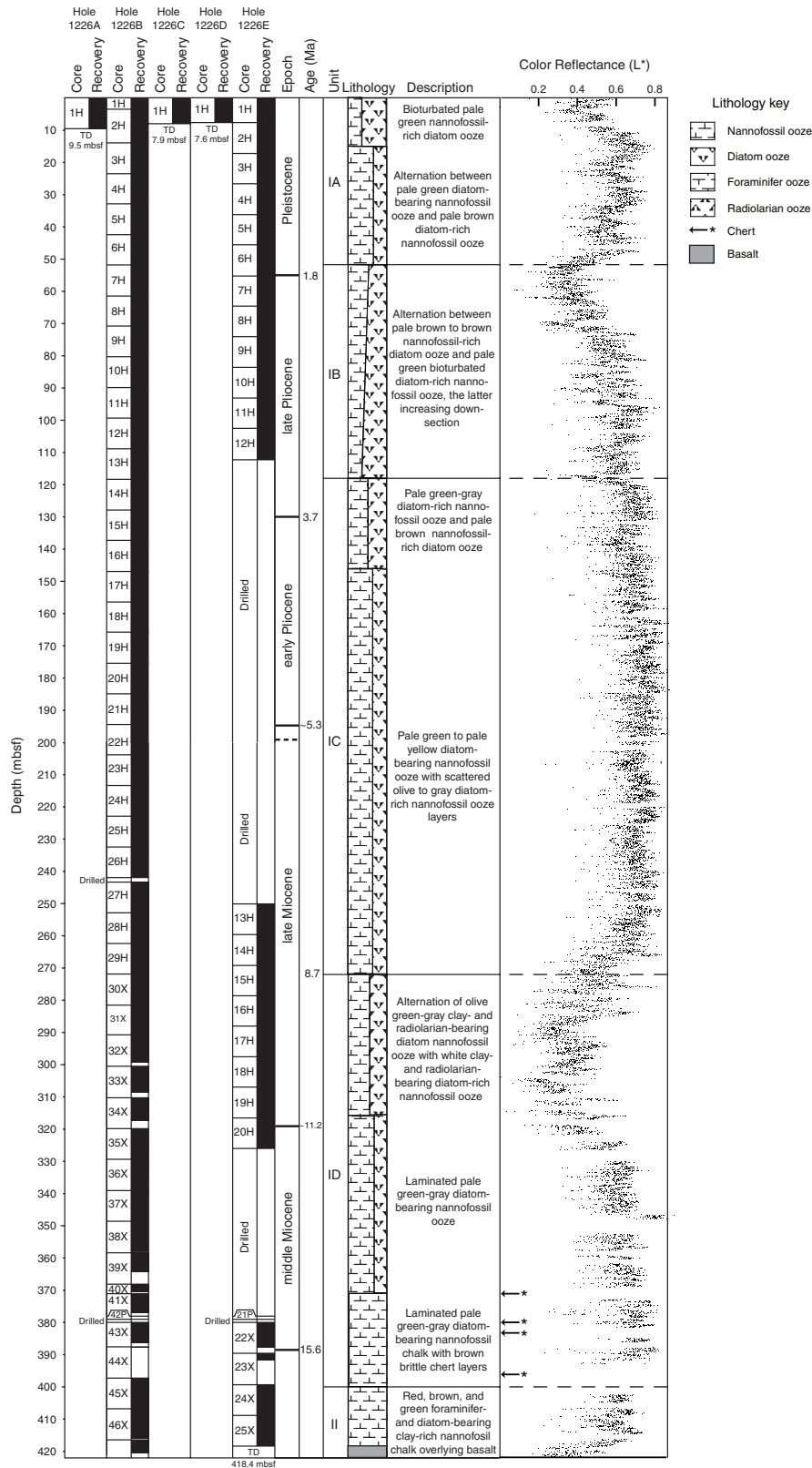
Figure F2. Close-up photographs of core features. **A, B.** Trace fossils in Subunit IA, (A) *Zoophycos* and (B) *Skolithos*. (Continued on next three pages.)
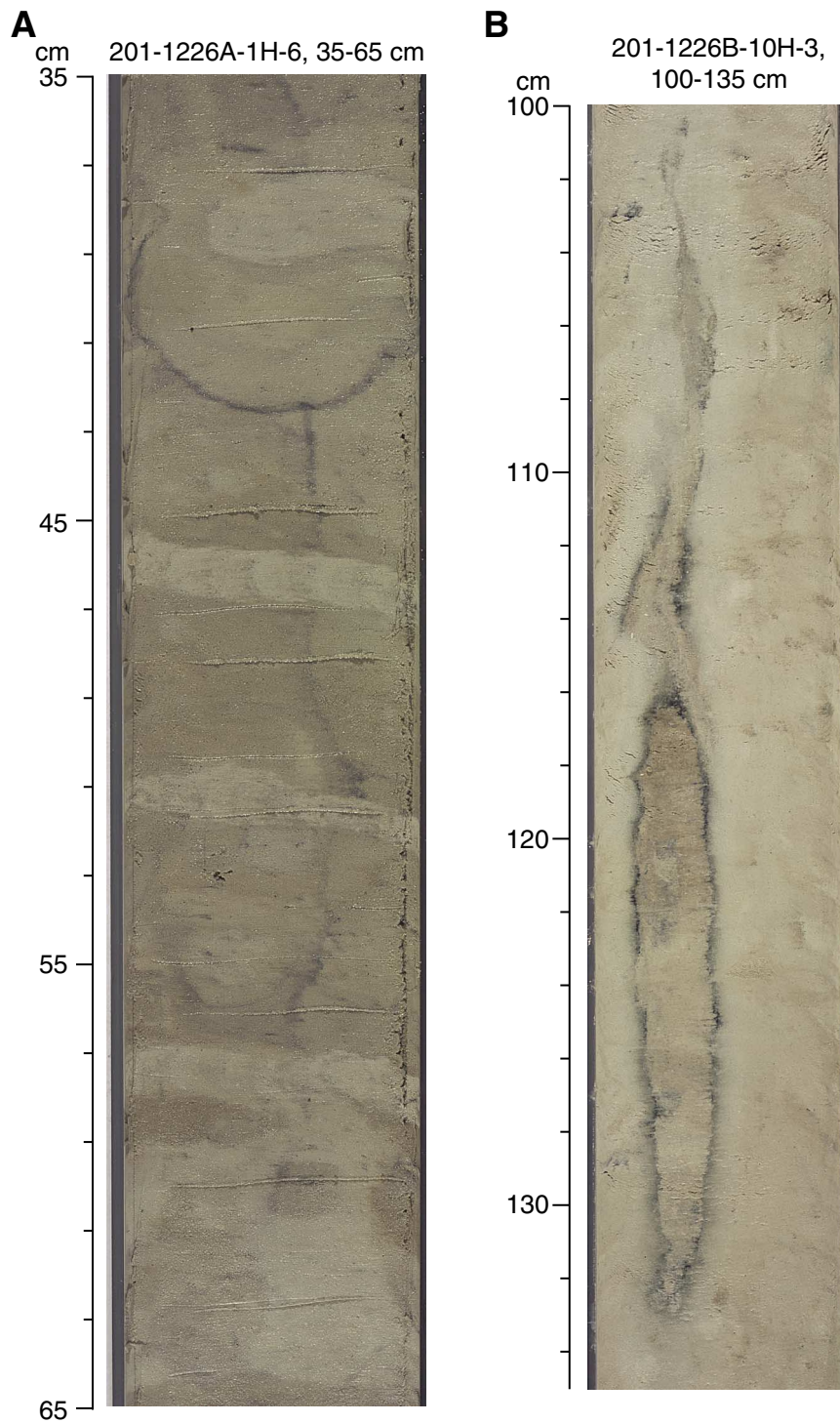
Figure F2 (continued). C. Brown chert layer in Subunit ID. **D.** Yellow dolomite nodule in Subunit ID. (Continued on next page.)

C
cm   201-1226E-22X-5,135-142 cm

D
cm   201-1226E-19H-6, 0-20 cm
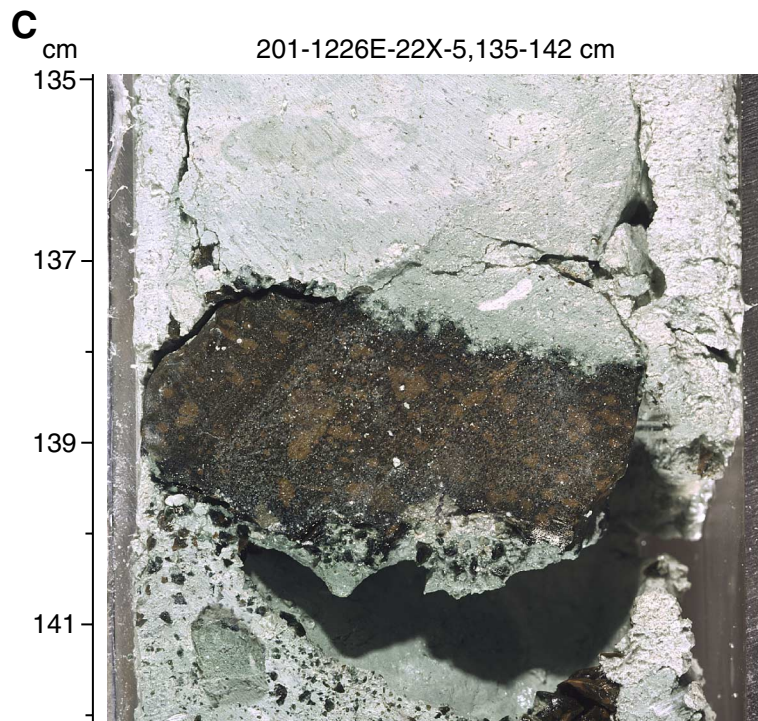
Figure F2 (continued). E, F. Resedimented interval in Unit II. (Continued on next page).
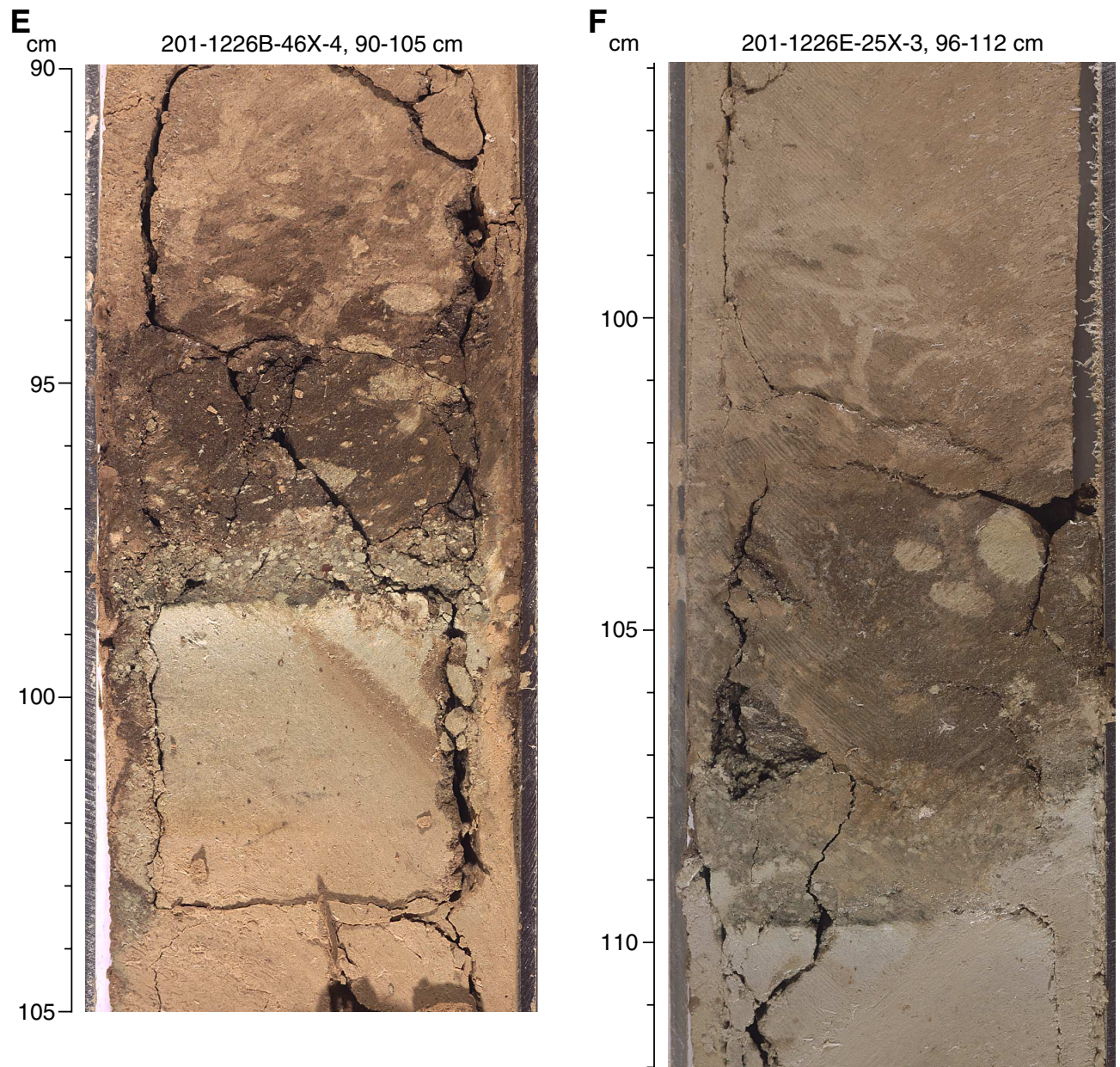
Figure F2 (continued). G. Red hematite-rich sediment directly above basaltic breccia.

G

201-1226B-47X-CC, 27–47 cm
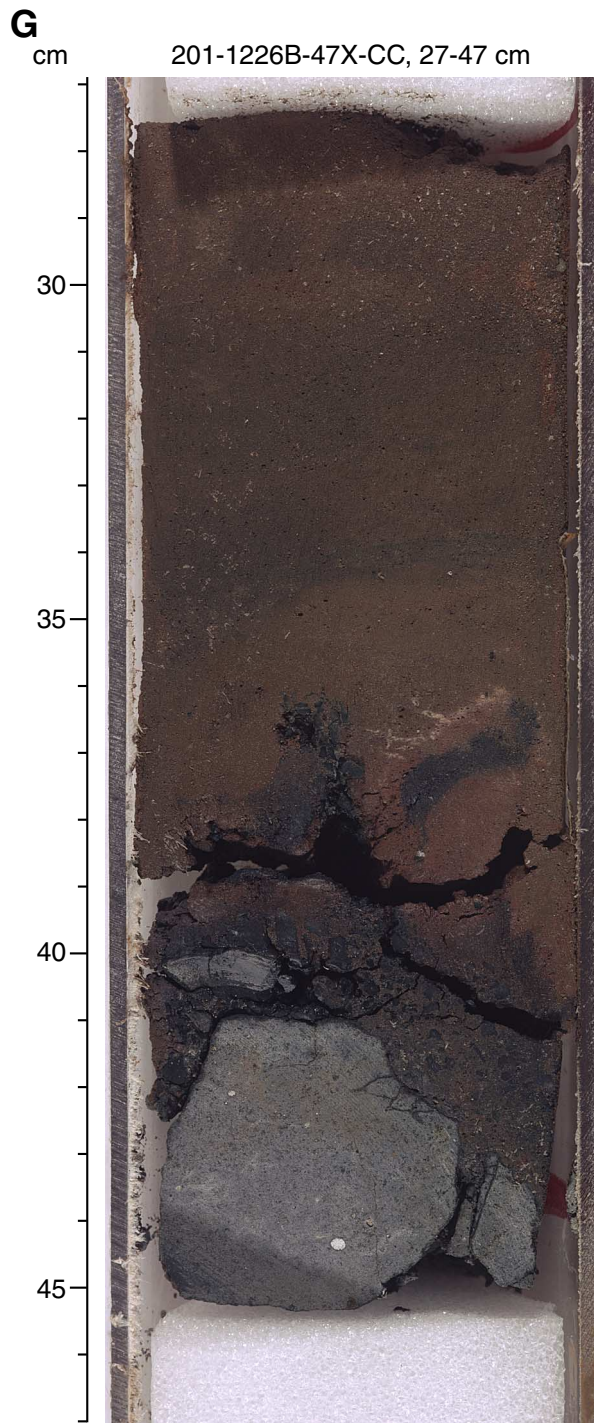
Figure F3. Examples of XRD analyses for Site 1226. Samples from (**A**) a diatom-rich nannofossil ooze layer, (**B**) a nannofossil-rich diatom ooze layer, (**C**) a yellow dolomite nodule, (**D**) a dark speck in diatom nannofossil ooze, (**E**) a brown chert layer, and (**F**) a green porcelanite layer. A = opal-A, C = calcite, B = barite, P = pyrite, D = dolomite, Q = quartz, T = trydimite, Cr = crystobalite, V = vermiculite, K = kaolinite, He = hematite.
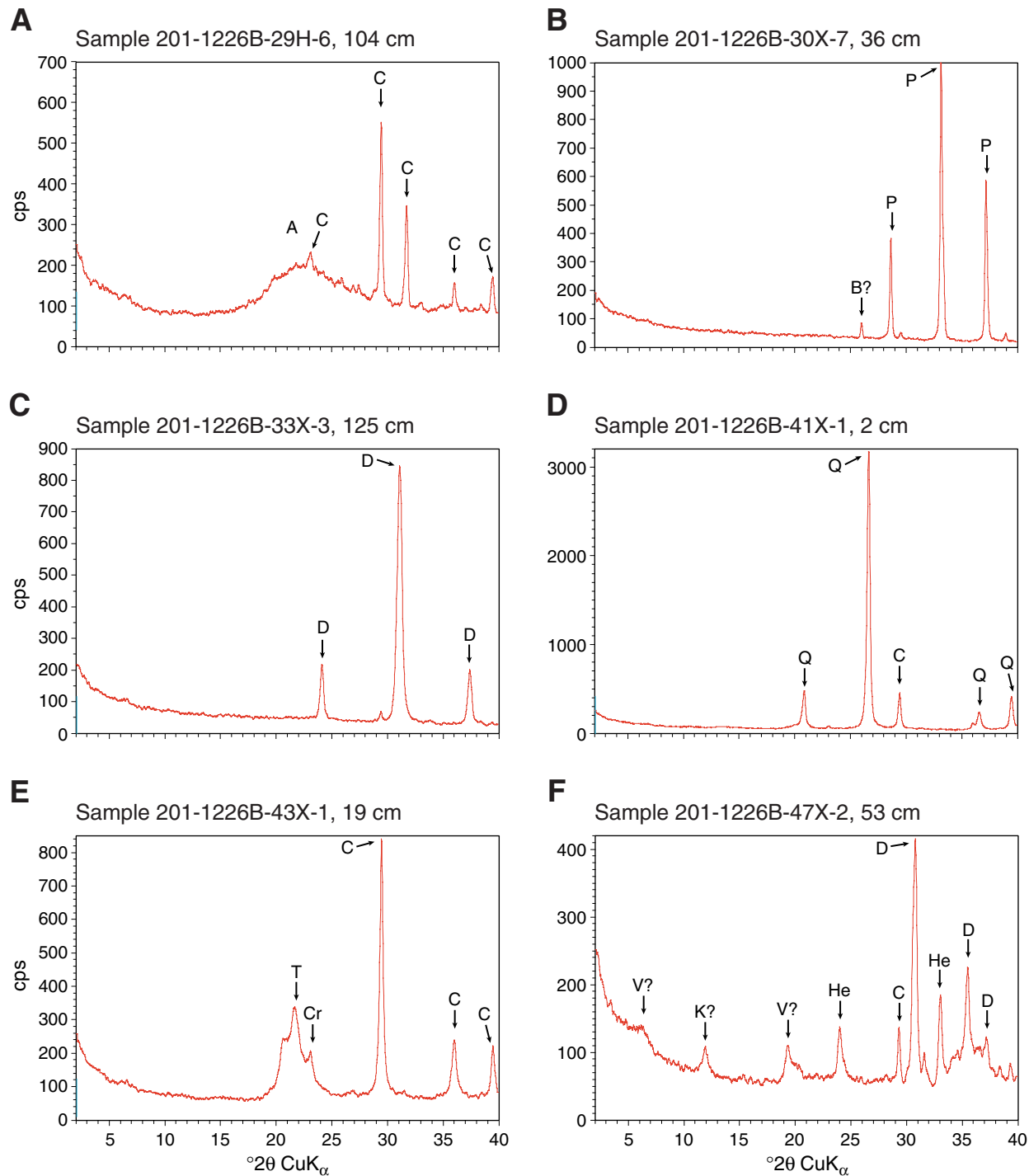
Figure F4. Concentrations of various dissolved species in interstitial waters from Holes 1226B and 1226E. (**A**) Alkalinity, (**B**) dissolved inorganic carbon (DIC), (**C**) nitrite, (**D**) manganese, (**E**) iron, (**F**) sulfate, and (**G**) strontium. (Continued on next two pages.)

Figure F4 (continued). (**H**) lithium, (**I**) calcium, (**J**) sulfide, (**K**) methane, (**L**) ammonium, (**M**) acetate, and (**N**) formate. (Continued on next page.)

Figure F4 (continued). (O) hydrogen, (P) phosphate, (Q) silica, and (R) chloride.

Figure F5. Graphical representation of subsampling and analysis program for the MBIO core sections from Hole 1226B. The sequence of subsections runs from the top of the core (right) to the bottom (left). DNA = deoxyribonucleic acid, ATP = adenosine triphosphate. WRC = whole-round core. 1* = mixed samples from Sections 201-1225B-34X-3 and 33X-4. See Table T2, p. 82, in the "Explanatory Notes" chapter for explanation of sample codes.

Hole 1226B	FISHWR	FISHH	FISHTS	H3S	ABTP	O18B	ABTP	PO4B	SRRF	H2S	CNSS	CHNSF	DIFFF	SLUR (60-mL+2x5-mL syr)	SLUR (60-mL+3x5-mL syr)	HTEW	CELLS	FESF	BIOMHIN	BIOHORS	AMO	DNAF	DNAM	DNAI	DNAT	DNAN	DNAS	DNAODP	ATPS	Sediment Depth (mbsf)
	N₂-flushed cutting rig												ODP cutter																	Top of Section
Interval (cm)		6			6		6			6			5	7	7	6	5	5	10	5	5	5	5	5	5	5	5	5	10	
Sample Type	Rem. WRC	1 Syr	2 Syr	4 Syr	4 Syr	1 Syr	8 Syr	1-cm slice	4 Sy	4 Syr	Plug from 1-m slice	Res. from 1-cm slice	WRC	60-mL+2x5-mL syr	60-mL+3x5-mL syr	3 Syr	WRC	WRC	WRC	WRC	WRC	WRC	WRC	WRC	WRC	WRC	WRC	WRC	WRC	
Package Type	Poly-bag	Anaer. Jar	Poly-bag	Al-bag	Anaer. Jar	Poly-bag	Anaer. Jar	Poly-bag	Al-bag	Poly-bag	Poly-bag	Al-bag	Al-bag	Al-bag	Al-bag	Anaer. Jar	Poly-bag	Al-bag	Poly-bag	Poly-bag	Al-bag	Poly-bag	Poly-bag	Poly-bag	Poly-bag	Poly-bag	Poly-bag	Poly-bag	Poly-bag	
Gas phase in Package		N₂		N₂	N₂		N₂		N₂	N₂		Vac pack	Vac pack	N₂	N₂	N₂		Vac pack			N₂									
Storage Temperature	-80°	+4°C	+4°C	+4°C Radvan	+4°C Radvan	+4°C	+4°C Radvan	-20°C	+4°C Radvan	+4°C	+4°C	+4°C	+4°C'	on ice	on ice	+4°C	-80°C	-20°C	-80°C	-20°C	+4°C	-80°C	-80°C	-80°C	-80°C	-80°C	-80°C	-80°C	-80°C	Sediment Depth (mbsf)
Core / Section																														top
2H 3	1	1	1	1	1	1	1	1	1	1	1	1	1	1	1	1	-	1	1		-	1	1	1	1	1	1	1	1	7.4
3H 3	-	-	-	-	-	-	-	-	1	-	1	1	-				-	1	-		-	1	-	-	1	-	-	-	-	16.9
4H 3	1	1	1	1	1	1	1	1	1	1	1	1	-	-	-	-	-	1	1		-	1	1	1	1	1	1	1	1	26.4
5H 3	-	-	-	-	-	-	-	-	1	-	1	1	-	-	-	-	-	1	-		-	1	-	-	1	-	-	-	-	35.9
6H 3	1	1	1	1	1	1	1	1	1	1	1	1	-	-	-	-	-	1	1	1	1 (1)	1	-	1	1	1	1	1	1	45.4
7H 3	-	-	-	-	-	-	-	-	1	-	1	1	-	-	-	-	-	1	-		-	1	-	-	1	-	-	-	-	54.9
8H 3	1	1	1	1	1	1	1	1	1	1	1	1	-	-	-	-	-	1	1		-	1	1	1	1	1	1	1	1	64.4
9H 3	-	-	-	-	-	-	-	-	1	-	1	1	-	-	-	-	-	1	-		-	1	-	-	1	-	-	-	-	73.9
10H 3	1	1	1	1	1	1	1	1	1	1	1	1	-	-	-	-	-	1	1		1 (1)	-	1	1	1	1	1	1	1	83.4
11H 3	-	-	-	-	-	-	-	-	1	-	1	1	-	-	-	-	-	1	-		-	1	-	-	1	-	-	-	-	92.9
12H 3	1	1	1	1	1	1	1	1	1	1	1	1	-	1	1	1	-	1	1	1	-	1	1	1	1	1	1	1	1	102.4
13H 3	-	-	-	-	-	-	-	-	1	-	1	1	-	-	-	-	-	1	-		-	1	-	-	1	-	-	-	-	111.9
14H 3	-	-	-	-	-	-	-	-	1	-	1	1	-	-	-	-	-	1	-		1 (1)	-	1	-	-	1	-	-	-	121.4
15H 3	1	1	1	1	1	1	1	1	1	1	1	1	-	-	-	-	-	1	1		-	1	1	1	1	1	1	1	1	130.9
16H 3	-	-	-	-	-	-	-	-	1	-	1	1	-	-	-	-	-	1	-		-	1	-	-	1	-	-	-	-	140.4
17H 3	-	-	-	-	-	-	-	-	1	-	1	1	-	-	-	-	-	1	-		-	1	-	-	1	-	-	-	-	149.9
18H 3	1	1	1	1	1	1	1	1	1	1	1	1	1	-	-	-	1	1	1		1	1	1	1	1	1	1	1	1	159.4
19H 3	-	-	-	-	-	-	-	-	1	-	1	1	-	-	-	-	-	1	-		-	1	-	-	1	-	-	-	-	168.9
20H 3	-	-	-	-	-	-	-	-	1	-	1	1	-	-	-	-	-	1	-		-	1	-	-	1	-	-	-	-	178.4
21H 3	-	-	-	-	-	-	-	-	1	-	1	1	-	-	-	-	-	1	-		-	1	-	-	1	-	-	-	-	187.9
22H 3	1	1	1	1	1	1	1	1	1	1	1	1	-	1	1	1	-	1	1	1	1	-	1	1	1	1	1	1	1	196.2
23H 3	-	-	-	-	-	-	-	-	1	-	1	1	-	-	-	-	-	1	-		-	-	-	1	-	-	-	-	-	206.9
24H 3	1	1	1	1	1	1	1	1	1	1	1	1	-	-	-	-	-	1	-		-	1	1	1	1	1	1	1	1	216.4
25H 3	-	-	-	-	-	-	-	-	1	-	1	1	-	-	-	-	-	1	-		-	-	-	1	-	-	-	-	-	225.9
26H 3	-	-	-	-	-	-	-	-	1	-	1	1	-	-	-	-	-	1	-		-	-	-	1	-	-	-	-	-	235.9
27H 3	1	1	1	1	1	1	1	1	1	1	1	1	-	-	-	-	-	1	1		1	1	1	1	1	1	1	1	1	246.4
28H 3	-	-	-	-	-	-	-	-	1	-	1	1	-	-	-	-	-	1	-	1	-	1	-	-	1	-	-	-	-	255.9
29H 3	-	-	-	-	-	-	-	-	1	-	1	1	-	-	-	-	-	1	-		-	-	-	1	-	-	-	-	-	265.4
30X 3	1	1	1	1	1	1	1	1	1	1	1	1	-	-	-	-	-	1	1		-	1	1	1	1	1	1	1	1	274.9
31X 3	-	-	-	-	-	-	-	-	1	-	1	1	-	-	-	-	-	1	-		-	-	-	1	-	-	-	-	-	284.5
32X 3	-	-	-	-	-	-	-	-	1	-	1	1	-	-	-	-	-	1	-		-	-	-	1	-	-	-	-	-	293.8
33X 4	1	1	1	-	-	-	-	-	-	-	-	-	-	-	-	-	-	1*	1*		1*	-	1*	1*	1*	1*	1*	1*	1*	305.0
34X 3	-	-	-	-	-	-	-	-	-	-	-	-	-	1	1	-	-	1	-		-	-	-	-	-	-	-	-	-	313.2
35X 3+4	-	-	-	-	-	-	-	-	1	1	1	1	-	-	-	-	-	1	-		-	-	-	-	-	-	-	-	-	322.8
36X 3	-	-	-	-	-	-	-	-	-	-	-	-	-	-	-	-	-	-	-		-	-	-	-	-	-	-	-	-	332.4
37X 3	-	-	-	-	-	-	-	-	-	-	-	-	-	-	-	-	-	-	-		-	-	-	-	-	-	-	-	-	342.0
38X 3	-	-	-	-	-	-	-	-	-	-	-	-	-	-	-	-	-	-	-		-	-	-	-	-	-	-	-	-	351.7
39X 3	-	-	-	-	-	-	-	-	-	-	-	-	-	-	-	-	-	-	-		-	-	-	-	-	-	-	-	-	361.3
40X 3	-	-	-	-	-	-	-	-	-	-	-	-	-	-	-	-	-	-	-		-	-	-	-	-	-	-	-	-	370.2
41X 3	-	-	-	-	-	-	-	-	-	-	-	-	-	-	-	-	-	-	-		-	-	-	-	-	-	-	-	-	374.1
42P 2	-	-	-	-	-	-	-	-	-	-	-	-	-	-	-	-	-	-	-		-	-	-	-	-	-	-	-	-	379.5
43X 3	-	-	-	-	-	-	-	-	-	-	-	-	-	1	1	-	-	-	1		-	1	-	1	1	1	1	1	1	382.9
44X 1	-	-	-	-	-	-	-	-	-	-	-	-	-	-	-	-	-	-	-		-	-	-	-	-	-	-	-	-	387.6
45X 3	1	1	1	1	1	1	1	1	1	1	1	1	-	-	-	-	1	1(2,3)	1		-	1	1	1	1	1	1	1	1	400.2
46X 3	1	1	1	1	1	1	1	1	1	1	1	1	-	-	-	-	-	1	1		-	1	1	1	1	1	1	1	1	409.8
47X 2	1	1	1	1	1	1	1	1	1	1	1	1	-	1	1	-	-	1	1		-	-	1	1	1	1	1	1	1	417.9
47X 3, CC	-	-	1(CC)	-	-	-	-	-	-	-	-	-	-	-	-	1	-	1	1		-	-	1	1	1	1	-	-	-	419.4
TOTAL	14	14	14	13	-	13	13	13	33	14	33	33	2	4	5	4	2	32	14	5	3	7	6	33	14	14	14	14	14	

Figure F6. Graphical representation of subsampling and analysis program for the MBIO core sections from Hole 1226E. The sequence of subsectioning runs from the top of the core (right) to the bottom (left). DNA = deoxyribonucleic acid, ATP = adenosine triphosphate. WRC = whole-round core. See Table T2, p. 82, in the "Explanatory Notes" chapter for explanation of sample codes.

Column descriptions (N₂-flushed cutting rig, then ODP cutter):

Curators Code	Analysis	Interval (cm)	Sample Type	Package Type	Gas phase in Package	Temperature Destination
FISHWR	Fluorescent in situ hybridization (FISH)	6	Rem. WRC	Poly-bag		-80°
FISHH	Fluorescent in situ hybridization (FISH)	6	1 Syr	Anaer. Jar	N₂	+4°C
FISHTS	Fluorescent in situ hybridization (FISH)	6	2 Syr	Poly-bag		+4°C
H3S	Activity measurements: methanogenesis, thymidine incorporation, tritiated hydrogen turnover, ¹⁸O phosphate turnover	6	4 Syr	Al-bag	N₂	+4°C Radvan
ABTP	Activity measurements	6	4 Syr	Anaer. Jar	N₂	+4°C Radvan
O18B	Activity measurements	6	1 Syr	Poly-bag		+4°C
ABTP	Activity measurements	6	8 Syr	Anaer. Jar	N₂	+4°C Radvan
PO4B	Activity measurements	6	1-cm slice	Poly-bag		-20°C
SRRF	Sulfate reduction activity; hydrogen concentration; CNHS geochemistry; magnetic bacterial particles	6	4 Syr	Al-Bag	N₂	+4°C Radvan
H2S	Sulfate reduction activity	6	4 Syr	Poly-bag	N₂	+4°C
CNSS	Sulfate reduction activity	6	Plug from 1-m slice	Poly-bag		+4°C
CHNSF	Sulfate reduction activity	6	Res. From 1-cm slice	Al-bag	Vac pack	+4°C
DIFFF	Diffusion experiments	5	WRC	Al-bag	Vac pack	+4°C'
SLUR	General enrichment slurry	7	60-mL + 2 x 5 mL syr	Al-bag	N₂	on ice
SLUR	General enrichment slurry	7	60-mL + 3 x 5-mL syr	Al-bag	N₂	on ice
HTEW	Enrichments for thermophiles	6	3 Syr	Anaer. Jar	N₂	+4°C
CELLS	Cell separations	5	WRC	Poly-bag		-80°C
FESF	Fe/Mn/S solid-phase concentrations and stable isotopes	5	WRC	Al-bag	Vac pack	-20°C
BIOMHIN	Biomarkers	10	WRC	Poly-bag		-80°C
BIOHORS	Biomarkers	5	WRC	Poly-bag		-20°C
AMO	Anaerobic methane oxidation	5	WRC	Al-bag	N₂	+4°C
DNAF	DNA	5	WRC	Poly-bag		-80°C
DNAM	DNA	5	WRC	Poly-bag		-80°C
DNAI	DNA	5	WRC	Poly-bag		-80°C
DNAT	DNA	5	WRC	Poly-bag		-80°C
DNAN	DNA	5	WRC	Poly-bag		-80°C
DNAS	DNA	5	WRC	Poly-bag		-80°C
DNAODP	DNA-ODP archive	5	WRC	Poly-bag		-80°C
ATPS	ATP-DNA	10	WRC	Poly-bag		-80°C

Sampling matrix (1 = sampled, - = not sampled):

Core	Section	FISHWR	FISHH	FISHTS	H3S	ABTP	O18B	ABTP	PO4B	SRRF	H2S	CNSS	CHNSF	DIFFF	SLUR	SLUR	HTEW	CELLS	FESF	BIOMHIN	BIOHORS	AMO	DNAF	DNAM	DNAI	DNAT	DNAN	DNAS	DNAODP	ATPS	Sediment Depth (mbsf)
1H	1	1	1	1	1	1	1	1	1	1	1	1	1	-	1	1	1	-	1	1	-	-	1	1	1	1	1	1	1	1	top
1H	3	1	1	1	-	1	1	1	1	1	-	1	1	1	-	-	-	1	1	1	-	1	1	1	1	1	1	1	1	-	3.0
1H	5	1	1	1	-	-	-	-	-	1	-	1	1	-	-	-	-	-	1	1	-	1	1	1	1	1	1	1	1	-	6.0
14H	3	-	-	-	-	-	-	-	-	1	-	-	-	-	-	-	-	-	1	1	-	-	-	-	1	-	-	-	-	-	262.5
15H	3	-	-	-	-	-	-	-	-	1	1	1	1	-	-	-	-	-	1	1	-	-	-	-	1	-	-	-	-	-	272.0
16H	3	1	1	1	1	1	1	1	1	1	1	1	1	-	-	-	-	-	1	1	-	1	-	1	1	1	1	1	1	1	281.5
17H	3	-	-	-	-	-	-	-	-	1	1	1	1	-	-	-	-	-	1	1	-	-	-	-	1	-	-	-	-	-	291.0
18H	3	1	1	1	1	1	1	1	1	1	1	1	1	1	-	-	1	-	1	1	-	1	1	1	1	1	1	1	1	1	300.5
19H	3	-	-	-	-	-	-	-	-	1	1	1	1	-	-	-	-	-	1	1	-	-	-	-	1	-	-	-	-	-	310.0
20H	3	1	1	1	1	1	1	1	1	1	1	1	1	-	-	-	-	-	1	1	-	1	1	1	1	1	1	1	1	1	319.5
TOTAL		6	6	6	4	5	5	5	5	10	7	9	9	2	1	1	2	1	10	10	0	2	6	5	10	6	6	6	6	4	

Figure F7. Total prokaryotic cell numbers per cubic centimeter (solid circles) and the percentage of cells indicating cell division (open circles) with depth at Site 1226. Vertical dashed line represents the detection limit at 5.6×10^4 cells/cm³. Dividing cell percentages become increasingly unreliable as total cell counts decrease below 10^6 cells/cm³ as within-sample variability rises due to the low number of cells counted. Samples with cell concentrations below the detection limit are arbitrarily shown as containing 1×10^4 cells/cm³.
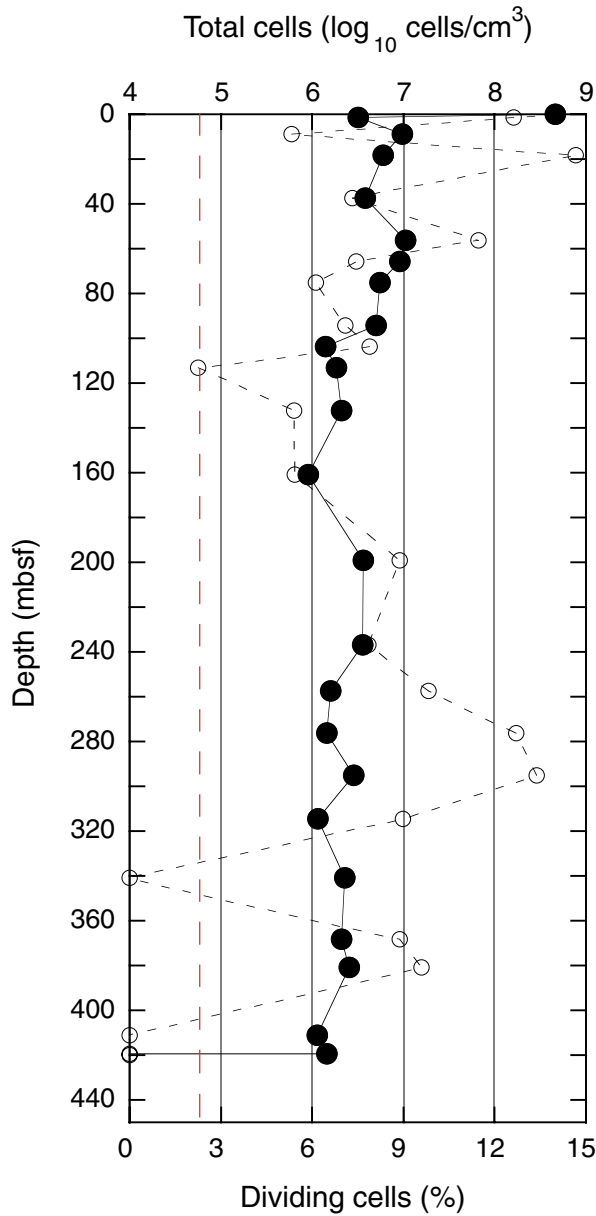
Figure F8. Profile of total prokaryotic cells in Holes 1226E (upper two data points) and 1226B (rest of data points). The heavy dashed line is a model regression line derived from previous ODP legs and updated from Parkes et al., 1994 ($\log_{10}$ cells = 8.03 – 0.66 $\log_{10}$ depth), lighter dashed lines represent the ±2-σ envelope cell concentrations at previously censused ODP sites.
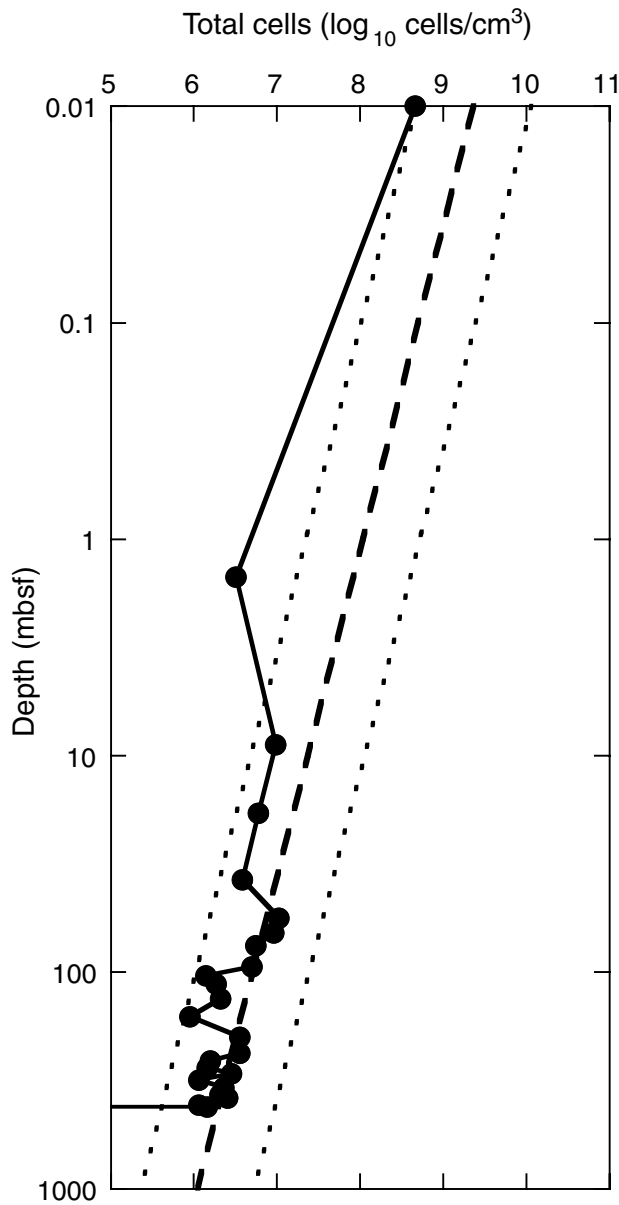
Figure F9. Hard piece of intact sediment (~5-cm-wide "biscuit") found in Core 201-1226B-43X.
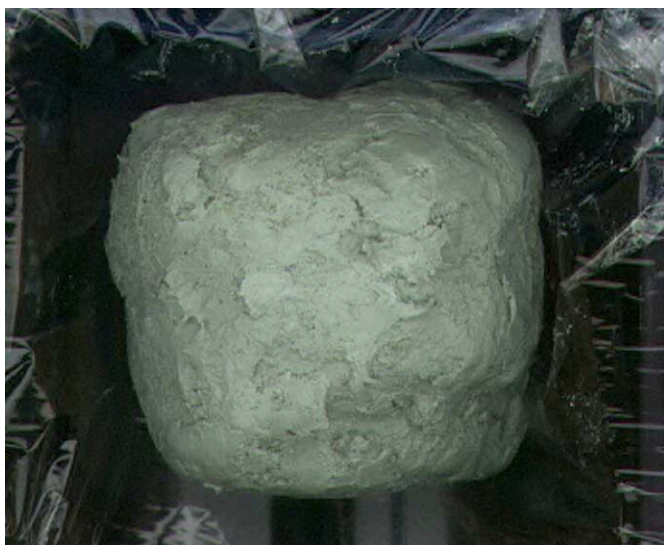
Figure F10. Piece of basalt from the bottom core of Hole 1226B trapped in the core catcher of an XCB core (Section 201-1226B-47X-CC). The rock was washed and surface-sterilized with 3-M HCl, crushed, and used for microbiology and other analyses.

Figure F11. A. Different lines used to create core liner profile for Core 201-1226B-13H. Lines are numbered 1–8 from left. The 5-cm mark (white circle) is visible on the scale to the left (see in "Physical Properties" in the "Explanatory Notes" chapter). (Continued on next page.)

A
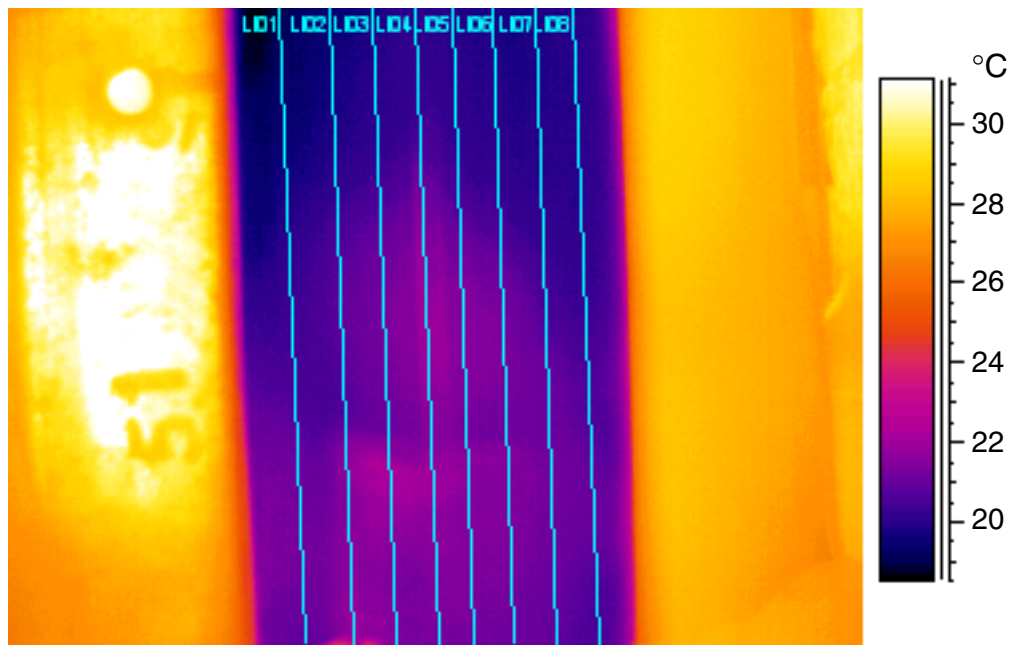
Figure F11 (continued). B. Different core liner temperature profiles generated along the eight profile lines.

B
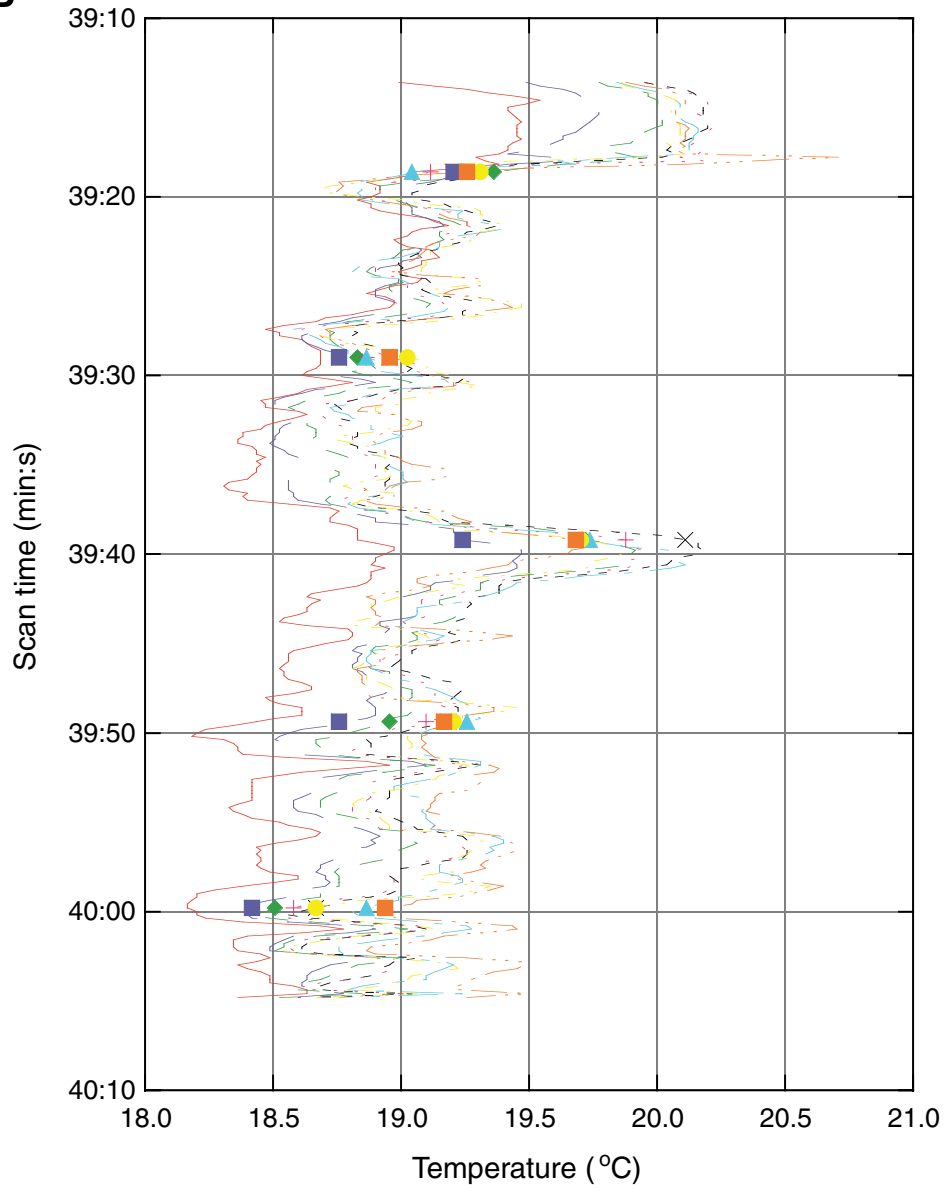
Figure F12. IR scan showing higher temperature (spot 2) of void compared to adjacent sediment (spot 1).
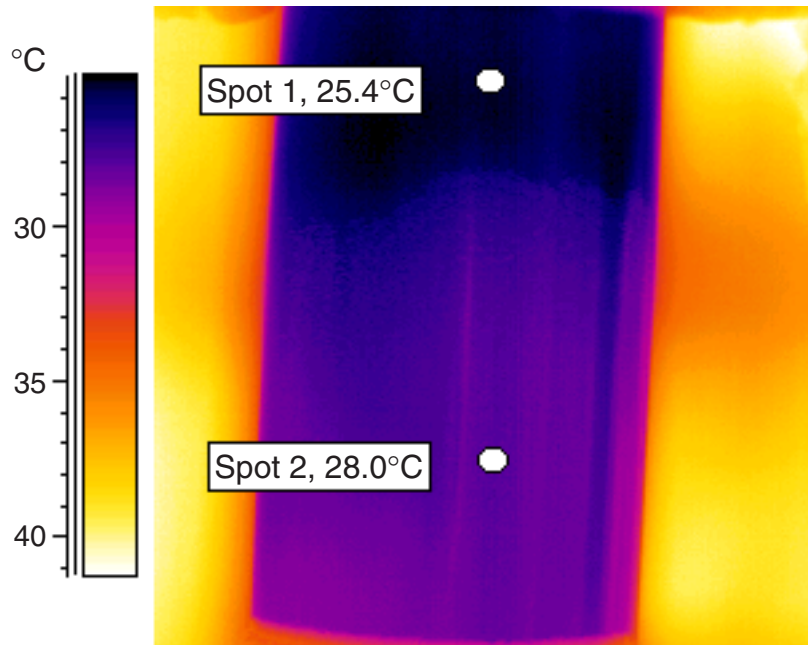
Figure F13. A. Emissivity of sediment setup, with *e* = 0.95. Sediment with tape is on the right; sediment without tape is on the left. **B.** Increase in calculated temperature when *e* = 0.84. At this emissivity value, the temperature of the sediment without tape matches the thermistor temperature.
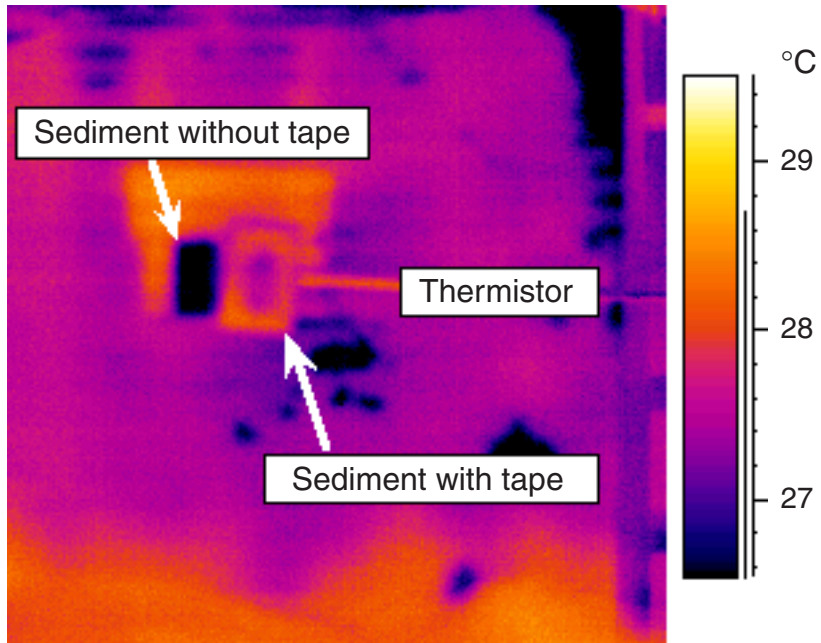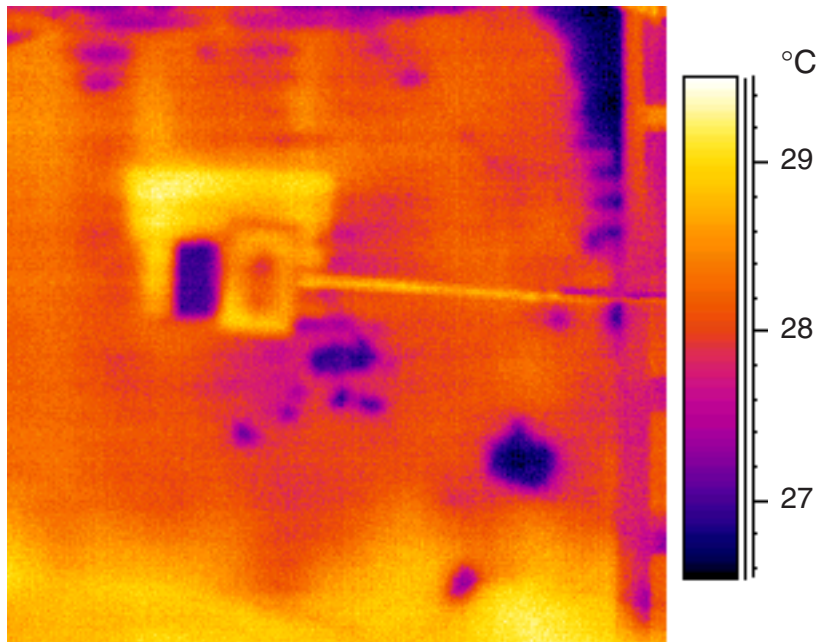
Figure F14. Comparison of magnetic susceptibility data derived from the multisensor track for Holes 1226B, 1226E, and 846B.
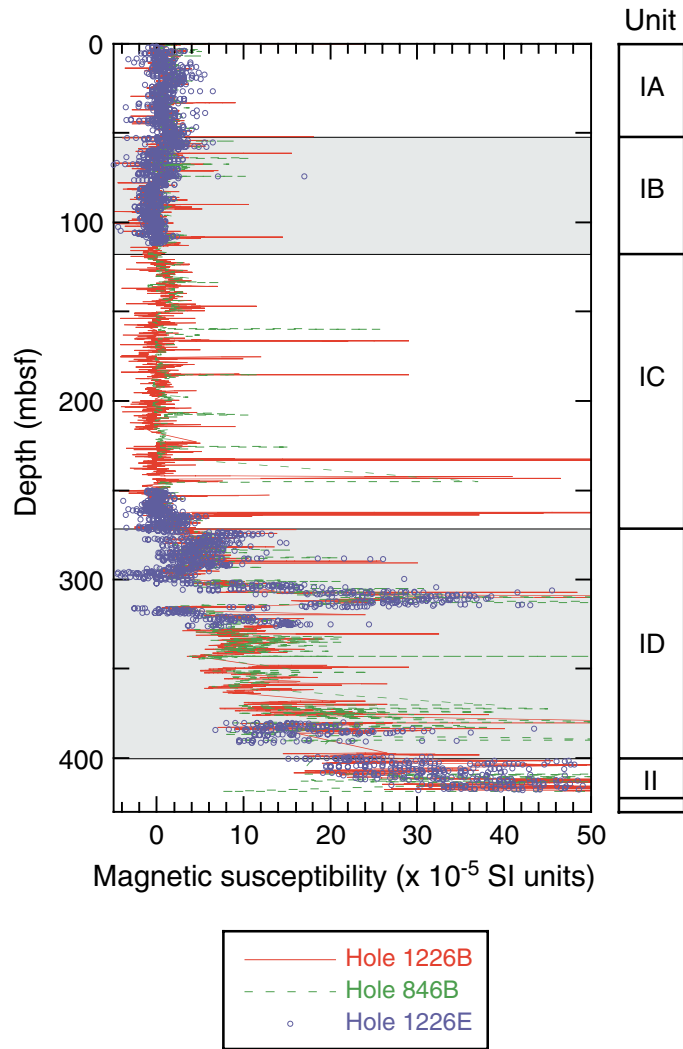
Figure F15. Cyclicity of reflectance and magnetic susceptibility data, using a five-point moving average on each data set. Shaded boxes highlight areas of particularly good inverse correlation.
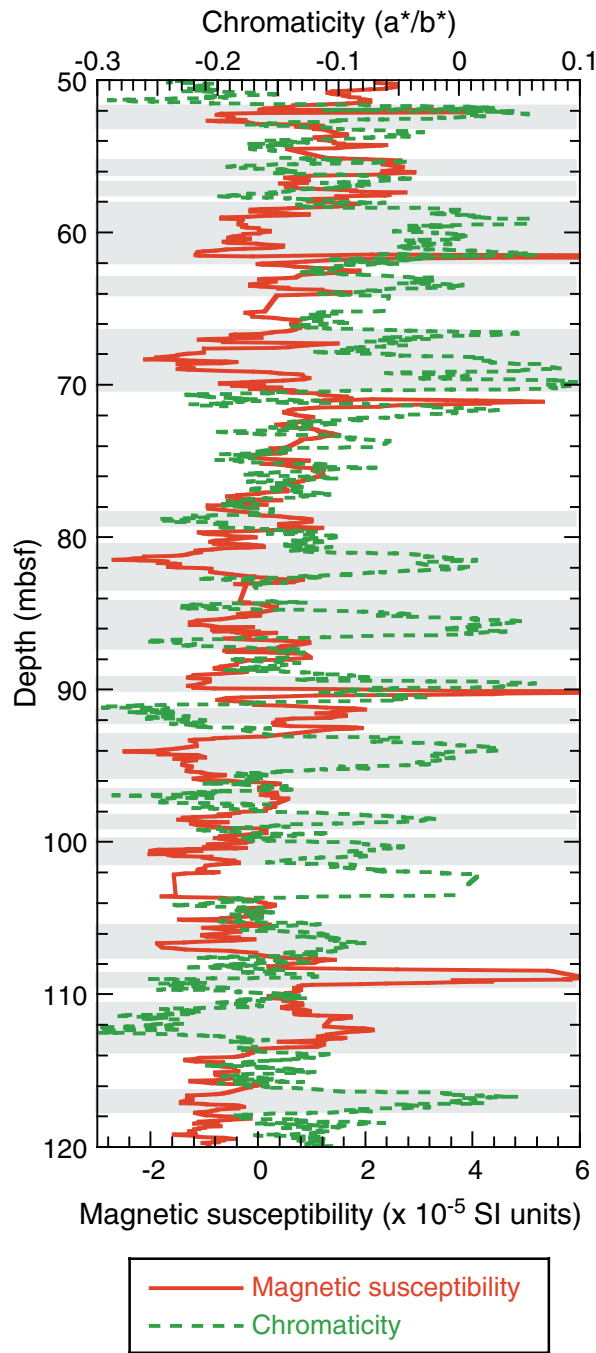
Figure F16. Magnetic intensity in Hole 1226E and magnetic susceptibility of Hole 1226B. Open squares = NRM intensity, solid squares = intensity after 20-mT AF demagnetization.
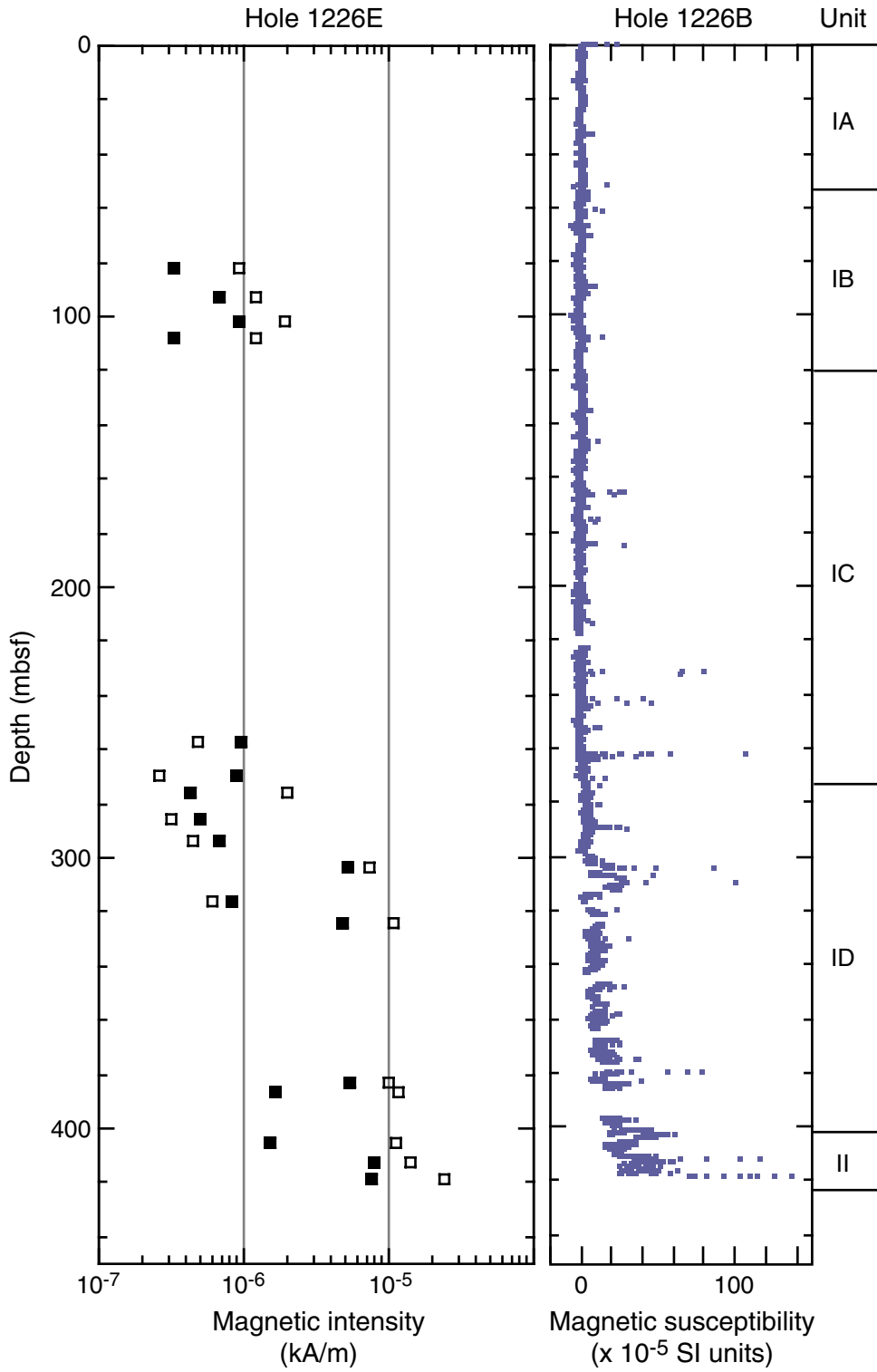
Figure F17. Principal component analysis of natural remanent magnetization (NRM) of Sample 201-1226E-18H-6, 55–57 cm, including equal area projection of directions of magnetization during demagnetization, intensity of magnetization plotted vs. demagnetization, and vector component diagrams showing projection of magnetic vector's endpoints on horizontal and vertical planes.

Sample 201-1226E-18H-6, 55-57 cm
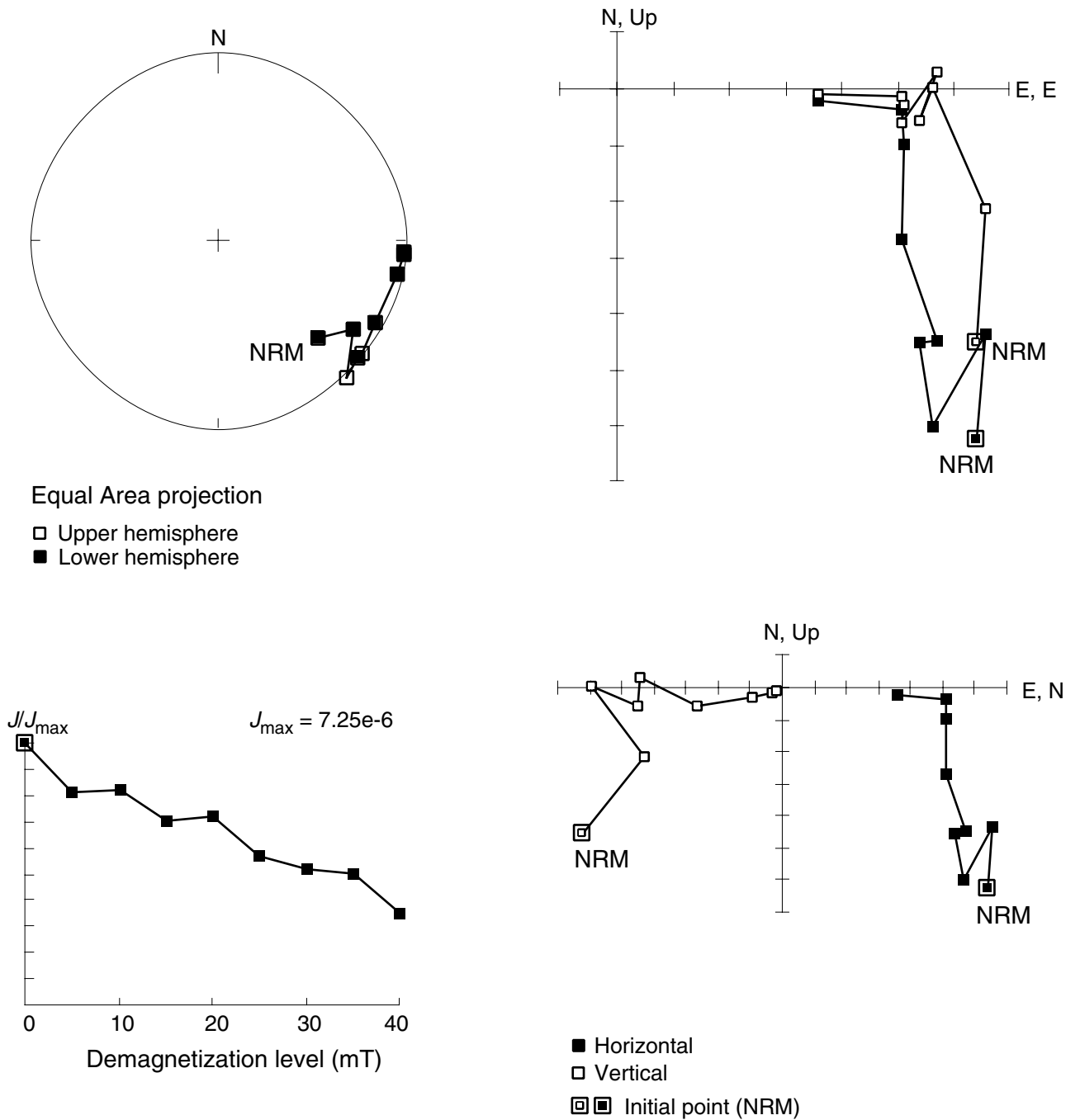
Figure F18. Principal component analysis of natural remanent magnetization (NRM) of Sample 201-1226E-22X-3, 31–33 cm, including equal area projection of directions of magnetization during demagnetization, intensity of magnetization plotted vs. demagnetization, and vector component diagrams showing projection of magnetic vector's endpoints on horizontal and vertical planes.

Sample 201-1226E-22X-3, 31-33 cm
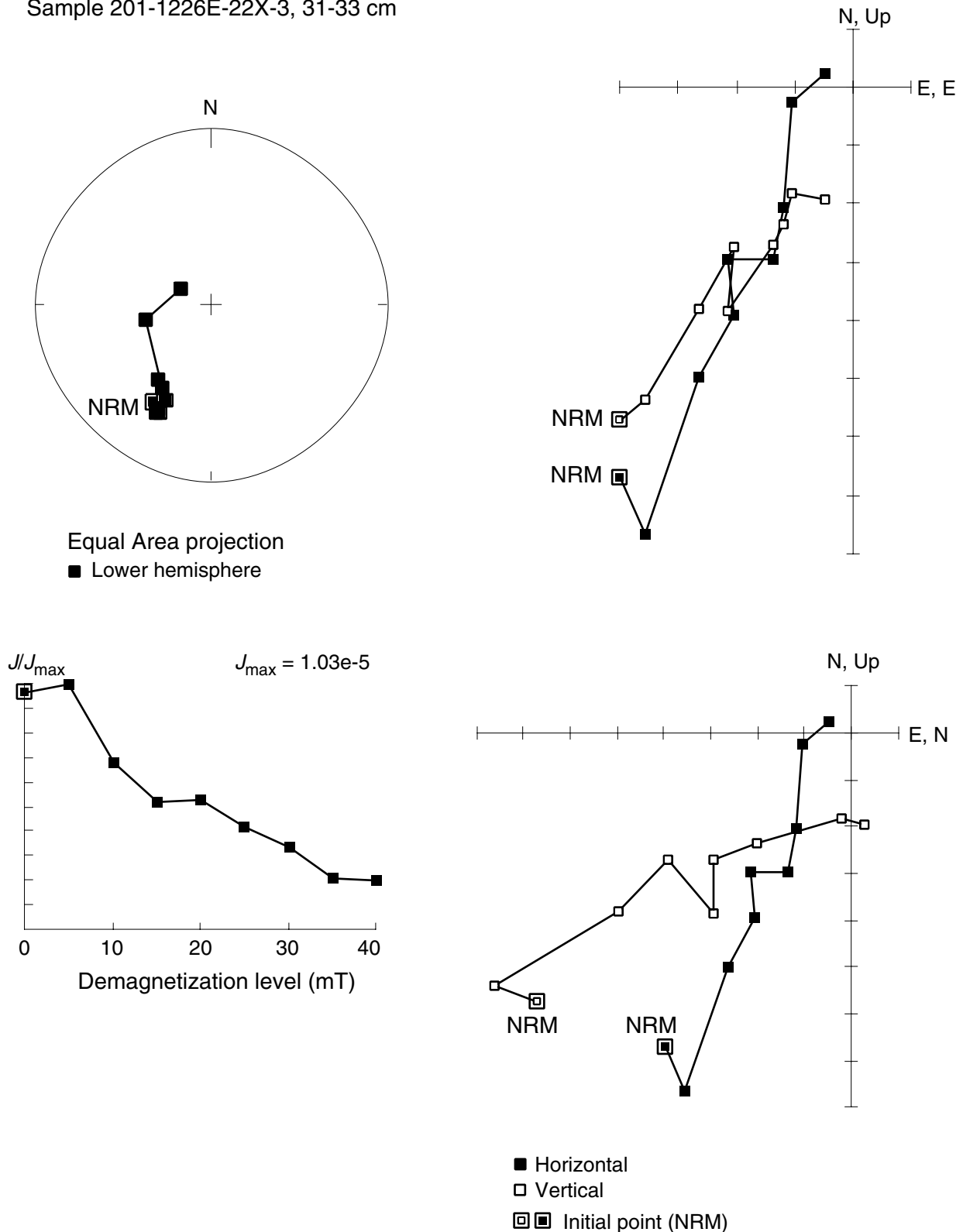
Figure F19. Principal component analysis of natural remanent magnetization (NRM) of Sample 201-1226E-25X-3, 112–114 cm, including equal area projection of directions of magnetization during demagnetization, intensity of magnetization plotted vs. demagnetization, and vector component diagrams showing projection of magnetic vector's endpoints on horizontal and vertical planes.

Sample 201-1226E-25X-3, 112-114 cm
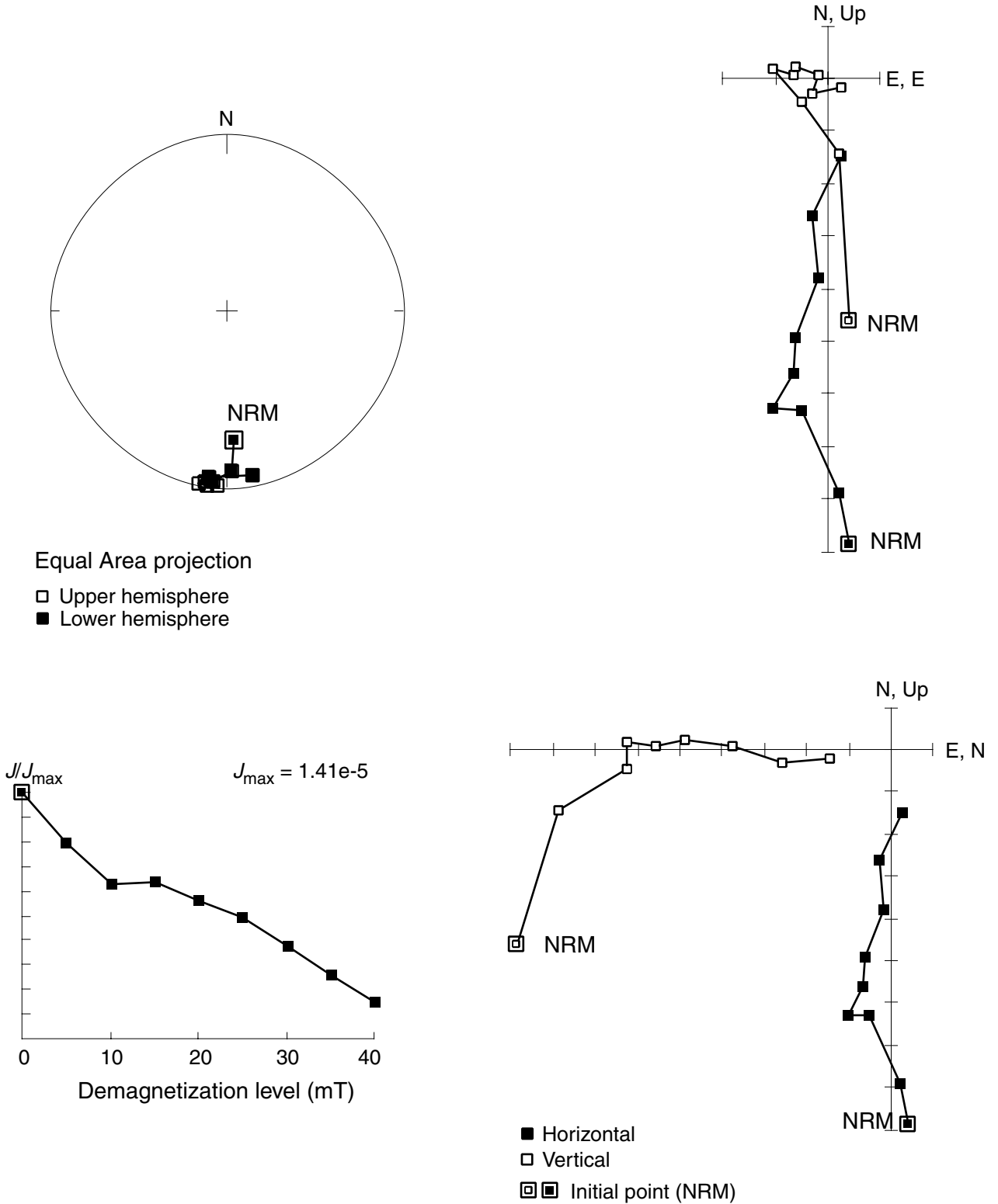
Figure F20. Principal component analysis of natural remanent magnetization (NRM) of Sample 201-1226E-25X-CC, 13–15 cm, including equal area projection of directions of magnetization during demagnetization, intensity of magnetization plotted vs. demagnetization, and vector component.

Sample 201-1226E-25X-CC, 13-15 cm

Equal Area projection
■ Lower hemisphere

J_{max} = 2.46e-5

J/J_{max}

Demagnetization level (mT)

■ Horizontal
□ Vertical
▣ ▣ Initial point (NRM)
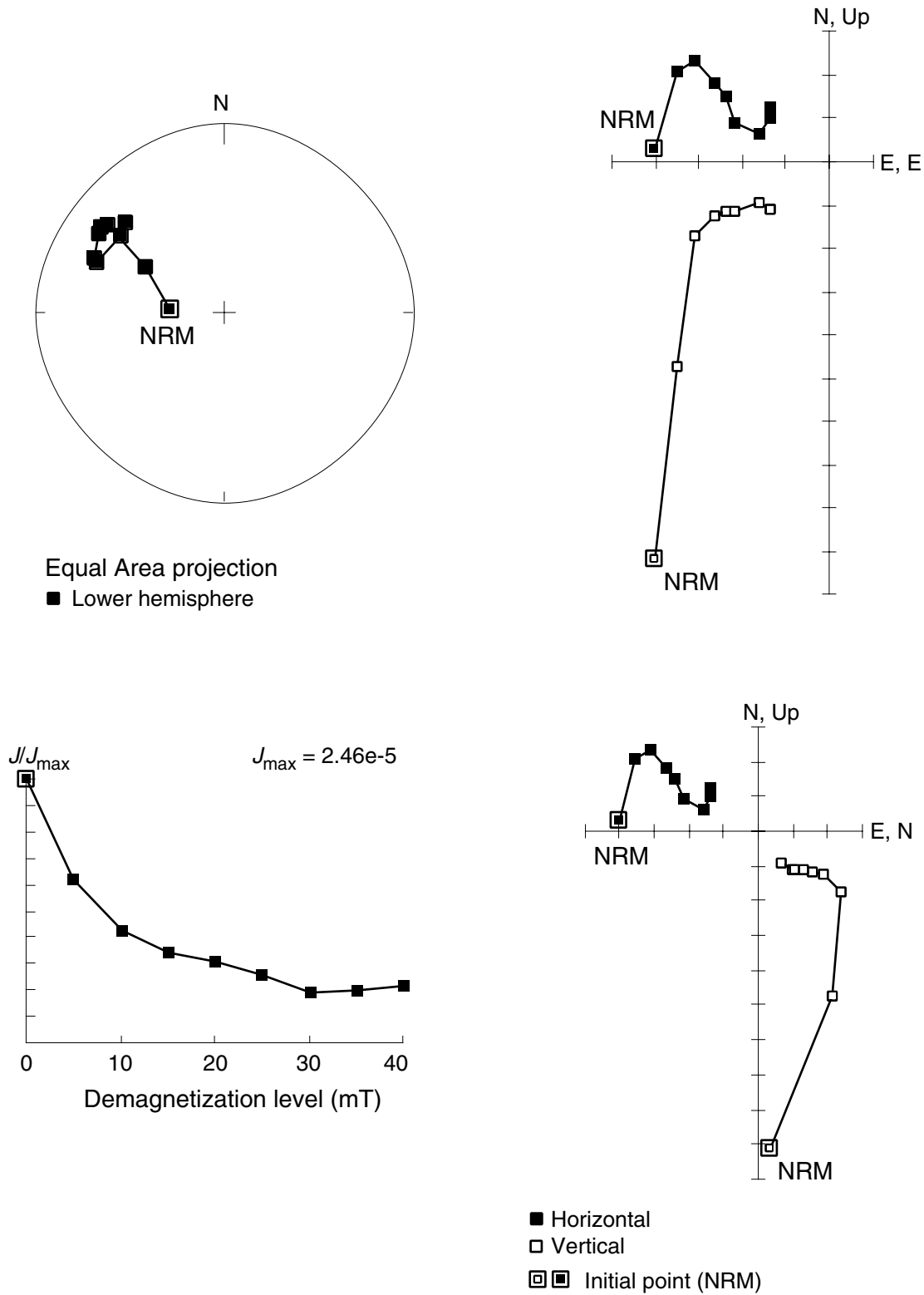
Figure F21. Comparison of gamma ray attenuation (GRA) bulk density data from Holes 1226B and 1226E with those from Hole 846B.
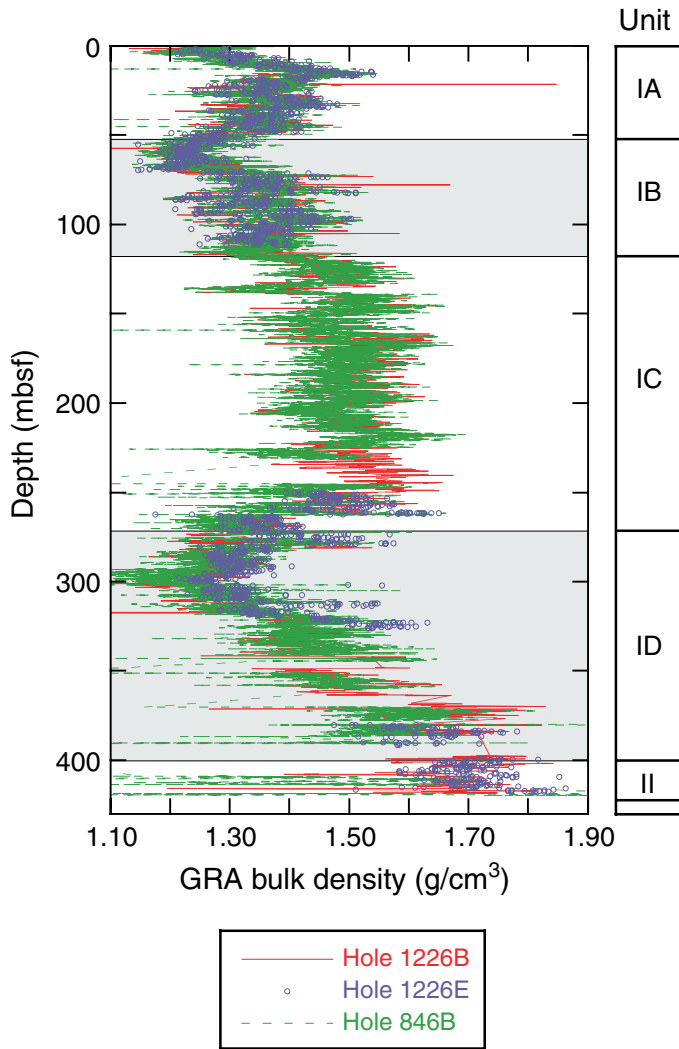
Figure F22. Comparison of 5-m moving averages of GRA bulk density from Holes 1226B, 846B, and mass/volume-based densities computed from moisture and density (MAD) measured on samples from Hole 1226B. The GRA measurements for Holes 1226B and 846B are statistically identical except for the intervals between the advanced hydraulic piston corer (APC)–extended core barrel (XCB) core transition (207–272 mbsf) and between ~380 and 418 mbsf.
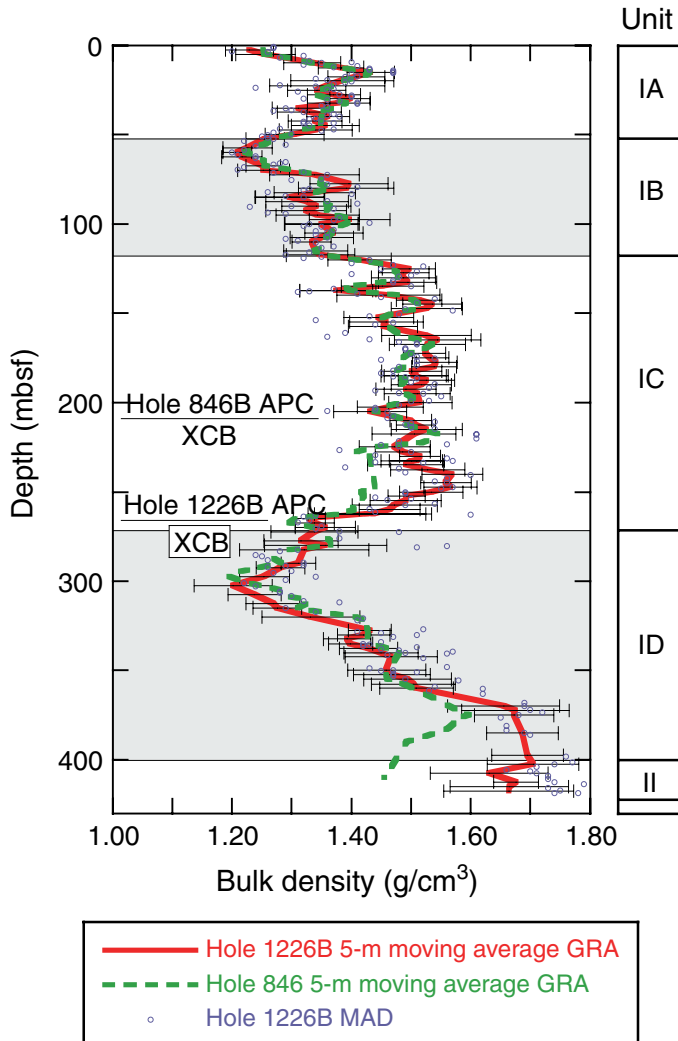
Figure F23. Mass/volume moisture and density measurements (MAD) for Hole 1226B. **A.** Gamma ray attenuation (GRA) and MAD bulk density profiles. **B.** Hole 1226B grain density profile. Note the diatom-enriched intervals at the tops of Subunits IB and ID, respectively. **C.** Porosity profile showing substantial porosity increase at the tops of Subunits IB and ID, respectively, probably due to increased intrafrustule pore volume.
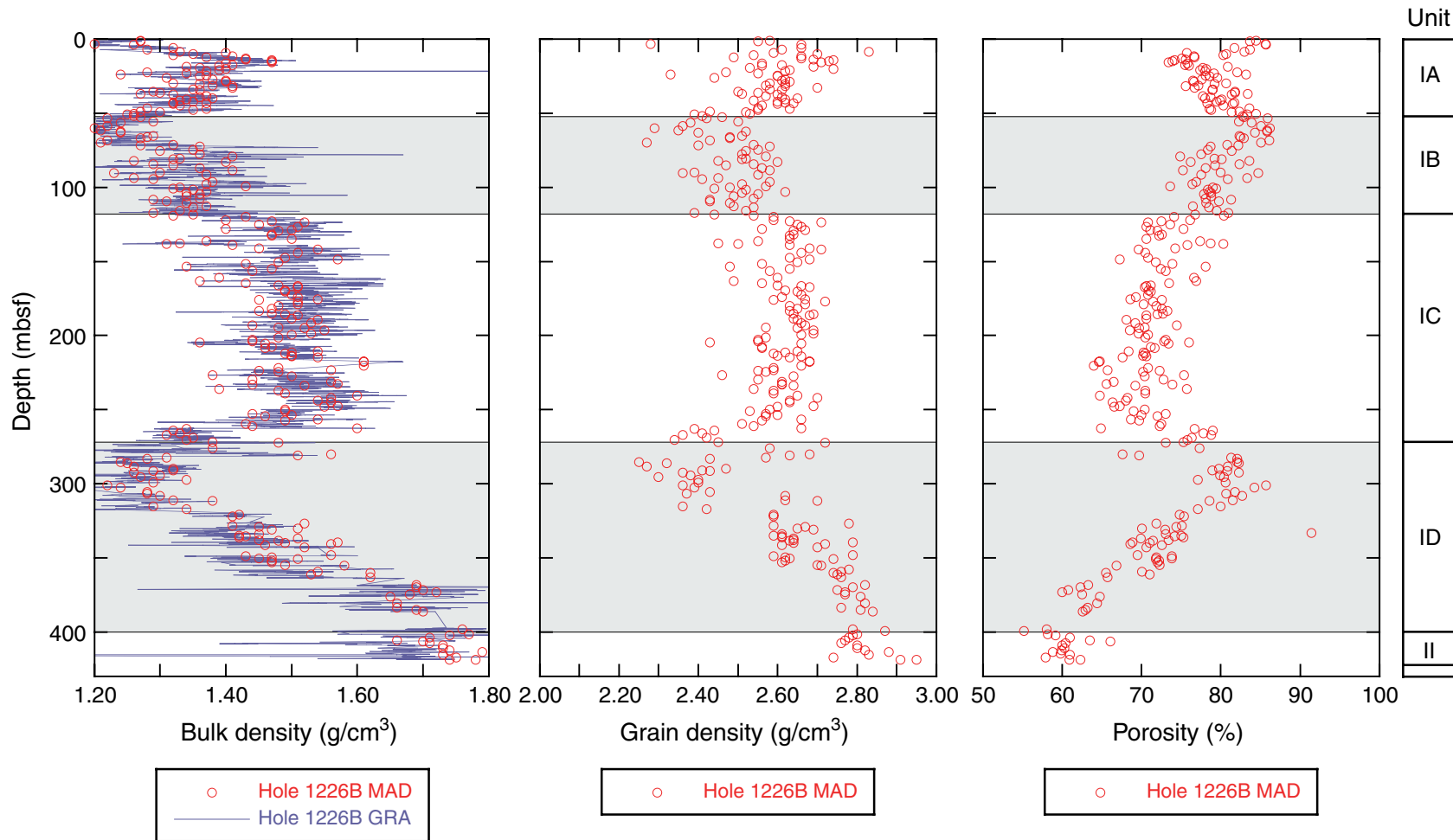
Figure F24. *P*-wave velocity profiles derived from *P*-wave logger (PWL) and PWS3 measurements for Site 1226 and Hole 846B sonic logs. Thick black lines over five distinct depth intervals represent minimum and maximum velocities measured shipboard. Additional discussion of the downhole variation in PWS3 and logging measurements and of the analysis to determine the minimum-maximum shipboard velocity constraints is provided in **"Comparison with Site 846 Wireline *P*-Wave Velocity Log,"** p. 30, in "Compressional Wave Velocity" in "Physical Properties."
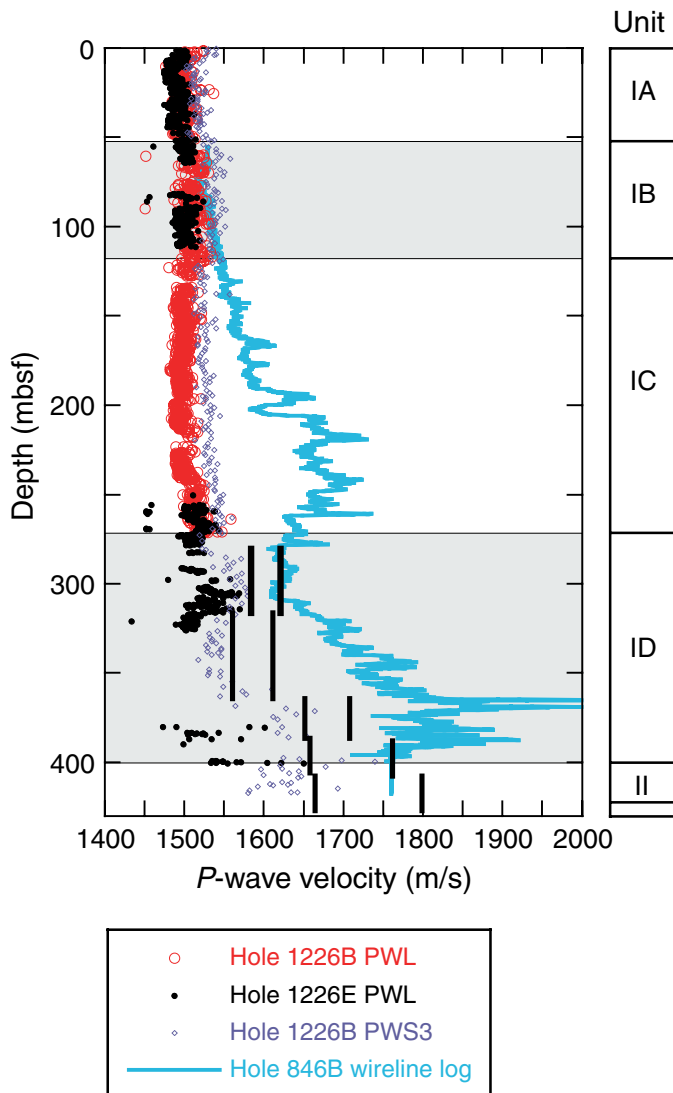
Figure F25. (A) Natural gamma ray (NGR) and (B) radioactive element composition profiles show the effects of uranium enrichment due to highly reducing redox conditions associated with organic carbon in shallow sediments. MST = multisensor track.
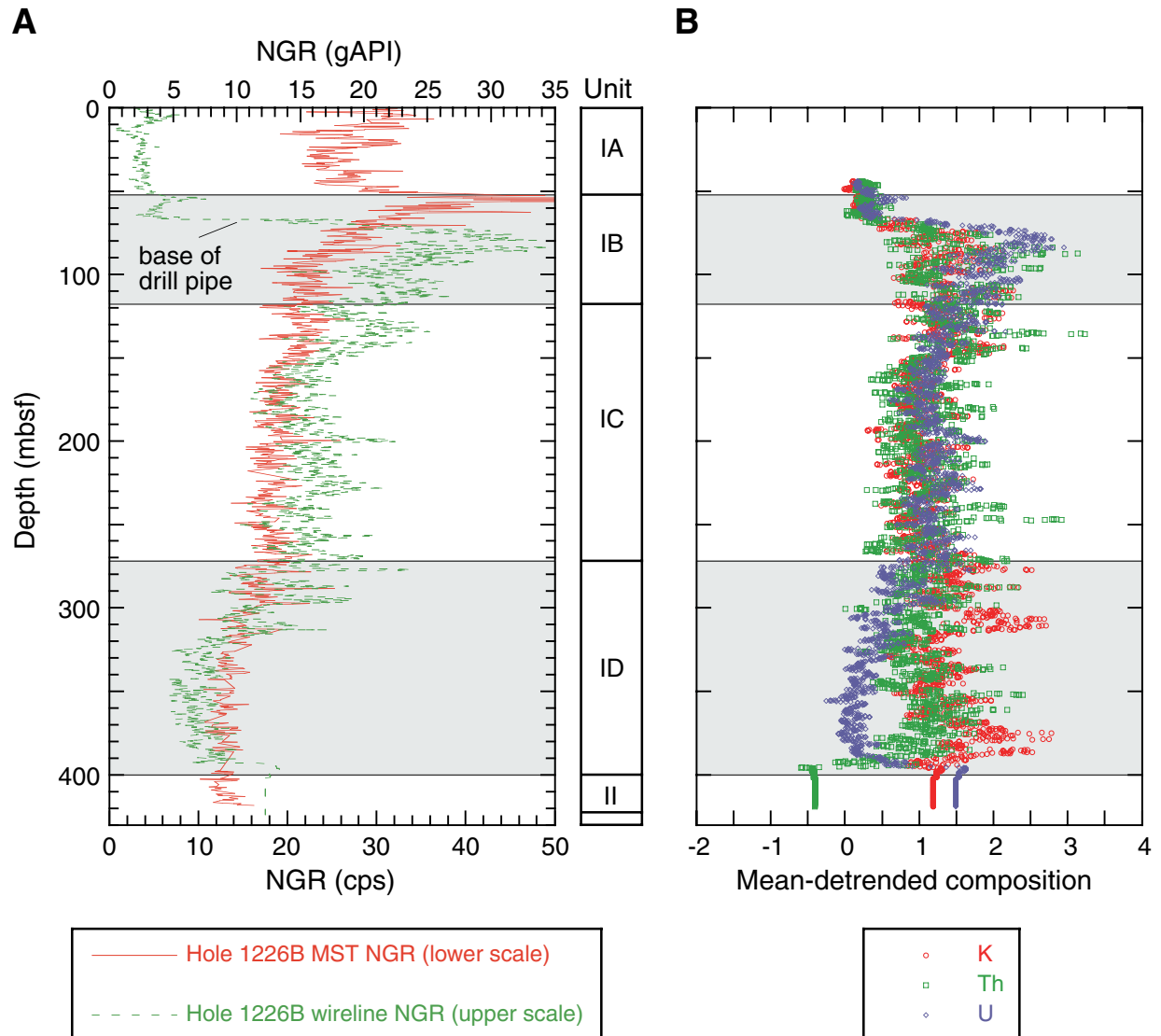
Figure F26. Thermal conductivity measurements for Hole 1226B. **A.** Thermal conductivity profile (needle probe method). **B.** Mean-detrended bulk density and thermal conductivity profiles illustrate the controlling effect of water content variability on thermal properties.
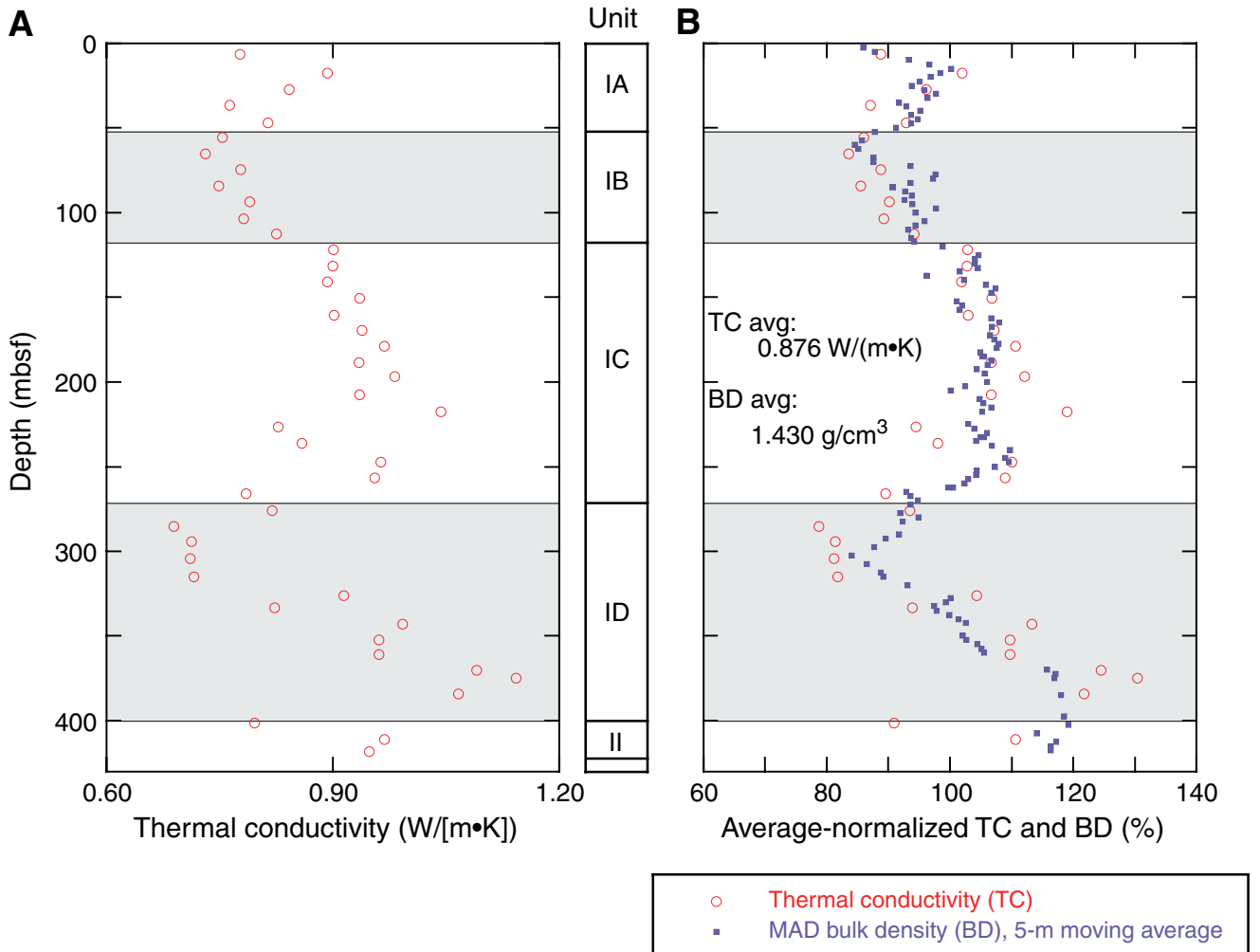
Figure F27. Formation factor profile. Increasing consolidation is depicted in the rapid formation factor increase below ~305 mbsf, consistent with shipboard and Hole 846B logging *P*-wave velocities. Resistivity data were not collected below 375 mbsf due to instrument maintenance. The framed area indicates values obtained for intact core biscuits into which holes were drilled to prevent splitting of the core during insertion of the probe. They are considered to represent the more reliable data.
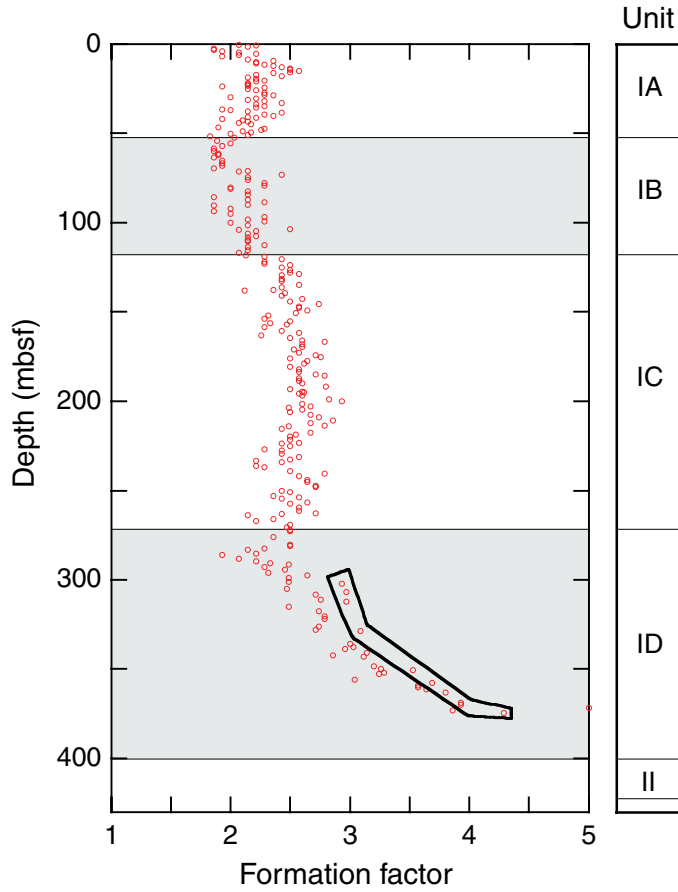
Figure F28. A. All temperatures measured in Hole 1226A plotted vs. depth with best-fit linear profile. **B.** In situ temperature data shown with a steady-state conductive profile computed using the thermal conductivities measured on cores from Hole 1226B. DVTP = Davis-Villinger Temperature Probe.
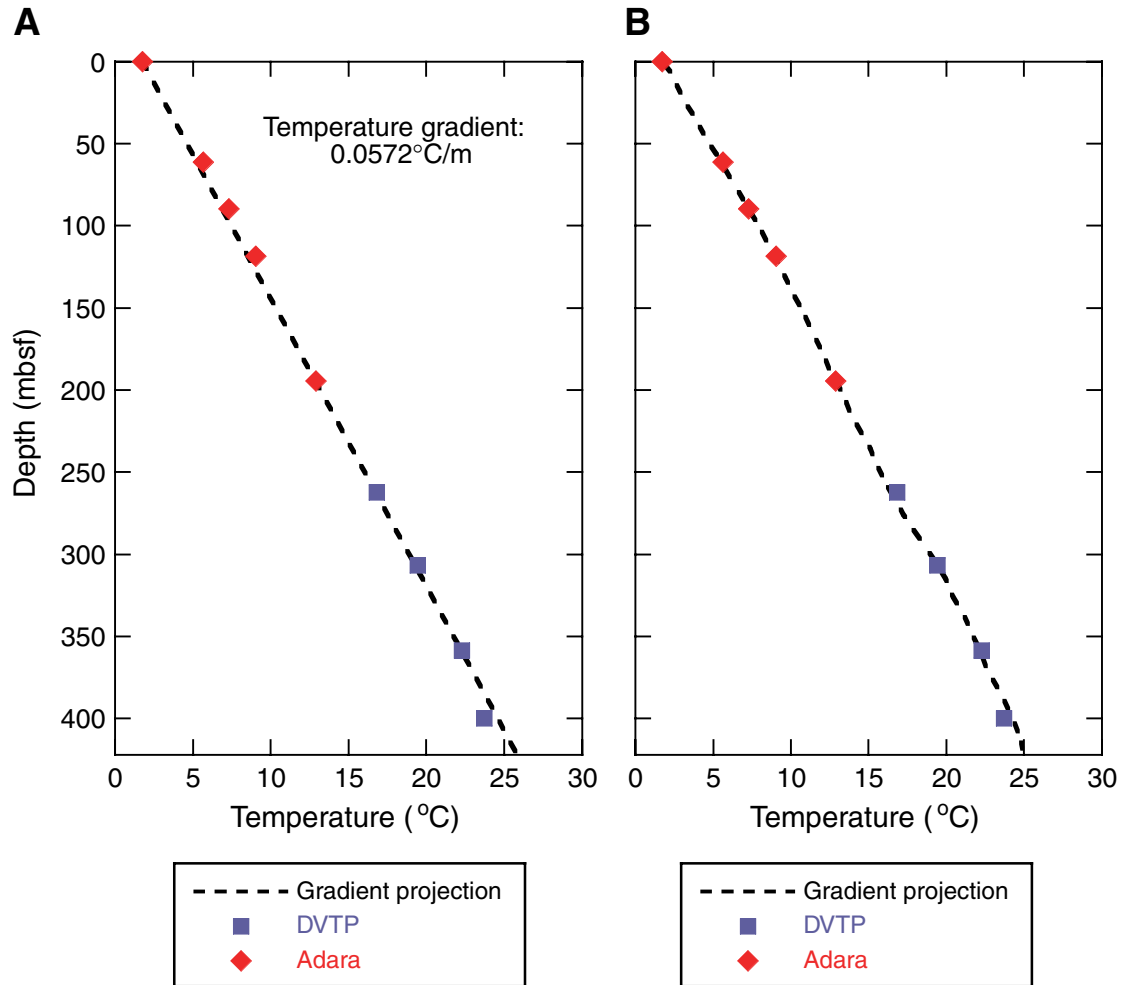
Figure F29. Pressure measured in Hole 1226E during the DVTP-P station after Core 201-1226E-21H. Rapid drop-off and noise during the 20-min equilibration period indicate that the formation did not form an adequate seal around the probe.
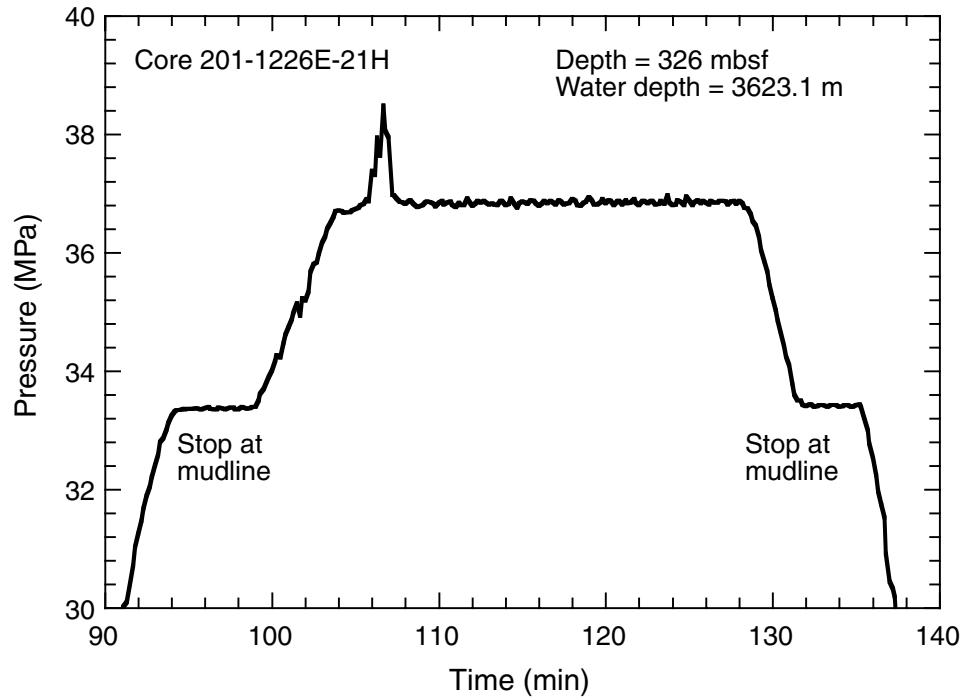
Figure F30. Pressure record from PCS core 201-1226B-42P monitored from the time of recovery to opening.

Figure F31. Main logs recorded in Hole 1226B. **A.** The hole diameter is measured by the caliper arm of the density sonde. **B.** Gamma ray count is a measure of the natural radioactivity of the formation. **C.** Concentrations of potassium, thorium, and uranium derived from the gamma ray counts. **D.** Resistivity measured by the Phasor Dual Induction tool with three depths of investigation. **E.** Density log (red line) compared with density measurements made on core samples (shaded circles) (see **"Density and Porosity,"** p. 29, in "Physical Properties"). **F.** Porosity log for the two receivers spacings of the Accelerator Porosity Sonde (APS) compared with porosity measurements made on core samples (shaded circles) (see **"Density and Porosity,"** p. 29, in "Physical Properties"). HNGS = Hostile Environment Natural Gamma Ray Sonde, SGT = Scintillation Gamma Ray Tool

Figure F32. Comparison between logs from Hole 1226B (red) and the data recorded during ODP Leg 138 in neighboring Hole 846B (green). **A.** Hole diameter. **B.** Gamma radiation. **C.** Thorium. **D.** Uranium. **E.** Potassium. **F.** Medium resistivity. **G.** Density.
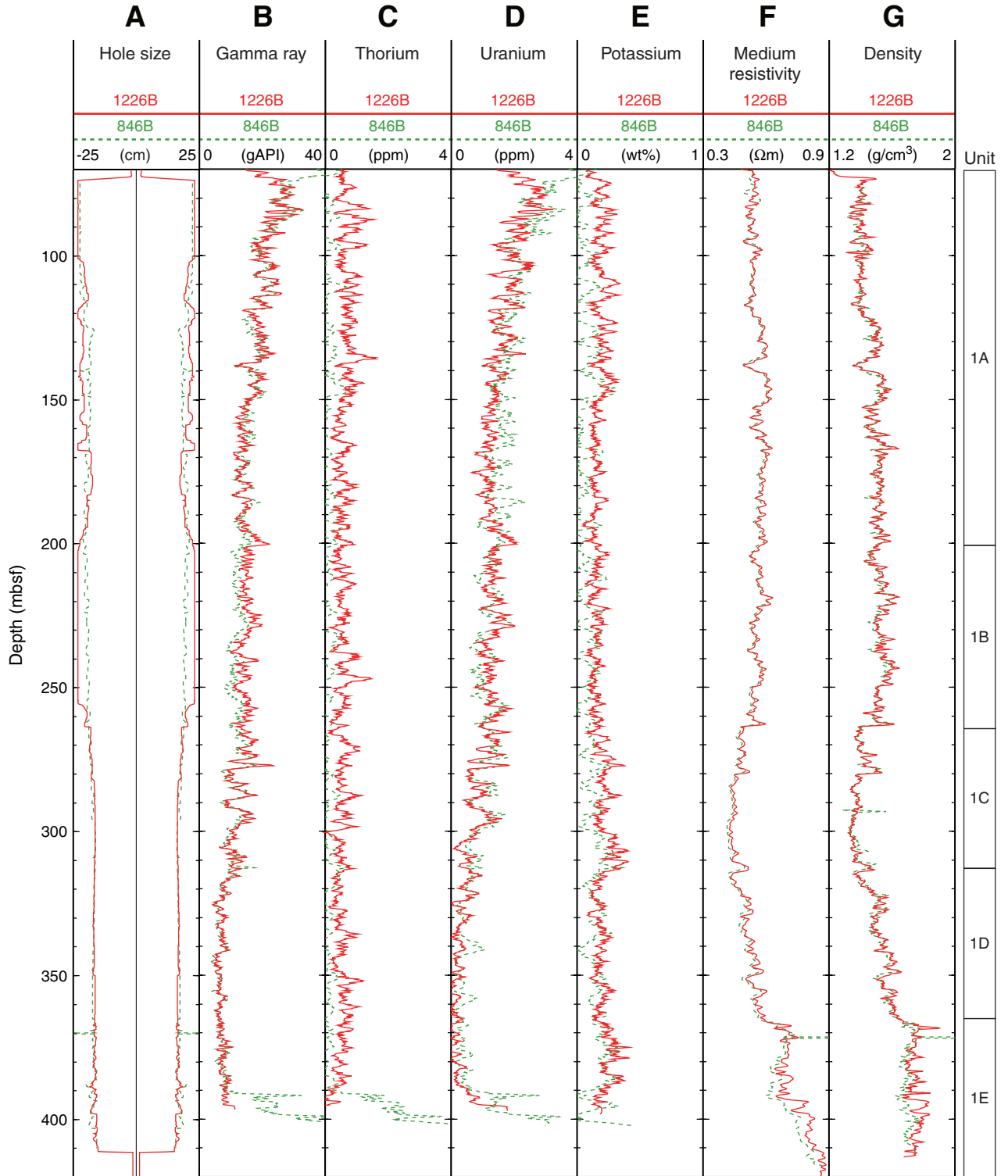
Figure F33. Temperature log recorded in Hole 1226B. Temperature data were recorded continuously during the two passes of the tool string.
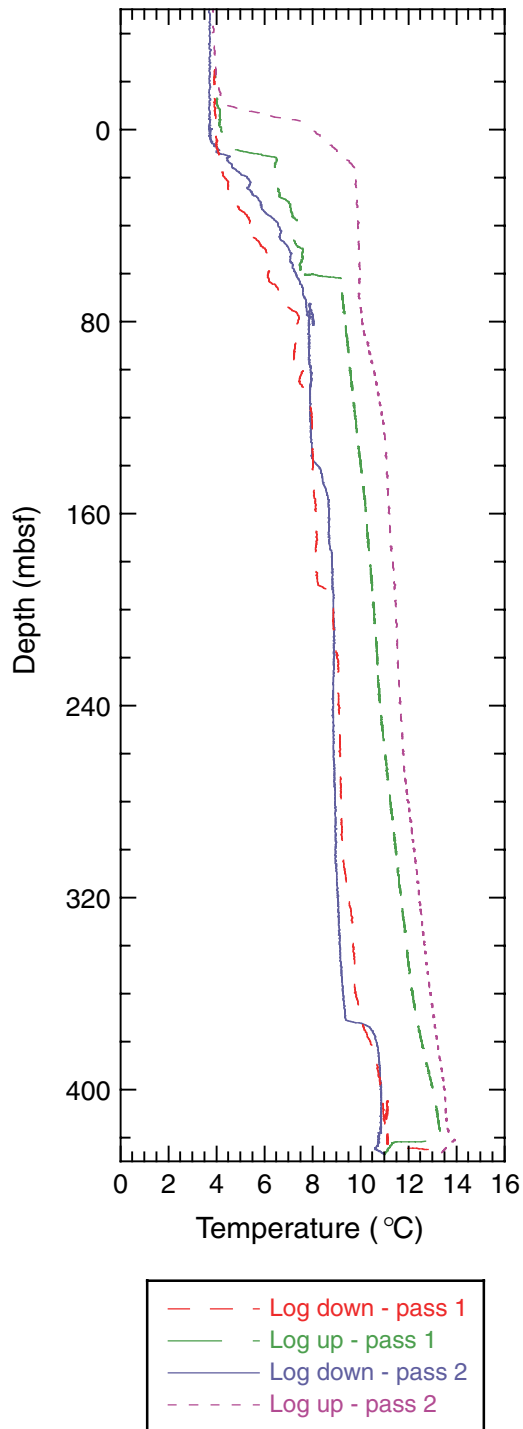
Table T1. Coring summary, Site 1226. (Continued on next two pages.)

Hole 1226A
Latitude: 3°5.6688′N
Longitude: 90°49.0785′W
Time on site (hr): 149.25 (1100 hr, 19 Feb–1615 hr, 25 Feb 2002)
Time on hole (hr): 9.5 (1100 hr, 19 Feb–2030 hr, 19 Feb 2002)
Seafloor (drill pipe measurement from rig floor, mbrf): 3308.0
Distance between rig floor and sea level (m): 11.1
Water depth (drill pipe measurement from sea level, m): 3296.9
Total depth (drill pipe measurement from rig floor, mbrf): 3317.5
Total penetration (meters below seafloor, mbsf): 9.5
Total length of cored section (m): 9.5
Total core recovered (m): 9.43
Core recovery (%): 99.26
Total number of cores: 1

Hole 1226B
Latitude: 3°5.6686′N
Longitude: 90°49.0793′W
Time on hole (hr): 86.25 (2030 hr, 19 Feb–1045 hr, 23 Feb 2002)
Seafloor (drill pipe measurement from rig floor, mbrf): 3308.1
Distance between rig floor and sea level (m): 11.1
Water depth (drill pipe measurement from sea level, m): 3297.0
Total depth (drill pipe measurement from rig floor, mbrf): 3729.5
Total penetration (meters below seafloor, mbsf): 421.4
Total length of cored section (m): 418.9
Total length of drilled intervals (m): 2.5
Total core recovered (m): 413.69
Core recovery (%): 98.8
Total number of cores: 47
Total number of drilled intervals: 2

Hole 1226C
Latitude: 3°5.6477′N
Longitude: 90°49.0789′W
Time on hole (hr): 1.5 (1045 hr, 23 Feb–1215 hr, 23 Feb 2002)
Seafloor (drill pipe measurement from rig floor, mbrf): 3307.6
Distance between rig floor and sea level (m): 11.2 m
Water depth (drill pipe measurement from sea level, m): 3296.4
Total depth (drill pipe measurement from rig floor, mbrf): 3315.5
Total penetration (meters below seafloor, mbsf): 7.9
Total length of cored section (m): 7.9
Total core recovered (m): 7.91
Core recovery (%): 100.1
Total number of cores: 1

Hole 1226D
Latitude: 3°5.6460′N
Longitude: 90°49.0806′W
Time on hole (hr): 0.75 (1215 hr, 23 Feb–1300 hr, 23 Feb 2002
Seafloor (drill pipe measurement from rig floor, mbrf): 3307.9
Distance between rig floor and sea level (m): 11.2
Water depth (drill pipe measurement from sea level, m): 3296.7
Total depth (drill pipe measurement from rig floor, mbrf): 3315.5
Total penetration (meters below seafloor, mbsf): 7.6
Total length of cored section (m): 7.6
Total core recovered (m): 7.64
Core recovery (%): 100
Total number of cores: 1

Hole 1226E
Latitude: 3°5.6430′N
Longitude: 90°49.0793′W
Time on hole (hr): 51.25 (1300 hr, 23 Feb–1615 hr, 25 Feb 2002)
Seafloor (drill pipe measurement from rig floor, mbrf): 3307.6
Distance between rig floor and sea level (m): 11.2
Water depth (drill pipe measurement from sea level, m): 3296.4
Total depth (drill pipe measurement from rig floor, mbrf): 3726.0
Total penetration (meters below seafloor, mbsf): 418.4
Total length of cored section (m): 227.5
Total length of drilled intervals (m): 190.9
Total core recovered (m): 226.96
Core recovery (%): 99.76
Total number of cores: 25
Total number of drilled intervals: 3

Table T1 (continued).

Core	Date (Feb 2002)	Local time (hr)	Depth (mbsf) Top	Depth (mbsf) Bottom	Length (m) Cored	Length (m) Recovered	Recovery (%)
201-1226A-							
1H	19	1950	0.0	9.5	9.5	9.43	99.3
				Cored totals:	9.5	9.43	99.3
201-1226B-							
1H	19	2050	0.0	4.4	4.4	4.40	100.0
2H	19	2215	4.4	13.9	9.5	10.07	106.0
3H	19	2330	13.9	23.4	9.5	9.95	104.7
4H	20	0055	23.4	32.9	9.5	9.95	104.7
5H	20	0230	32.9	42.4	9.5	9.64	101.5
6H	20	0330	42.4	51.9	9.5	9.88	104.0
7H	20	0500	51.9	61.4	9.5	10.18	107.2
8H	20	0600	61.4	70.9	9.5	10.04	105.7
9H	20	0705	70.9	80.4	9.5	10.00	105.3
10H	20	0840	80.4	89.9	9.5	9.72	102.3
11H	20	0945	89.9	99.4	9.5	9.63	101.4
12H	20	1050	99.4	108.9	9.5	9.48	99.8
13H	20	1235	108.9	118.4	9.5	9.87	103.9
14H	20	1335	118.4	127.9	9.5	10.00	105.3
15H	20	1430	127.9	137.4	9.5	10.14	106.7
16H	20	1605	137.4	146.9	9.5	10.31	108.5
17H	20	1700	146.9	156.4	9.5	9.90	104.2
18H	20	1800	156.4	165.9	9.5	10.10	106.3
19H	20	1900	165.9	175.4	9.5	10.08	106.1
20H	20	2000	175.4	184.9	9.5	10.15	106.8
21H	20	2140	184.9	194.4	9.5	10.12	106.5
22H	21	0020	194.4	203.9	9.5	10.13	106.6
23H	21	0140	203.9	213.4	9.5	10.14	106.7
24H	21	0300	213.4	222.9	9.5	10.12	106.5
25H	21	0420	222.9	232.4	9.5	10.02	105.5
26H	21	0620	232.4	241.9	9.5	10.11	106.4
			*****Drilled from 241.9 to 243.4 mbsf*****				
27H	21	0945	243.4	252.9	9.5	10.14	106.7
28H	21	1110	252.9	262.4	9.5	10.18	107.2
29H	21	1445	262.4	271.9	9.5	9.98	105.1
30X	21	1600	271.9	281.5	9.6	9.74	101.5
31X	21	1700	281.5	290.8	9.3	9.83	105.7
32X	21	1810	290.8	300.5	9.7	8.60	88.7
33X	21	1925	300.5	310.2	9.7	8.22	84.7
34X	21	2205	310.2	319.8	9.6	7.52	78.3
35X	21	2315	319.8	329.4	9.6	9.76	101.7
36X	22	0020	329.4	339.0	9.6	9.75	101.6
37X	22	0120	339.0	348.7	9.7	9.76	100.6
38X	22	0220	348.7	358.4	9.7	9.50	97.9
39X	22	0520	358.4	368.1	9.7	5.98	61.7
40X	22	0715	368.1	371.1	3.0	2.42	80.7
41X	22	0845	371.1	378.0	6.9	6.00	87.0
42P	22	1010	378.0	379.0	1.0	1.66	166.0
			*****Drilled from 379.0 to 380.0 mbsf*****				
43X	22	1110	380.0	387.6	7.6	6.71	88.3
44X	22	1235	387.6	397.2	9.6	0.21	2.2
45X	22	1430	397.2	406.8	9.6	9.83	102.4
46X	22	1630	406.8	416.4	9.6	9.52	99.2
47X	22	1855	416.4	421.4	5.0	4.25	85.0
				Cored totals:	418.9	413.69	98.8
				Drilled total:	2.5		
				Total:	421.4		
201-1226C-							
1H	23	1220	0.0	7.9	7.9	7.91	100.1
				Cored totals:	7.9	7.91	100.1
201-1226D-							
1H	23	1305	0.0	7.6	7.6	7.64	100.5
				Cored totals:	7.6	7.64	100.5
201-1226E-							
1H	23	1420	0.0	7.6	7.6	7.57	99.6
2H	23	1510	7.6	17.1	9.5	9.87	103.9
3H	23	1605	17.1	26.6	9.5	9.66	101.7
4H	23	1705	26.6	36.1	9.5	9.83	103.5

Table T1 (continued).

Core	Date (Feb 2002)	Local time (hr)	Depth (mbsf) Top	Bottom	Length (m) Cored	Recovered	Recovery (%)
5H	23	1840	36.1	45.6	9.5	9.62	101.3
6H	23	1940	45.6	55.1	9.5	10.06	105.9
7H	23	2035	55.1	64.6	9.5	9.73	102.4
8H	23	2155	64.6	74.1	9.5	10.17	107.1
9H	23	2245	74.1	83.6	9.5	10.01	105.4
10H	24	0015	83.6	93.1	9.5	10.11	106.4
11H	24	0110	93.1	102.6	9.5	9.92	104.4
12H	24	0310	102.6	112.1	9.5	9.62	101.3
*****Drilled from 112.1 to 250.0 mbsf*****							
13H	24	0755	250.0	259.5	9.5	10.19	107.3
14H	24	0915	259.5	269.0	9.5	10.17	107.1
15H	24	1030	269.0	278.5	9.5	10.06	105.9
16H	24	1150	278.5	288.0	9.5	10.06	105.9
17H	24	1340	288.0	297.5	9.5	10.06	105.9
18H	24	1515	297.5	307.0	9.5	10.01	105.4
19H	24	1835	307.0	316.5	9.5	9.73	102.4
20H	24	2000	316.5	326.0	9.5	9.93	104.5
*****Drilled from 326.0 to 378.0 mbsf*****							
21P	25	0230	378.0	379.0	1.0	1.02	102.0
*****Drilled from 379.0 to 380.0 mbsf*****							
22X	25	0355	380.0	389.6	9.6	7.95	82.8
23X	25	0515	389.6	399.2	9.6	2.11	22.0
24X	25	0825	399.2	408.8	9.6	9.72	101.3
25X	25	0940	408.8	418.4	9.6	9.78	101.9
			Cored totals:		227.5	226.96	99.8
			Drilled total:		190.9		
			Total:		418.4		

Table T2. Comparison of basalt compositions from Hole 846B (Leg 138) and Hole 1226B (Leg 201). (**See table notes.** Continued on next page.)

Core, section, Interval (cm):	138-846B-45X-1 76–79	201-1226B-47X-CC 42–44	Standard BIR-1	SRM reported value
Major element oxide (wt%):				
SiO_2	51.81	51.19	47.93	47.96
TiO_2	1.07	0.99	0.98	0.96
Al_2O_3	16.39	16.62	15.43	15.5
Fe_2O_3*	10.05	10.14	11.25	11.3
MnO	0.19	0.14	0.16	0.18
MgO	8.22	7.19	9.24	9.7
CaO	10.26	10.54	13.05	13.3
Na_2O	2.32	2.61	1.71	1.82
K_2O	0.74	0.27	0.02	0.03
P_2O_5	0.06	0.04	0.02	0.02
LOI	3.49	4.2	2	
Total	101.11	99.73	99.79	100.77
Trace element (ppm):				
Ba		8	7	7
Ni		181	147	170
Sc		34	40	44
Cr		472	356	370
Cu		128	116	125
Dy		3.37	2.61	4
Ce		4.3	3.7	1.9
Co		46.2	56.1	52
Eu		0.77	0.49	0.55
Gd		2.72	1.98	1.8
Hf		1.5	<0.5	0.6
Nd		4.7	2.7	2.5
La		1.5	0.8	0.63
Li				
Sr		137.8	108.7	110
V		205	337	310
Y		21	17.1	16
Zn		67	51	70
Zr		46.6	13.7	18
SRM informational value (ppm):				
As		2.9	0.6	0.44
B				
Be				
Cl				
F				
Ga		16.8	16.1	16
Lu		0.38	0.27	0.26
Nb		1.1	<0.5	0.6
Pb		0.3	4.5	3
Sb		0.1	0.5	0.58
Sm		2.2	1.2	1.1
Additional element (ppm):				
C		0.21		
S		0.04		
Mo		<0.1	<0.1	
Cd		0.1	<0.1	
Bi		<0.1	<0.1	
Ag		0.1	<0.1	
Au (ppb)		1.8	2.4	
Hg		0.05	<0.01	
Tl		1.1	<0.1	
Cs		0.2	<0.1	
Rb		7.2	<0.5	
Sn		<1	<1	
Ta		0.1	<0.1	
Th		<0.1	<0.1	
U		1.8	<0.1	
W		0.1	<0.1	
Pr		0.82	0.41	
Ho		0.76	0.6	
Tb		0.53	0.37	

Table T2 (continued).

Core, section, Interval (cm):	138-846B-45X-1 76–79	201-1226B-47X-CC 42–44	Standard BIR-1	SRM reported value
Er		2.46	1.78	
Tm		0.34	0.27	
Yb		2.24	1.61	

Notes: * = total iron as Fe_2O_3. SRM = standard reference material, BIR-1 = U.S. Geological Survey Icelandic basalt SRM. Leg 138 analyses were conducted by X-ray fluorescence and Leg 201 analyses were conducted by inductively coupled plasma (ICP)–atomic emission spectrophotometry (major element oxides and Ba, Ni, Sc, and Cr) and ICP-mass spectrometry (all other trace elements). Leg 201 analysis were performed by Acme Labs, Vancouver, BC. The SRM was included in the analytical suite as an unknown.

Table T3. Interstitial water chemistry, Holes 1226B and 1226E. (**See table notes.** Continued on next two pages.)

Core, section, interval (cm)	Depth (mbsf)	pH	Alk (mM)	DIC (mM)	Cl⁻ (mM)	SO₄²⁻ (mM)	H₄SiO₄ (µM)	PO₄³⁻ (µM)	NH₄⁺ (µM)	Fe (µM)	Mn (µM)	Sr (µM)	Li (µM)	Ba (µM)	Acetate (µM)	Formate (µM)	NO₃⁻ (µM)	NO₂⁻ (µM)	Ca† (mM)	K† (mM)	Mg† (mM)	ΣH₂S (mM)
201-1226B-																						
1H-1, 130–150	1.30	7.57	2.88	3.07		30.1	772	7.55	51.7	0.7	33.5	88	25.9	BDL	0.0	0.1	0.2		10.8	11.6	54.4	<0.00017
1H-3, 0–20	3.00	7.54	2.83	3.35		29.1	790	7.93	95.0	2.4	30.9	90	25.9	BDL								0.00170
2H-2, 130–150	7.20	7.56	3.46	3.97				7.02	217.3	4.5	36.6	95	26.9	BDL	0.0	0.2	0.2		10.1	12.1	54.2	0.0986
2H-5, 127–150	11.67	7.49	3.72	3.90		28.4	791	6.47	194.8	37.5	32.0	103	26.5	BDL								0.211
3H-2, 130–150	16.70	7.55	4.24	4.83		27.5		5.65	246.5	8.5	22.0	110	25.2	BDL	0.5	0.1			9.2	11.8	54.9	0.349
3H-5, 130–150	21.20	7.47	4.34	5.12		27.3	820	4.44		6.2	21.7	123	25.8	BDL					9.0	11.9	54.2	0.381
4H-2, 130–150	26.20	7.52	5.37	5.37		26.5								BDL	0.6	0.1						0.483
4H-5, 130–150	30.70	7.45	5.56	5.42		25.9	885	7.49	412.5	6.4	17.7	140	25.8	BDL								
5H-2, 130–150	35.70	7.55	5.75	5.53		25.1	817	5.62	433.5	3.2	15.7	148	24.8	BDL	0.6	0.3			8.1	11.9	53.2	0.332
5H-5, 130–150	40.20	7.37	5.95	6.03	560.9	25.3		5.24	469.7	3.8	15.6	154	25.4	BDL								
6H-2, 130–150	45.20	7.45	6.27	6.07		24.5	899	5.82	483.1	3.0	14.8	160	24.8	BDL	0.3	0.1			7.9	11.7	53.9	0.656
6H-5, 130–150	49.70	7.47	6.50	6.48		24.7		5.71	513.4	5.5	14.6	170	25.4	BDL								
7H-2, 130–150	54.70	7.57	6.76	6.62	560.9	24.6	833	6.13		0.9	14.6	174	24.5	BDL	0.0	0.1			7.9	11.8	52.8	0.621
7H-5, 130–150	59.20	7.61	6.88			24.0		6.58	541.1	6.1	12.4	180	23.9	BDL								
8H-2, 130–150	64.20	7.53	6.75	6.85		24.1		5.49	567.3	4.1	11.6	188	24.7	BDL	0.0	0.5			7.9	11.6	53.3	
8H-5, 130–150	68.70	7.50	6.82			24.0		6.00	570.2	3.0	10.2	194	24.3	BDL								0.530
9H-2, 130–150	73.70	7.48	6.68	6.82	560.9	24.4		4.73	556.3	1.3	7.4	180	21.4	BDL	0.0	0.4			7.6	11.5	52.8	0.700
9H-5, 130–150	78.20	7.36	6.57	6.78		23.5		3.80	545.4	4.9	7.2	192	23.0	BDL								
10H-2, 130–150	83.20	7.37	6.77	6.92		23.1	810	4.11		1.2	4.7	205	22.7	BDL	0.5	0.2			7.6	11.7	53.0	0.651
10H-5, 130–150	87.70	7.41	6.76			23.1		4.11	612.8	1.4	4.5	209	21.7	BDL								
11H-2, 130–150	92.70	7.38	6.72	6.82		22.7		4.27	621.6	1.1	3.9	207	20.9	BDL					7.4	11.6	53.1	0.576
11H-5, 130–150	97.20	7.46	6.66		562.4	22.6		3.76	625.0	7.6	3.6	211	20.7	BDL	0.5	0.3						
12H-2, 130–150	102.20			6.94		22.7		3.22	567.3	2.2	3.4	230	20.3	BDL								0.474
12H-5, 130–150	106.70	7.45	6.79			22.6		3.07		3.2	3.3	232	20.3	BDL	0.5	0.2						
13H-2, 130–150	111.70	7.42	6.65	6.93		22.5	894	2.75	621.9	7.0	3.3	235	19.9	BDL					7.6	11.6	52.1	0.635
13H-5, 130–150	116.20	7.37	6.87		563.4	22.6		3.20	622.2	4.6	3.2	243	18.7	BDL	0.6	0.5						0.672
14H-2, 130–150	121.20	7.38	6.72	6.94				2.49	640.9	4.9	3.0	246	18.3	BDL					7.6	11.6	53.3	0.569
14H-5, 130–150	125.70	7.66	6.61			21.9		2.24	605.0	8.3	2.9	249	18.0	BDL	0.6	0.5						0.647
15H-2, 130–150	130.70	7.38	6.65	6.90		21.8		2.25	604.1					BDL					7.6	11.7	52.4	0.644
15H-5, 130–150	135.20	7.35	6.56		562.4	22.1		2.22		5.5	3.1	267	17.0	BDL	0.8	0.5						0.528
16H-2, 130–150	140.20	7.34	6.50	7.00			960	2.35	619.3	9.4	2.6	263	16.5	BDL					7.5	11.5	51.8	0.511
16H-5, 130–150	144.70	7.32	6.61			21.5		2.22	623.8	6.2	2.4	271	15.8	BDL	1.0	1.0						0.498
17H-2, 130–150	149.70	7.28	6.58	7.03		21.7		2.20	623.3					BDL					7.9	11.3	50.8	0.530
17H-5, 130–150	154.20				564.4	21.7		2.09	540.4	3.7	2.0	282	15.0	BDL	0.5	0.7						0.465
18H-2, 130–150	159.20			6.94		21.7		2.27	558.8	3.3	1.6	292	14.6	BDL					8.1	11.2	50.9	0.552
18H-5, 130–150	163.70	7.30	6.56			21.6		1.70		4.1	1.6	289	14.3	BDL	0.8	0.8						0.505
19H-2, 130–150	168.70	7.29	6.61	7.01			942	2.80	605.8					BDL					7.9	11.0	50.9	0.476
19H-5, 130–150	173.20	7.34	6.55		563.4			2.02	602.1	3.2	1.5	290	13.7	BDL	1.2	0.9						0.461
20H-2, 130–150	178.20	6.91	6.56	6.95		21.2		2.33	596.9	5.3	1.6	296	13.0	BDL					8.3	11.1	50.9	0.474
20H-5, 130–150	182.70	7.37	6.46					1.93	554.3	4.3	1.8	301	13.3	BDL	0.9	0.9						0.417
21H-2, 130–150	187.70	7.20	6.42	6.93		21.8		1.94		4.6	1.7	311	13.0	BDL								0.453
21H-5, 130–150	192.20	7.30	6.45					1.96		2.6	1.7	307	12.7	BDL	0.9	0.9			8.4	11.0	50.6	0.303
22H-3, 130–150	197.50	7.36	6.13	6.79		21.0	1003	2.38	582.9					BDL								0.306
22H-6, 130–150	202.00	6.86	5.70					1.85	586.1	4.2	1.9	312	11.6	BDL	1.0	1.0						
23H-2, 130–150	206.70	6.88	5.73	6.71	561.4	21.1		2.20	577.8	4.6	1.8	316	11.8	BDL								0.337
23H-5, 130–150	211.20	6.79	5.70			20.9		2.00	531.0	8.8	1.7	315	11.3	BDL	0.7	0.6			8.6	11.1	49.6	
24H-2, 130–150	216.20			6.65		20.7		1.94		6.4	1.7	310	11.3	BDL								0.256
24H-5, 130–150	220.70	7.16	6.12					1.69		10.0	1.8	302	11.0	BDL	0.8	0.8						

Table T3 (continued).

Core, section, interval (cm)	Depth (mbsf)	pH	Alk (mM)	DIC (mM)	Cl⁻ (mM)	SO₄²⁻ (mM)	H₄SiO₄ (μM)	PO₄³⁻ (μM)	NH₄⁺ (μM)	Fe (μM)	Mn (μM)	Sr (μM)	Li (μM)	Ba (μM)	Acetate (μM)	Formate (μM)	NO₃⁻ (μM)	NO₂⁻ (μM)	Ca† (mM)	K† (mM)	Mg† (mM)	ΣH₂S (mM)
25H-2, 130–150	225.70	7.37	5.94	6.45		21.0	1048	1.93	555.4	4.3	2.2	315	11.1	BDL	0.8	0.8			8.6	10.9	49.2	0.189
25H-5, 130–150	230.20	7.38	5.85			20.9		1.49	562.1					BDL								
26H-2, 130–150	235.20	7.30	5.78	6.34		20.4		1.87	568.1	2.6	2.0	307	11.0	BDL								0.0891
26H-5, 130–150	239.70	7.23	5.21	5.89		20.3		1.78	523.0	2.3	1.9	306	11.3	BDL								
27H-2, 130–150	246.20	7.43	5.79	6.28		19.8		2.00		3.9	2.3	302	11.4	BDL					9.0	11.0	49.3	0.0966
27H-5, 130–150	250.70			6.14		20.6		2.09		8.9	2.8	304	11.3	BDL	0.8	0.7						
28H-2, 130–150	255.70	7.38	5.45	6.13			1115	2.25	517.5	2.0	7.0	304	12.0	BDL								0.0959
28H-5, 130–150	260.20	7.13	5.47	6.23		20.9		1.96	516.8	1.7	6.9	297	12.2	BDL								
29H-2, 130–150	265.20	7.41	5.76	6.12			1070	2.15	502.1	3.4	11.4	302	12.1	BDL					9.5	10.7	49.7	0.193
29H-5, 130–150	269.70	7.21	5.38	5.98		21.5	1281	1.95	479.7	4.9	15.6	304	13.1	BDL	0.9	0.4		0.00				0.108
30X-2, 130–150	274.70	7.46	4.99	5.22		21.7	1321	1.65		6.3	19.6	299	14.1	BDL	0.7	0.7		0.02				0.0508
30X-5, 130–150	279.20	7.20	5.03	5.6		21.1	1194	1.89		5.5	24.1	291	13.9	BDL				0.01				0.0652
31X-2, 130–150	284.30									2.6	29.8	299	14.4	BDL				0.10	9.9	10.7	49.1	
31X-5, 130–150	288.80			5.34			1265	1.55	494.0	7.5	32.6	294	15.7	BDL				0.07				<0.005
32X-2, 130–150	293.60			5.83		22.0	1289	2.25	465.8	4.3	34.8	296	15.1	BDL				0.23				<0.005
32X-5, 130–150	298.10			5.98			1267	1.87	461.6	1.1	33.4	289	14.5	BDL	1.3	1.4		0.04				
33X-2, 130–150	303.30													BDL								
33X-5, 130–150	307.80						1399	1.27	417.0	27.1	36.9	286	16.5	BDL				0.20				<0.005
34X-2, 130–150	313.00	7.70	3.59	3.67		22.2	1307	0.96		5.5	25.9	276	17.1	BDL		1.3		0.09	9.8	10.5	48.8	
34X-4, 130–150	316.00													BDL								
35X-2, 110–150	322.40			4.51		22.1	1251	1.16	440.9	0.4	32.6	260	15.7	BDL				0.04				
35X-5, 110–150	326.90	7.12	4.18	4.23						11.9	25.9	252	15.7	BDL				0.22				
36X-2, 110–150	332.00									1.7	20.4	246	16.4	BDL								
36X-5, 110–150	336.50			3.23			1168			1.2	21.8	254	17.2	BDL	2.9	2.2		0.13	10.2	11.5	48.6	
37X-2, 110–150	341.60			3.96			1200							BDL				0.13				
37X-5, 110–150	346.10	6.53	2.99	4.02						6.6	22.9	235	16.1	BDL				0.14				
38X-2, 110–150	351.30			3.71			1166	0.91	386.8	4.1	21.4	244	16.3	BDL				0.03				
38X-5, 110–150	355.80	7.23	3.39	3.49				1.15	372.4	5.9	19.8	236	17.1	BDL	2.0	1.5	0.4	0.05	10.9	11.0	48.2	
39X-2, 110–150	360.93	7.43	3.47	3.63		22.8	1203	0.87	331.2					BDL	1.2	1.3		0.05				
39X-3, 110–150	362.43	7.38	2.85	2.99			1014		324.3	11.9	18.3	239	17.1	BDL				0.07				
40X-1, 110–150	369.20	7.40	3.46	3.61		22.5	758		295.1					BDL	1.1	0.9		0.04				
41X-2, 110–150	373.70	7.52	2.85	3.13			575		278.1	13.1	20.2	221	19.2	BDL	1.3	1.5		0.04	11.5	10.5	47.9	
43X-4, 110–150	385.50	7.24	1.89	1.08		23.2	202		258.2	8.7	21.5	211	20.6	BDL				0.08	11.9	10.4	48.0	
45X-1, 130–150	398.50	7.45	2.70	2.54		23.8	1051		175.0	3.2	38.7	208	22.1	BDL	3.9	1.0			13.9	9.3	48.4	
45X-2, 130–150	400.00	7.52	2.76	2.98			991		171.2	0.5	43.6	214	21.6	BDL	3.2	1.7	1.0	0.32				
45X-5, 110–150	404.30	7.40	2.72	2.89			1032		213.6	0.3	37.1	205	22.0	BDL			0.1	0.00				
46X-2, 130–150	409.60	7.26	2.65	2.51		24.3	955		167.9	0.2	36.0	197	21.8	BDL	4.3	1.4	0.0	0.07	15.3	8.4	48.7	
46X-5, 110–130	413.90	7.10	2.04	2.19			764		161.2	0.3	38.4	200	22.6	BDL	1.6	0.7	3.1	0.20				
47X-1, 130–150	417.70			1.67		25.2	591		165.4	0.6	43.0	194	22.6	BDL	2.3	1.0	1.3	0.06	16.2	9.2	48.0	
201-1226E-																						
1H-1, 0–15	0.00	7.61	2.80	2.84	552.9			6.74	22.5	1.6	37.1	90	25.5	BDL				0.02				<0.00017
1H-1, 59–74	0.59	7.59	2.90	3.01				7.59	45.1	1.6	35.5	90	26.2	BDL								0.00024
1H-1, 95–114	0.95			3.23				6.96	56.5	0.8	33.1	93	25.6	BDL								
1H-2, 30–45	1.80	7.34	3.13	3.36	553.4			7.81	81.3	1.7	31.9	92	25.2	BDL				0.01				0.00489
1H-2, 85–100	2.35	7.44	3.31	3.46					91.5	0.9	32.3	91	24.2	BDL				0.00				0.00127
1H-3, 135–150	4.35	7.62	3.56	3.79					132.0	2.1	36.6	90	25.2	BDL				0.05				0.0166
1H-4, 135–150	5.85	7.32	3.54	3.87					148.2	1.2	34.6	95	25.9	BDL				0.01				0.00039
1H-5, 126–141	7.26	7.43	3.73	4.00	555.4				172.6	5.7	36.5	95	24.8	BDL								0.00123
2H-1, 135–150	8.95	6.64	4.03	4.27	555.9				197.3	26.4	38.0	98	25.2	BDL				0.09				0.128

Table T3 (continued).

Core, section, interval (cm)	Depth (mbsf)	pH	Alk (mM)	DIC (mM)	Cl⁻ (mM)	SO_4^{2-} (mM)	H_4SiO_4 (µM)	PO_4^{3-} (µM)	NH_4^+ (µM)	Fe (µM)	Mn (µM)	Sr (µM)	Li (µM)	Ba (µM)	Acetate (µM)	Formate (µM)	NO_3^- (µM)	NO_2^- (µM)	Ca† (mM)	K† (mM)	Mg† (mM)	ΣH_2S (mM)
2H-2, 135–150	10.45	6.70	4.19	4.46	556.9				212.8	1.5	36.3	100	25.8	BDL								0.208
2H-3, 135–150	11.95	7.72	4.17	4.53	559.4				229.1	1.7	33.3	104	25.7	BDL				0.01				0.292
2H-5, 135–150	14.95	7.40	4.47	4.85	556.9				265.2	5.7	28.5	114	29.7	BDL								0.344
3H-1, 135–150	18.45	7.56	5.20	5.03						1.3	21.9	116	25.5	BDL								0.387
3H-3, 135–150	21.45	7.74	5.12	5.29	559.9				291.2	4.0	21.3	120	25.7	BDL								0.426
3H-5, 135–150	24.45	7.69	4.60	5.39					345.1	8.7	19.3	127	25.4	BDL								0.402
9H-2, 130–150	76.90													BDL								
13H-2, 135–150	252.85	7.40	5.86	6.42	559.4				520.1	4.2	4.2	304	12.0	BDL								0.101
13H-5, 135–150	257.35	7.16	5.65	6.25					517.5	2.6	6.2	298	11.9	BDL								0.0702
14H-2, 135–150	262.35	7.20	5.37	6.06	559.9				510.8	0.3	9.4	299	11.7	BDL								0.00723
14H-5, 135–150	266.85	7.23	5.43	6.03				1.56	509.6	2.0	12.5	304	12.2	BDL								0.00764
15H-2, 135–150	271.85	7.44	5.36	6.11	560.9			1.65	503.8	2.3	16.9	306	12.7	BDL								0.0167
15H-5, 135–150	276.35	7.31	4.91	5.43				1.20	505.8	5.0	21.4	292	13.7	BDL								0.00059
16H-2, 135–150	281.35	7.46	5.12	5.68	559.9			1.33	505.2	1.3	26.6	299	13.6	BDL								0.00040
16H-5, 135–150	285.85	7.46	5.18	5.67				1.29	480.3	3.9	31.5	300	15.7	BDL								0.00023
17H-2, 135–150	290.85	7.39	5.03	5.68	559.4			1.11	488.2	12.0	34.8	298	14.6	BDL								<0.00017
17H-5, 135–150	295.35	7.33	4.71	5.38				1.24	479.1	12.2	35.1	298	14.6	BDL								<0.00017
18H-2, 135–150	300.35	7.19	5.34	5.93	561.9			1.22	472.4	2.7	37.8	298	15.2	BDL								<0.00017
18H-5, 135–150	304.85	7.18	4.99	5.59				1.05	460.5	25.4	36.6	292	15.1	BDL					10.3	10.8	49.0	<0.00017
19H-2, 135–150	309.85	7.28	5.06	5.55	560.4			1.00	437.3	27.7	35.4	290	15.8	BDL					10.5	10.6	49.0	
19H-5, 135–150	314.35	7.21	4.31	4.67				1.05	402.8	25.7	31.7	290	18.5	BDL					10.4	10.0	49.6	<0.00017
20H-2, 135–150	319.35	7.11	5.02	5.63	560.9			0.87	444.3	33.6	37.2	277	15.5	BDL					10.7	10.8	49.6	
20H-5, 135–150	323.85	7.13	4.35	4.83				0.84	428.3	41.4	30.3	268	16.3	BDL					10.6	10.7	49.5	0.00035
22X-2, 130–150	382.80	7.45	3.18	3.38			429	0.25	317.1	41.9	25.1	227	20.3	BDL					12.3	10.0	48.3	0.00020
22X-4, 130–150	385.80	7.28	2.63	2.68	559.2		508	0.29	261.8	38.2	23.8	230	20.4	BDL					12.6	9.2	49.0	
23X-1, 120–150	390.80	7.47	2.78	2.94	558.9		430	0.31	302.6	10.0	27.3	210	20.0	BDL					12.7	10.6	48.0	<0.00017
24X-2, 120–150	401.90	7.45	2.38							0.3	43.4	218	21.2	BDL				0.06	14.4	9.6	48.4	
24X-5, 120–150	406.40				554.9		957	1.13	250.5	0.3	38.0	220	21.8	BDL				0.06	14.8	9.3	48.8	<0.00017
25X-1, 124–150	410.04	7.43	2.73				709	1.02	221.7	0.3	36.8	210	21.6	BDL				0.07	15.1	9.4	47.7	<0.00017
25X-3, 120–150	413.00				551.6		784			0.5	40.1	214	22.8	BDL				0.12	15.8	8.3	51.6	
25X-5, 120–150	416.00						597			0.8	40.6	204	22.6	BDL					16.0	9.2	48.8	
25X-7, 20–46	418.00						614			0.3	41.9	204	22.2	BDL				0.12	15.7	9.0	47.8	

Notes: Alk = alkalinity, DIC = dissolved inorganic carbon. BDL = below detection limit. † = analyses performed by inductively coupled plasma–atomic emission spectroscopy rather than conventional ion chromatography. This table is also available in ASCII.

Table T4. Iron concentrations of replicate interstitial water passed through different filters, Hole 1226B.

Core, section, interval (cm)	Fe (μM)	
	0.45-μm filter	0.1-μm filter
201-1226B-		
5H-2, 130–150	8.0	7.8
5H-2, 130–150	7.8	7.6
5H-2, 130–150	5.7	5.7
5H-5, 130–150	9.7	10.0
5H-2, 130–150	5.8	5.8
5H-2, 130–150	5.9	5.9
5H-2, 130–150	11.2	10.8

Note: This table is also available in **ASCII.**

Table T5. Methane concentrations in headspace, Holes 1226B and 1226E.

Core, section, interval (cm)	Depth (mbsf)	Methane (ppm in headspace) 20 min @ 60°C	24 hr @ 22°C	Methane (μM)	Core, section, interval (cm)	Depth (mbsf)	Methane (ppm in headspace) 20 min @ 60°C	24 hr @ 22°C	Methane (μM)
201-1226B-					24H-2, 0–5	214.90		12.58	2.33
1H-2, 0–5	1.50		2.00	0.07	24H-4, 0–5	217.90		13.41	2.96
1H-3, 0–5	3.20	1.92		0.08	24H-6, 0–5	220.90	5.39		1.41
2H-2, 0–5	5.90		2.98	0.26	25H-2, 0–5	224.40		14.73	2.66
2H-4, 0–5	8.90		3.62	0.36	25H-4, 0–5	227.40		10.87	1.93
2H-6, 0–5	11.90	2.76		0.32	25H-2, 0–5	230.40	7.19		1.91
3H-2, 0–5	15.40		4.69	0.64	26H-2, 0–5	233.90		12.33	2.50
3H-4, 0–5	18.40		4.82	0.63	26H-4, 0–5	236.90		11.70	2.20
3H-6, 0–5	21.40	4.03		0.70	26H-6, 0–5	239.90	6.68		1.67
4H-2, 0–5	24.90		5.66	0.78	27H-2, 0–5	244.90		12.28	2.63
4H-4, 0–5	27.90		5.81	0.85	27H-4, 0–5	247.90		13.56	2.61
4H-6, 0–5	30.90	4.63		0.93	27H-6, 0–5	250.90	8.84		2.21
5H-2, 0–5	34.40		5.99	0.86	28H-2, 0–5	254.40		12.27	2.24
5H-4, 0–5	37.40		8.30	1.27	28H-4, 0–5	257.40		12.79	2.26
5H-6, 0–5	40.40	5.62		1.12	28H-6, 0–5	260.40	7.73		1.98
6H-2, 0–5	43.90		7.24	1.06	29H-2, 0–5	263.90		12.25	1.95
6H-4, 0–5	46.90		6.90	0.99	29H-4, 0–5	266.90		12.38	1.92
6H-6, 0–5	49.90	7.95		1.71	29H-6, 0–5	269.90	7.94		1.69
7H-2, 0–5	53.40		8.36	1.14	30X-2, 0–5	273.40		10.67	1.58
7H-4, 0–5	56.40		10.63	1.52	30X-4, 0–5	276.40		9.89	1.56
7H-6, 0–5	59.40	8.98		1.82	30X-6, 0–5	279.40	5.04		1.06
8H-2, 0–5	62.90		12.30	1.93	31X-2, 0–5	283.00		9.79	1.38
8H-4, 0–5	65.90		9.37	1.30	31X-4, 0–5	286.00		7.42	1.04
8H-6, 0–5	68.90	8.98		2.01	31X-6, 0–5	289.00	6.76		1.34
9H-2, 125–130	73.65		9.30	1.40	32X-2, 0–5	292.30		7.49	1.06
9H-4, 0–5	75.40		11.92	1.92	32X-4, 0–5	295.30		10.24	1.52
9H-6, 0–5	78.40	9.24		2.27	32X-6, 0–5	298.30	7.24		1.41
10H-2, 0–5	81.90		10.88	1.64	33X-4, 0–5	305.00		4.35*	ND
10H-4, 0–5	84.90		13.82	2.29	33X-6, 0–5	308.00	6.83*		ND
10H-6, 0–5	87.90	10.72		2.54	34X-2, 0–5	311.70		8.78	1.22
11H-2, 0–5	91.40		11.18	1.91	34X-5, 0–5	316.20	13.93*		ND
11H-4, 0–5	94.40		10.59	1.63	35X-2, 0–5	321.30		11.67	1.92
11H-6, 0–5	97.40	8.14		1.94	35X-6, 0–5	327.30	5.10		1.03
12H-2, 0–5	100.90		13.28	2.15	36X-4, 0–5	333.90		9.15	1.51
12H-4, 0–5	103.90		12.36	2.10	36X-4, 0–5	336.90	5.66		1.17
12H-6, 0–5	106.90	8.95		2.05	37X-3, 0–5	342.00		8.06	1.09
13H-2, 0–5	110.40		12.98	2.13	37X-4, 0–5	346.50	5.34		1.21
13H-4, 0–5	113.40		13.70	2.29	38X-3, 0–5	351.70		7.04	1.01
13H-6, 0–5	116.40	8.53		2.26	38X-6, 0–5	356.20	5.83		1.36
14H-2, 0–5	119.90		12.46	2.23	39X-3, 0–5	361.33	5.48		1.13
14H-4, 0–5	122.90		10.52	1.86	39X-4, 0–5	362.83		6.46	1.01
14H-6, 0–5	125.90	7.56		1.99	40X-1, 105–110	369.15	4.97		1.15
15H-2, 0–5	129.40		12.01	2.35	40X-2, 0–5	369.60		3.47*	ND
15H-4, 0–5	132.40		10.92	2.01	41X-2, 105–110	373.65	4.69		1.04
15H-6, 0–5	135.40	6.24		1.46	41X-3, 0–5	374.10		5.62	0.92
16H-2, 0–5	138.90		10.68	1.81	43X-1, 135–140	381.35		5.19	0.81
16H-4, 0–5	141.90		12.31	2.57	43X-4, 0–5	384.40	4.15		0.99
16H-6, 0–5	144.90	7.33		1.79	45X-2, 0–5	398.70		3.64	0.50
17H-2, 0–5	148.40		10.92	2.18	45X-6, 0–5	404.70	5.81*		ND
17H-4, 0–5	151.40		11.65	2.00	46X-2, 0–5	408.30		5.96	0.84
17H-6, 0–5	154.40	6.87		1.57	46X-6, 0–5	414.30	3.59*		ND
18H-2, 0–5	157.90		12.62	2.43	47X-1, 125–130	417.65	3.77*		ND
18H-4, 0–5	160.90		13.93	2.50	201-1226E-				
18H-6, 0–5	163.90	6.88		1.58	13-H3, 0–5	253.00		10.48	1.85
19H-2, 0–5	167.40		11.84	2.18	13-H6, 0–5	257.50		12.08	2.02
19H-4, 0–5	170.40		12.22	2.22	14-H2, 130–135	262.30		11.19	1.61
19H-6, 0–5	173.40	7.28		1.87	14-H5, 0–5	265.50		12.43	2.05
20H-2, 0–5	176.90		12.18	2.35	15-H2, 130–135	271.80		13.94	2.43
20H-4, 0–5	179.90		12.44	2.34	15-H5, 0–5	275.00		13.14	2.29
20H-6, 0–5	182.90	7.17		1.76	16-H2, 130–135	281.30		15.28	2.48
21H-2, 0–5	186.40		10.39	1.89	16-H5, 0–5	284.50		14.49	2.32
21H-4, 0–5	189.40		15.13	3.17	17-H2, 130–135	290.80		13.98	2.28
21H-6, 0–5	192.40	7.51		1.84	17-H5, 0–5	294.00		11.54	1.76
22H-3, 0–5	196.20		8.54	1.58	18-H2, 130–135	300.30		12.38	1.83
22H-5, 0–5	199.20		10.25	1.93	18-H5, 0–5	303.50		11.57	1.71
22H-7, 0–5	202.20	8.55		2.16	19-H2, 130–135	309.80		10.86	1.59
23H-2, 0–5	205.40	9.33		2.26					
23H-4, 0–5	208.40		11.97	2.18					
23H-6, 0–5	211.40		11.29	1.90					

Notes: * = samples were not taken volumetrically. ND = not determined. This table is also available in **ASCII.**

Table T6. Hydrogen concentrations for incubated headspace samples, Holes 1226B and 1226E.

Core, section, interval (cm)	Depth (mbsf)	H_2 (nM)	Incubation temperature (°C)
201-1226B-			
2H-3, 85–91	8.25	0.67	4
4H-3, 55–64	26.95	0.13	4
6H-3, 72–78	46.12	0.22	4
8H-3, 50–56	64.90	0.45	4
10H-3, 57–63	83.97	0.41	4
12H-3, 80–86	103.20	0.38	4
15H-3, 50–56	131.40	0.52	13
18H-3, 75–81	160.15	0.44	13
22H-4, 75–81	198.45	0.35	13
24H-3, 60–66	217.00	0.62	13
27H-3, 81–87	247.21	0.32	13
45X-3, 75–81	400.95	0.72	21
46X-3, 80–86	410.60	0.74	21
201-1226E-			
15H-3, 55–61	272.20	0.41	13
16H-3, 55–61	282.05	0.27	13
18H-3, 65–70	301.15	0.31	13
20H-3, 60–66	320.10	0.28	21

Note: This table is also available in **ASCII.**

Table T7. Concentrations of carbonate, total organic carbon (TOC), total nitrogen, and total sulfur, Holes 1226B and 1226E.

Core, section, interval (cm)	Depth (mbsf)	Description	Carbonate (wt%)	TOC (wt%)	Total nitrogen (wt%)	Total sulfur (wt%)
201-1226B-						
31X-3, 10–16	284.60	Radiolarian-bearing diatom rich nannofossil ooze	12.0	0.44	0.12	0.19
32X-3, 10–16	293.90	Radiolarian-bearing diatom rich nannofossil ooze	23.7	0.62	0.11	0.08
201-1226E-						
6H-5, 130–131	51.90	Nannofossil ooze	38.7	0.60	0.11	BDL
6H-5, 130–131	52.90	Diatom ooze	39.6	2.32	0.23	0.02
6H-6, 80–81	53.90	Nannofossil ooze	39.3	0.89	0.12	BDL
6H-7, 15–16	54.75	Diatom ooze	12.3	2.10	0.22	0.01
8H-1, 120–121	65.80	Diatom ooze	37.5	0.80	0.24	BDL
8H-2, 130–131	67.40	Nannofossil ooze	28.7	1.02	0.14	0.03
8H-4, 55–56	69.65	Diatom ooze	12.5	3.49	0.32	BDL
8H-5, 65–66	71.25	Nannofossil ooze	41.2	0.95	0.13	0.01
10H-1, 94–96	84.54	Nannofossil ooze	57.0	0.47	0.08	BDL
10H-2, 104–106	86.14	Diatom ooze	21.1	1.60	0.16	0.35
10H-6, 44–46	91.54	Diatom ooze	39.2	0.65	0.12	0.05
10H-7, 54–56	93.14	Nannofossil ooze	50.6	0.63	0.12	BDL
12H-3, 49–50	106.09	Diatom rich nannofossil ooze	48.9	0.44	0.10	0.01
13H-1, 50–51	250.50	Radiolarian-bearing diatom rich nannofossil ooze	60.8	0.30	0.07	0.01
13H-3, 50–51	253.50	Radiolarian-bearing diatom rich nannofossil ooze	70.6	0.49	0.06	BDL
13H-5, 50–51	256.50	Radiolarian-bearing diatom rich nannofossil ooze	74.1	0.40	0.02	BDL
14H-3, 50–51	263.00	Diatom rich nannofossil ooze	33.8	0.59	0.12	0.01
18H-2, 92–93	299.92	Diatom ooze	5.1	0.82	0.13	BDL
18H-5, 78–79	304.34	Diatom ooze	16.7	0.29	0.08	BDL
18H-6, 84–85	305.80	Nannofossil ooze	26.1	0.25	0.08	0.01

Notes: TOC = total organic carbon, BDL = below detection limit. This table is also available in **ASCII.**

Table T8. Potential contamination based on PFT and parallel bead counts, Holes 1226B and 1226E.

Core, section	Sample type	ng PFT/ g sediment	Potential µL seawater/ g sediment	Beads counted	Beads/ g sediment
201-1226B-					
1H-4		0.03	0.03		
2H-4		BD	BD		
3H-4		0.03	0.03		
4H-3		0.08	0.08		
6H-3		0.09	0.09		
8H-3		0.06	0.06		
10H-3		0.03	0.03		
12H-3		0.04	0.04	2 in 50 fields	84
15H-4		BD	BD		
18H-4		BD	BD		
21H-4		0.03	0.03		
22H-4		0.04	0.04	1 in 50 fields	(29)
24H-3		BD	BD		
27H-3		BD	BD		
30X-4		4.08	4.08		
40X-1		0.99	0.99		
43X-4		0.03	0.03		
43X-2	4-cm biscuit	0.23	0.23		
43X-2	Slurry biscuit 1	0.67	0.67		
43X-2	Slurry biscuit 2	0.18	0.18	0	0
45X-3		0.07	0.07		
46X-3	Biscuit for SRR	0.04	0.04		
46X-4		0.14	0.14		
47X-2	Biscuit (black sediment)	0.15	0.15	35 in 50 fields	7295
47X-2	Biscuit (red sediment)	0.17	0.17	4 in 50 fields	750
47X-CC	Crushed rock	0.05	0.05		
47X-CC	Breccia	1.78	1.78		
47X-2		0.67	0.67		
47X-3		0.29	0.29		
201-1226E-					
1H-1		BD	BD		
1H-3		BD	BD		
1H-5		BD	BD		
13H-3		0.03	0.03		
15H-3		0.03	0.03		
15H-4		BD	BD		
15H-4	Replicate	BD	BD		
16H-4		0.08	0.08		
16H-4	Replicate	0.16	0.16		
16H-4	Replicate	0.16	0.16		
17H-4		0.02	0.02		
18H-4		0.04	0.04		
19H-4		0.45	0.45		
20H-4		BD	BD		

Notes: Detection limit = 0.02 µL seawater/g sediment, BD = below detection. The potential for microbial contamination is based on 5×10^8 cells/L surface seawater. This may be viewed as an upper limit for microbial contamination because it requires the sediment to be permeable enough to allow all of the contaminating cells to travel with the PFT. SRR = sulfate reduction rate measurement. The number in parentheses represents results based on a single, non-reproducible bead observation.

Table T9. Potential contamination of slurries based on PFT, Holes 1226B and 1226E.

Core, section	Sample type	ng PFT/ g sediment	Potential µL seawater/ g sediment
201-1226B-			
2H	Slurry	0.26	0.26
12H	Slurry	BD	BD
22H	Slurry	BD	BD
43X	Slurry	BD	BD
47X	Slurry	BD	BD
201-1226E-			
1H	Slurry	BD	BD

Note: Detection limit = 0.025 mL seawater/mL slurry, BD = below detection.

Table T10. Potential contamination of slurries obtained using fluorescent beads (0.5 μm diameter) as prokaryotic cell mimics, deployed at amounts of 5×10^{11} beads per core, Site 1226.

Core, section, interval (cm)	Sample type	Beads/ 50 fov	Beads/mL sediment	Mean	Delivery confirmed
201-1226B-					
2H-3, 10–24	Slurry	7*	494		
	Vial	0	0	0*	
	Core	3	529		Yes
12H-3, 66–80	Slurry	0	0		
	Vial	0	0	0	
	Core	9	1587		Yes
22H-3	Slurry	1	71		
	Vial	0	0	36	
	Core	12	2166		Yes
43X-2	Slurry	1	71		
	Vial	0	0	36	
	Core	4	705		Yes
47X-1, 87–107	Slurry	4	593		
	Vial			593	
	Core				Yes[†]
201-1226E-					
1H-1, 114–124	Slurry	NA	NA		
	Vial	NA	NA	NA	
	Core	NA	NA		No

Notes: Vial = secondary check using vial samples collected for total bacterial counts. * = procedural contamination during processing and result ignored. † = sample not taken but deployment confirmed by incidental observation in other subsamples. fov = a field of view under the microscope approximating an area of 22,800 μm^2. NA = not applicable.

Table T11. Media inoculated with sample material from different depths, Holes 1226B and 1226E.

Core: Depth (mbsf):	1226B-2H 9	1226B-12H 104	1226B-22H 200	1226B-34X 315	1226B-43X 381	1226B-47X 420	1226E-1H Seawater on top	1226E-1H 1	1226E-18H 311
Medium:									
Sed	15°C: MPN	15°C: MPN			15°C: EN	15°C: MPN		15°C: MPN	
Mono	15°C: MPN	15°C: MPN			15°C: EN	15°C: MPN		15°C: MPN	
Poly	15°C: MPN	15°C: MPN			15°C: EN	15°C: MPN		15°C: MPN	
Aro	15°C: MPN	15°C: MPN			15°C: EN	15°C: MPN		15°C: MPN	
Lac	15°C: MPN	15°C: MPN			15°C: EN	15°C: MPN		15°C: MPN	
B-sed	15°C: MPN	15°C: MPN				15°C: MPN		15°C: MPN	
B-poly	15°C: MPN	15°C: MPN				15°C: MPN		15°C: MPN	
Rad	4°C: MPN	4°C: MPN				4°C: MPN		4°C: MPN	
Rad-Lac	4°C: MPN	4°C: MPN				4°C: MPN		4°C: MPN	
Grad	15°C: EN	15°C: EN	15°C: EN					15°C: EN	
FERM-Glyc: 8.0	60°C: EN	60°C: EN	60°C: EN		60°C: EN	60°C: EN		60°C: EN	
FERM-Glyc: 8.8	60°C: EN	60°C: EN	60°C: EN		60°C: EN				
FERM-Xyl: 8.0	60°C: EN	60°C: EN	60°C: EN		60°C: EN	60°C: EN	60°C: EN	60°C: EN	60°C: EN
FERM-Xyl: 8.8	60°C: EN	60°C: EN	60°C: EN		60°C: EN	60°C: EN	60°C: EN	60°C: EN	
SRB: 8.0	60°C: EN	60°C: EN	60°C: EN		60°C: EN	60°C: EN	60°C: EN	60°C: EN	60°C: EN
SRB: 8.6	60°C: EN	60°C: EN	60°C: EN		60°C: EN		60°C: EN		
SRB benz: 8.0	60°C: EN	60°C: EN	60°C: EN		60°C: EN	60°C: EN	60°C: EN	60°C: EN	60°C: EN
H_2/HCO_3^-/FeIII: 7.9	60°C: EN	60°C: EN	60°C: EN		60°C: EN	60°C: EN	60°C: EN	60°C: EN	
H_2/HCO_3^-/FeIII: 8.5	60°C: EN	60°C: EN	60°C: EN		60°C: EN	60°C: EN	60°C: EN	60°C: EN	60°C: EN
H_2/HCO_3^-/MnIV: 7.8	60°C: EN				60°C: EN		60°C: EN	60°C: EN	60°C: EN
H_2/HCO_3^-: 7.8	60°C: EN	60°C: EN	60°C: EN		60°C: EN	60°C: EN	60°C: EN	60°C: EN	60°C: EN
H_2/HCO_3^-: 8.8	60°C: EN	60°C: EN	60°C: EN		60°C: EN	60°C: EN	60°C: EN	60°C: EN	
C-18-lipo: 7.8	60°C: EN	60°C: EN	60°C: EN		60°C: EN	60°C: EN	60°C: EN	60°C: EN	60°C: EN
C-18-lipo: 9.0	60°C: EN	60°C: EN	60°C: EN		60°C: EN	60°C: EN	60°C: EN	60°C: EN	60°C: EN
Chlor: 7.8	60°C: EN				60°C: EN	60°C: EN	60°C: EN	60°C: EN	60°C: EN
201-1	RT, 50°C, 80°C: EN	RT, 50°C, 80°C: EN		RT, 50°C, 80°C: EN		RT, 50°C, 80°C: EN			
201-2	RT, 50°C, 80°C: EN	RT, 50°C, 80°C: EN		RT, 50°C, 80°C: EN		RT, 50°C, 80°C: EN			
201-3	RT, 50°C, 80°C: EN	RT, 50°C, 80°C: EN		RT, 50°C, 80°C: EN		RT, 50°C, 80°C: EN			
201-4	RT, 50°C, 80°C: EN	RT, 50°C, 80°C: EN		RT, 50°C, 80°C: EN		RT, 50°C, 80°C: EN			
201-5	RT, 50°C, 80°C: EN	RT, 50°C, 80°C: EN		RT, 50°C, 80°C: EN		RT, 50°C, 80°C: EN			
201-6	RT, 50°C, 80°C: EN	RT, 50°C, 80°C: EN		RT, 50°C, 80°C: EN		RT, 50°C, 80°C: EN			
201-7	RT, 50°C, 80°C: EN	RT, 50°C, 80°C: EN		RT, 50°C, 80°C: EN		RT, 50°C, 80°C: EN			
201-8	RT, 50°C, 80°C: EN	RT, 50°C, 80°C: EN		RT, 50°C, 80°C: EN		RT, 50°C, 80°C: EN			
201-9	RT, 50°C, 80°C: EN	RT, 50°C, 80°C: EN		RT, 50°C, 80°C: EN		RT, 50°C, 80°C: EN			
201-10	RT, 50°C, 80°C: EN	RT, 50°C, 80°C: EN		RT, 50°C, 80°C: EN		RT, 50°C, 80°C: EN			
201-11	RT: EN	RT: EN		RT: EN		RT: EN			
Fe(III)red	10°C: MPN	10°C: MPN	10°C: MPN		23°C: MPN	23°C: MPN		10°C: MPN	23°C: MPN
Mn(IV)red	10°C: MPN	10°C: MPN	10°C: MPN		23°C: MPN	23°C: MPN		10°C: MPN	23°C: MPN
AmOx						23°C: MPN			
NiOx						23°C: MPN			
Methylo						23°C: Plates			

Note: Enrichment assays were qualitative (EN) or quantitative (MPN) and incubated at the temperature given and/or at room temperature (RT = 21°–25°C). Media are defined in Table T9, p. 92 (see also "Microbiology," p. 14, Table T4, p. 84, T5, p. 85, and T7, p. 88, all in the "Explanatory Notes" chapter). Plates = agar plates for aerobic methylotrophs.

Table T12. Downhole temperature measurement summary, Holes 1226A, 1226B, and 1226E.

Depth (mbsf)	Tool	Measurement location	Thermal conductivity (W/[m·K])	Temperature (°C)
0.0	Adara	Seafloor 1226A-1H	—	1.72
0.0	Adara	Seafloor 1226B-2H	—	1.77
45.6	Adara	B Core 1226E-5H	0.81	4.56
61.4	Adara	B Core 1226B-7H	0.74	5.65
74.1	Adara	B Core 1226E-8H	0.77	6.35
89.9	Adara	B Core 1226B-10H	0.77	7.30
112.1	Adara	B Core 1226E-12H	0.82	8.63
118.4	Adara	B Core 1226B-13H	0.87	9.04
146.9	Adara	B Core 1226B-16H	0.92	10.61
194.4	Adara	B Core 1226B-21H	0.97	12.88
262.4	DVTP	T Core 1226B-29H	0.81	16.83
307.0	DVTP	T Core 1226E-19H	0.71	19.44
310.0	DVTP	T Core 1226B-34X	0.71	21.20
358.4	DVTP	T Core 1226B-39X	0.96	22.26
400.0	DVTP	T Core 1226E-24X	0.83	23.70
422.0	—	—	0.85*	25.88[†]

Notes: DVTP = Davis-Villinger Temperature Probe. B = bottom of core, T = top of core. — = not applicable. * = average thermal conductivity. † = projected temperature at base of hole. The last line shows the temperature extrapolated to basement using linear fit in Figure **F28,** p. 73, and the mean thermal conductivity computed from data plotted in Figure **F26A,** p. 71.

Table T13. Detail of logging operations, Hole 1226B.

Date (Feb 2002)	UTC (GMT – 7 hr)	Tool depth (mbsf)	Remarks
22	1900		Last core on deck
22	1900–2330		Wiper trip; hole displaced with 220 bbl of sepiolite; bottom of pipe set at 80 m
22	2330–0100		Logging rig-up
23	0130		Start going downward with triple combination tool string: TAP/DIT-E/HLDT/APS/HNGS/SGT
23	0325	0	Stop 5 min at mudline for temperature calibration
23	0335	80	Tool string in open hole
23	0407	423	Tool at TD; start logging upward at 900 ft/hr
23	0528	70	Tool back inside pipe; speed up to 1500 ft/hr to log mudline
23	0537	0	Mudline indicated by gamma ray at 3309 m below rig floor
23	0540	–26	End of pass 1; standing 5 min and start going back downward
23	0545	80	Tool string in open hole
23	0604	423	Tool at TD; start logging upward pass 2 at 900 ft/hr
23	0640	286	End of pass 2
23	0705	80	Tool back inside pipe; speed up to 8000 ft/hr
23	0850	0	Tool back on rig floor
23	1030		Finish rig-down

Notes: UTC = Universal Time Coordinated. TD = total depth. TAP = LDEO Temperature/Acceleration/Pressure tool, DIT-E = Dual Induction Tool, HLDT = Hostile Environment Litho-Density Tool, APS = Accelerator Porosity Sonde, HNGS = Hostile Environment Gamma Ray Sonde, SGT = Scintillation Gamma Ray Tool.